Simple Models for Turbulent Wave-Current Bottom Boundary Layer Flow: Theoretical Formulations and Applications

by

Alison I Sleath

Submitted to the Department of Civil and Environmental Engineering
in partial fulfillment of the requirements for the degree of

Master of Science in Civil and Environmental Engineering

at the

MASSACHUSETTS INSTITUTE OF TECHNOLOGY

June 2004

Author .....
Department of Civil and Environmental Engineering
May 17, 2004

Certified by .....
Ole Secher Madsen
Professor of Civil and Environmental Engineering
Thesis Supervisor

Accepted by .....
Heidi Nepf
Chairperson, Department Committee on Graduate Students

Simple Models for Turbulent Wave-Current Bottom Boundary Layer Flow: Theoretical Formulations and Applications

by

Alison I Sleath

Submitted to the Department of Civil and Environmental Engineering
on May 17, 2004, in partial fulfillment of the
requirements for the degree of
Master of Science in Civil and Environmental Engineering

Abstract

This study presents the theoretical formulations and applications of simple models for turbulent wave-current bottom boundary layer flow. Eddy viscosity formulations are presented for each model in order to analytically solve the governing equations for the bottom boundary layer. Approximations and procedures for obtaining practical solutions of the current velocity profile are presented for the two-layer Madsen-Salles (1998) and three-layer Barreto-Acobe (2001) flow models. Bottom roughness and ripple geometry models are developed for each model using fixed bed laboratory data and movable bed laboratory and field data. Wave attenuation measurements and current profile data are used in order to investigate the bottom roughness length scale for the cases of pure waves, waves in the presence of a current, and currents in the presence of waves. Wave and sediment characteristics are used to formulate a model for wave-generated ripples based on available laboratory and field data. The two-layer Madsen-Salles (1998) and three-layer Barreto-Acobe (2001) flow models are applied in conjunction with the ripple geometry and roughness models for the cases of known and unknown ripple geometry, and an assessment of expected accuracy of application of the models is presented.

Thesis Supervisor: Ole Secher Madsen
Title: Professor of Civil and Environmental Engineering

Acknowledgments

It would be difficult for me to overstate my gratitude to Ole Madsen, my advisor. Ole has been a source of inspiration and his guidance and support are second to none.

I would also like to thank my friends at MIT, who helped make my time here worthwhile and memorable. And to my best friend and fiancé, Michael, my deepest love.

Lastly, I would like to thank my family. Without them, none of this would be possible. This thesis is dedicated to my father, the late David Sleath.

Contents

List of Figures

List of Tables

Chapter 1

Introduction

1.1 Motivation

Coastal scientists and engineers strive to understand the coastal environment and the processes that directly impact the nearshore region. The effects of combined wave and current motion govern many nearshore processes and a thorough understanding of the basic hydrodynamics is critical to these processes. Throughout most of the water column, potential theory can adequately describe the fluid motion. However, viscous effects are important near the bottom boundary and potential theory can no longer be applied. At the bottom boundary, a no-slip velocity condition exists, i.e. the velocity is equal to zero. The boundary layer is the region where the velocity transitions from zero to the velocity prescribed by potential theory where viscous effects are no longer significant. Near-bottom flow significantly affects nearly all coastal processes, especially sediment transport since the interface and interaction of fluid and sediment occur in the bottom boundary layer. Hence, in order to better understand coastal processes, the physics of bottom boundary layer flow must be adequately characterized.

1.2 Objective

The main objective of this study was to present the evolution of simple models for turbulent wave-current bottom boundary layer flow, from the original two-layer Grant-Madsen (1979) model through a three-layer modified model presented by Barreto-Acobe (2001) and to arrive at a preferred flow model that adequately describes combined wave-current flow.

1.3 Thesis Outline

The development of hydrodynamic models for turbulent wave-current bottom boundary layer flows is presented in Chapter 2, beginning with the linearized governing equation for the bottom boundary layer and the introduction of the concept of an eddy viscosity in order to relate shear stress to the rate of strain. A time-invariant eddy viscosity is assumed and the time-varying and time-invariant components of the linearized governing equation are separated into two independent equations, one equation for the waves and another equation for the current. Eddy viscosity formulations are presented for the two-layered and three-layered wave-current boundary layer flow models in order to solve the equations analytically. Using each eddy viscosity formulation and boundary and matching conditions, the governing equation for the waves and the governing equation for the current are solved in terms of basic parameters. A closure hypothesis is presented and the concept of a wave-current friction factor is introduced in order to solve practical problems.

In Chapter 3, the results of the models are shown in the form of friction factor diagrams, phase angle diagrams, and wave boundary layer thickness diagrams. For the two-layer Madsen-Salles flow model, the eddy viscosity is linearly proportional to the shear velocity based on the maximum combined wave and current shear stress for the region inside the wave boundary layer. For the region outside the wave boundary layer, the eddy viscosity is linearly proportional to the shear velocity based on the

current shear stress. For the three-layer Barreto-Acobe flow model, the eddy profile is continuous. The bottom layer is proportional to the shear velocity based on the maximum combined wave and current shear stress and the top layer is proportional to the shear velocity based on the current shear stress. The constant intermediate layer provides a realistic transition from the wave boundary layer to the current boundary layer. The selection of the wave boundary layer height is discussed for each flow model type and approximate formulas to represent the results analytically are presented. Additional approximations for the three-layered Barreto-Acobe (2001) model are developed and two preferred models are selected and presented based on physical and mathematical plausibility. A procedure for obtaining predictions of the current velocity profile using the preferred models is then outlined. Lastly, an example calculation is given for a possible method of specifying the current motion.

Empirical relationships are developed in order to relate bottom roughness and ripple geometry in Chapter 4. The two-layer Madsen-Salles (1998) and three-layer Barreto-Acobe (2001) flow models are then applied to fixed bed laboratory data collected by Bagnold (1946), Sleath (1985), and Mathisen and Madsen (1996, 1999). The preferred flow models are also applied to movable bed laboratory and field data collected by Carstens et al. (1969), Lofquist (1986), Rosengaus (1987), Mathisen (1989), and Styles and Glenn (2002). For the Mathisen and Madsen (1996) data set, both wave attenuation and current profile data are available. Therefore, wave attenuation measurements were used in order to calculate the bottom roughness for the cases of pure waves and waves in the presence of a current while current measurements were used in order to establish the bottom roughness for the case of currents in the presence of waves.

In Chapter 5, wave and sediment characteristics are used to formulate a model for wave-generated ripples based on available movable bed laboratory and field data. The two-layer Madsen-Salles flow model and the three-layer Barreto-Acobe flow model are then applied in conjunction with the ripple geometry and roughness models devel-

oped in Chapter 4 for the cases of known and unknown ripple geometry. Pure wave movable bed data from Carstens et al. (1969), Lofquist (1986), Rosengaus (1987), and Mathisen (1989) and combined wave-current data collected by Mathisen and Madsen (1996) and Styles and Glenn (2002) are used in order to assess the predictive capabilities of the preferred flow models. Predicted and observed values for the wave friction factor and the current shear velocity are graphically depicted using the ripple geometry and roughness relationships developed for the flow models.

Results are summarized and presented in Chapter 6 along with a conclusion and recommendations for future study.

All of the laboratory and field data used throughout this thesis are tabulated and presented in Appendix A through Appendix E.

Chapter 2

Turbulent Wave-Current Boundary Layer Flow Models

The development of hydrodynamic models for turbulent wave-current bottom boundary layer flows is presented in this chapter. The chapter begins with the linearized governing equation for the bottom boundary layer and the concept of an eddy viscosity is used in order to relate shear stress to the rate of strain. A time-invariant eddy viscosity is assumed and the time-varying and time-invariant components of the linearized governing equation are separated into two independent equations, one equation for the waves and another equation for the current. Eddy viscosity formulations are presented for the two-layered and three-layered wave-current boundary layer flow models in order to solve the equations analytically. Using each eddy viscosity formulation and boundary and matching conditions, the governing equation for the waves and the governing equation for the current are solved in terms of basic parameters. A closure hypothesis is presented and the concept of a wave-current friction factor is introduced in order to solve practical problems.

2.1 Governing Equations

The linearized governing equation for the wave-current boundary layer can be written as

$$\rho \frac{\partial \vec{u}}{\partial t} = -\nabla p + \frac{\partial \vec{\tau}}{\partial z} \tag{2.1}$$

where

$\vec{u}$ = horizontal velocity vector = $\{u, v\}$

ρ = fluid density

∇ = gradient operator = $\left\{ \frac{\partial}{\partial x}, \frac{\partial}{\partial y} \right\}$

p = pressure

$\vec{\tau}$ = shear stress vector on horizontal planes

z = height above bottom

This linearized equation assumes uniform flow and thus neglects convective accelerations. A relationship between the viscous shear stress and rate of strain can be defined for turbulent flows based on the stress-strain relationship for Newtonian fluids. This relationship can be defined as

$$\frac{\vec{\tau}}{\rho} = \nu_t \frac{\partial \vec{u}}{\partial z} \tag{2.2}$$

where ν_t is the eddy viscosity. Using (2.2) in the linearized governing equation for the wave-current boundary layer yields

$$\frac{\partial \vec{u}}{\partial t} = -\frac{1}{\rho} \nabla p + \frac{\partial}{\partial z} \left[v_t \frac{\partial \vec{u}}{\partial z} \right] \tag{2.3}$$

This expression is analogous to the Navier-Stokes equation for laminar flows; however,

it does not assume a constant eddy viscosity.

For a time-invariant eddy viscosity, each term in (2.3) can be considered as the sum of an oscillatory component and a time-invariant component. The oscillatory component is related to the waves while the time-invariant component is related to the current.

$$\frac{\partial \vec{u}_w}{\partial t} = -\frac{1}{\rho}\nabla p_c - \frac{1}{\rho}\nabla p_w + \frac{\partial}{\partial z}\left[v_t \frac{\partial \vec{u}_c}{\partial z}\right] + \frac{\partial}{\partial z}\left[\nu_t \frac{\partial \vec{u}_w}{\partial z}\right] \tag{2.4}$$

Assuming that the eddy viscosity, ν_t, is independent of time, the time-varying components are independent of the time-invariant components in (2.4) and can therefore be separated to form two independent equations. One equation for the waves,

$$\frac{\partial \vec{u}_w}{\partial t} = -\frac{1}{\rho}\nabla p_w + \frac{\partial}{\partial z}\left[v_t \frac{\partial \vec{u}_w}{\partial z}\right] \tag{2.5}$$

and another equation for the current,

$$0 = -\frac{1}{\rho}\nabla p_c + \frac{\partial}{\partial z}\left[v_t \frac{\partial \vec{u}_c}{\partial z}\right] \tag{2.6}$$

2.1.1 The Wave Problem

To solve the time-varying wave problem, the governing equation for waves is simplified by choosing the x-direction to be the same as the direction of propagation of the wave. In other words, $\vec{u}_w = (u_w)_x = u_w$, i.e. (2.5) becomes

$$\frac{\partial u_w}{\partial t} = -\frac{1}{\rho}\frac{\partial p_w}{\partial x} + \frac{\partial}{\partial z}\left[v_t \frac{\partial u_w}{\partial z}\right] \tag{2.7}$$

Near the edge of the wave boundary layer, the velocity approaches the free stream velocity predicted by inviscid theory where viscous shear forces can be neglected. This occurs at a small distance above the bottom, $z = \delta$. According to continuity, the governing equation at this location becomes

$$\frac{\partial u_w}{\partial t} = \frac{\partial U}{\partial t} = -\frac{1}{\rho}\frac{\partial p_w}{\partial x} \tag{2.8}$$

where U is the horizontal free stream velocity predicted by linear potential theory at a location that is just outside of the boundary layer. At this location, the pressure gradient just inside the boundary layer is independent of depth and is equal to the pressure gradient just outside the boundary layer. Subtracting (2.8) from (2.7) yields

$$\frac{\partial u_w}{\partial t} - \frac{\partial U}{\partial t} = \frac{\partial}{\partial z}\left[\nu_t \frac{\partial u_w}{\partial z}\right] \tag{2.9}$$

Since the horizontal free stream velocity predicted by linear potential theory at a location that is just outside of the boundary layer, U, is independent of the distance above the bottom, it follows that $\frac{\partial U}{\partial z} = 0$. Using the quantity

$$\tilde{u} = u_w - U \tag{2.10}$$

where $\tilde{u}$ is the deficit velocity, equation (2.9) can be rewritten

$$\frac{\partial \tilde{u}}{\partial t} = \frac{\partial}{\partial z}\left[\upsilon_t \frac{\partial \tilde{u}}{\partial z}\right] \tag{2.11}$$

Since the wave-associated turbulence is restricted to a small height above the bottom, the wave boundary layer thickness is expected to be much smaller than the local water depth, in other words, $\delta/h << 1$. Therefore, U at the edge of the wave boundary

layer, at a distance $z = \delta$, is equivalent to U at the bottom, $z = 0$. According to linear wave theory, the predicted orbital velocity at the bottom is

$$U = U_b \cos \omega t \tag{2.12}$$

where U_b is the magnitude of the bottom orbital velocity and $\omega = {}^{2\pi}/_{T}$. The solution to (2.11) is, by virtue of (2.12), expected to be simple harmonic. Therefore, it can be written in the following form

$$u_d = \frac{\tilde{u}}{U_b} = \Re e \left\{ u_d \exp\left(i\omega \mathrm{t}\right) \right\} \tag{2.13}$$

where u_d is the normalized deficit velocity, $i = \sqrt{-1}$, and the operator $\Re e$ indicates the real part of the argument. Using (2.13) in (2.11), the governing equation for the time-varying component of the velocity field within the wave boundary layer is

$$\frac{d}{dz}\left[\nu_t \frac{du_d}{dz}\right] - i\omega u_d = 0 \tag{2.14}$$

One boundary condition for (2.14) is that the velocity must satisfy the no-slip condition at the bottom boundary, $u_w = 0$ or $u_d = -1$. Another boundary condition is that the velocity at the edge of the wave boundary layer must match the velocity of the free stream just outside of the boundary layer, $u_w = U$ or $u_d \to 0$ as $z \to \infty$.

2.1.2 The Current Problem

Since the eddy viscosity is assumed to be time-invariant, the governing equation for the current will only depend on the distance above the bottom. Simplifying the governing equation for the current and denoting the magnitude of the current velocity

vector as $u_c = |\vec{u}_c| = u_c(z)$, the governing equation for the time-invariant component of the current velocity (2.6) becomes

$$0 = -\frac{1}{\rho}\nabla p_c + \frac{\partial}{\partial z}\left[v_t \frac{\partial u_c}{\partial z}\right] \tag{2.15}$$

Integrating both sides of (2.15) and using the definition for the current shear stress at the bottom, a general equation for the current can be obtained. Using the law of the wall argument to neglect the pressure gradient term close to the bottom, the solution reduces to

$$\frac{\tau_c}{\rho} = \nu_t \frac{du_c}{dz} \tag{2.16}$$

Although the current boundary layer is expected to extend over the entire water depth, the preceding solution can be considered valid for the inner region of the current boundary layer. In other words, the solution is valid for small distances above the bottom relative to the total depth yet larger than the wave boundary layer thickness, δ. The boundary condition for the current equation (2.16) is the no slip condition at the bottom boundary, i.e. $u_c = 0$ at the bottom.

2.2 Eddy Viscosity Models

The next step in this analysis is to define an eddy viscosity based on the objectives stated in Chapter 1. Two types of eddy viscosity models will be examined in this section: two-layered Grant and Madsen (1979 and 1986) model types and three-layered model types (Madsen and Wikramanayake (1991), Styles and Glenn (2000), and Barreto-Acobe (2001)).

2.2.1 Two-Layered Grant-Madsen Models

The formulation for the eddy viscosity in the two-layered original Grant-Madsen type models is

$$\nu_t = \begin{cases} \kappa u_{*m} (z + z_b) & z + z_b < \delta \\ \kappa u_{*c} (z + z_b) & z + z_b > \delta \end{cases} \tag{2.17}$$

where

κ = von Karman's constant ($\kappa \cong 0.4$)

z = vertical height above bottom

z_b = either 0 (Original Grant-Madsen) or z_0 (Modified Grant-Madsen)

u_{*m} = shear velocity based on maximum combined bottom shear stress

u_{*c} = shear velocity based on current bottom shear stress

For $z_b = 0$, the no slip condition at the bottom boundary is applied at $z = z_0$. However, for $z_b = z_0$, the no slip condition at the bottom boundary is applied at $z = 0$ by introduction of the the vertical profile translation distance $z_b = z_0$.
This time-invariant eddy viscosity formulation will be used in both the wave problem and the current problem. For the region inside the wave boundary layer, the eddy viscosity is linearly proportional to the shear velocity based on the maximum combined wave and current shear stress. For the region outside the wave boundary layer, the eddy viscosity is linearly proportional to the shear velocity based on the current shear stress. The model's definition of the wave boundary layer thickness is

$$\delta = \alpha l \tag{2.18}$$

where the term α is the fitting parameter for this model and will be discussed in depth in Chapter 3. The wave boundary layer length scale, l, is defined as

$$l = \frac{\kappa u_{*m}}{\omega} \tag{2.19}$$

where ω is the radian frequency of the periodic wave. The shear velocities based on the maximum combined and current shear stress are $u_{*m} = \sqrt{\tau_m/\rho}$ and $u_{*c} = \sqrt{\tau_c/\rho}$, respectively. The maximum combined shear stress is the vector sum of the maximum wave shear stress and the current shear stress

$$\vec{\tau}_m = \vec{\tau}_{wm} + \vec{\tau}_c = (\tau_{wm} + \tau_c \left|\cos\phi_{wc}\right|, \tau_c \sin\phi_{wc}) \tag{2.20}$$

where ϕ_{wc} is the angle between the direction of the waves and the current. The maximum shear stress due to waves acting on the bottom can be determined from

$$\tau_{wm} = \rho\nu_t \left.\frac{\partial u_w}{\partial z}\right|_{z+z_b\to 0} \tag{2.21}$$

for the original Grant-Madsen type of eddy viscosity model and

$$\tau_{wm} = \rho\nu_t \left.\frac{\partial u}{\partial z}\right|_{z+z_b=z_0} \tag{2.22}$$

for the modified Grant-Madsen type of eddy viscosity model where

$$z_0 = \frac{k_n}{30} \tag{2.23}$$

for rough turbulent flow with k_n denoting the equivalent Nikuradse sand grain roughness. The magnitude of the maximum combined shear stress vector is obtained from (2.20) to be

$$\tau_m = |\vec{\tau}_m| = \sqrt{\tau_{wm}^2 + 2\tau_{wm}\tau_c \left|\cos\phi_{wc}\right| + \tau_c^2} \tag{2.24}$$

Wave Solution

In the two-layered Grant-Madsen type models, the wave problem is solved by assuming a linearly increasing eddy viscosity for the entire wave boundary layer. Therefore, the governing equation for the waves (2.14) becomes

$$\frac{d}{dz}\left[\kappa u_{*m}\left(z + z_b\right)\frac{du_d}{dz}\right] - i\omega u_d = 0 \tag{2.25}$$

This equation governing the waves can be simplified by introducing a new non-dimensional variable of the form

$$\zeta = \frac{z + z_b}{l} \tag{2.26}$$

where l is given by (2.19). Using (2.26) in (2.25),

$$\frac{d}{d\zeta}\left[\zeta\frac{du_d}{d\zeta}\right] - iu_d = 0 \tag{2.27}$$

From Hildebrand (1976), the solution of (2.27) is a special form of the Bessel equation

$$u_d = A\left\{\ker\left(2\sqrt{\zeta}\right) + i\mathrm{kei}\left(2\sqrt{\zeta}\right)\right\} + B\left\{\mathrm{ber}\left(2\sqrt{\zeta}\right) + i\mathrm{bei}\left(2\sqrt{\zeta}\right)\right\} \tag{2.28}$$

where *ker*, *kei*, *ber*, and *bei* are Kelvin functions of zeroth order and A and B are complex constants that will be determined by applying the boundary conditions, which

are for a turbulent flow:

$u_d = -1$ at $z + z_b = z_0$ or $\zeta = \zeta_0$

$u_d \to 0$ at $z + z_b \to \infty$ or $\zeta \to \infty$

where the non-dimensional form of z_0 is

$$\zeta_0 = \frac{z_0}{l} \tag{2.29}$$

From the boundary condition far away from the bottom $u_d \to 0$ at $z + z_b \to \infty$ or $\zeta \to \infty$, it can be seen that

$$B = 0 \tag{2.30}$$

since *ber* and *bei* become exponentially large when their arguments go toward infinity (Abramowitz and Stegun, 1972). Applying the no-slip boundary condition at the bottom, $u_d = -1$ at $z + z_b = z_0$ or $\zeta = \zeta_0$, to (2.28), yields

$$-1 = A\left\{\ker\left(2\sqrt{\zeta_0}\right) + i\mathrm{kei}\left(2\sqrt{\zeta_0}\right)\right\} \tag{2.31}$$

Therefore

$$u_d = \frac{-\left\{\ker\left(2\sqrt{\zeta}\right) + i\mathrm{kei}\left(2\sqrt{\zeta}\right)\right\}}{\ker\left(2\sqrt{\zeta_0}\right) + i\mathrm{kei}\left(2\sqrt{\zeta_0}\right)} \tag{2.32}$$

Recalling the definition of u_d (2.13), the solution for the wave velocity, u_w is

$$u_w = U_b \Re e\left\{\left[1 - \frac{\ker\left(2\sqrt{\zeta}\right) + i\mathrm{kei}\left(2\sqrt{\zeta}\right)}{\ker\left(2\sqrt{\zeta_0}\right) + i\mathrm{kei}\left(2\sqrt{\zeta_0}\right)}\right]\exp\left(i\omega \mathrm{t}\right)\right\}$$

$$= \Re e \left\{ \left[1 - \frac{\ker\left(2\sqrt{\zeta}\right) + i\mathrm{kei}\left(2\sqrt{\zeta}\right)}{\ker\left(2\sqrt{\zeta_0}\right) + i\mathrm{kei}\left(2\sqrt{\zeta_0}\right)} \right] u_\infty \right\} \tag{2.33}$$

where

$$u_\infty = U_b \exp\left(i\omega t\right) \tag{2.34}$$

For small values of ζ, i.e. for distances close to the bottom boundary, (2.33) can be approximated by a logarithmic velocity profile using the approximations for small arguments of *ker* and *kei* (Abramowitz and Stegun, 1972). Thus, for $\zeta \to 0$,

$$u_w = \Re e \left\{ \left[1 + \frac{1/2}{\ker\left(2\sqrt{\zeta_0}\right) + ikei\left(2\sqrt{\zeta_0}\right)} \left(\ln\zeta + 1.154 + i\frac{\pi}{2} \right) \right] u_\infty \right\} \tag{2.35}$$

Current Solution

In this section, the eddy viscosity formulation (2.17) will be used in the governing equation for the current (2.16) along with the appropriate boundary conditions. As stated before, δ, the wave boundary layer thickness is defined by equation (2.18). For the lower region, $z + z_b < \delta$, the solution to (2.16) after applying the no-slip boundary condition is

$$u_c = \frac{u_{*c}^2}{\kappa u_{*m}} \ln\left[\frac{z + z_b}{z_0}\right] \tag{2.36}$$

For the upper region, $z + z_b > \delta$, the solution to (2.16) is

$$u_c = \frac{u_{*c}}{\kappa} \ln\left[\frac{z + z_b}{\delta}\right] + C \tag{2.37}$$

where C is a constant of integration found by requiring that the velocity must be continuous at $z + z_b = \delta$.

After matching the velocities, the full solution is:

For $z + z_b < \delta$

$$u_c = \frac{u_{*c}}{\kappa}\frac{u_{*c}}{u_{*m}} \ln\left[\frac{z + z_b}{z_0}\right] \tag{2.38}$$

For $z + z_b > \delta$

$$u_c = \frac{u_{*c}}{\kappa}\left(\ln\left[\frac{z + z_b}{\delta}\right] + \frac{u_{*c}}{u_{*m}} \ln\left[\frac{\delta}{z_0}\right]\right) \tag{2.39}$$

Wave Friction Factor and Closure Hypothesis

In order to evaluate the equations in the turbulent wave-current bottom boundary layer models, α and z_0 must be specified. Therefore, a wave friction factor concept in the definition of the bottom shear stress will be used in order to close the problem. The shear velocity, u_{*m}, scales the eddy viscosity in the wave boundary layer and corresponds to the maximum combined shear stress due to waves and currents. The maximum combined shear stress (2.24) can be re-written as

$$\tau_m = \tau_{wm}\sqrt{1 + 2\left(\frac{\tau_c}{\tau_{wm}}\right)|\cos\phi_{wc}| + \left(\frac{\tau_c}{\tau_{wm}}\right)^2} \tag{2.40}$$

Next, a parameter, μ, is defined

$$\mu^2 = \frac{\tau_c}{\tau_{wm}} = \left(\frac{u_{*c}}{u_{*w}}\right)^2 \tag{2.41}$$

which expresses the relative magnitude of the current shear stress to the maximum wave shear stress.

Equation (2.40) can now be re-written

$$\tau_m = \tau_{wm}\sqrt{1 + 2\mu^2 \left|\cos\phi_{wc}\right| + \mu^4} \tag{2.42}$$

Another parameter, C_μ, can be introduced for further simplification

$$C_\mu = \sqrt{1 + 2\mu^2 \left|\cos\phi_{wc}\right| + \mu^4} \tag{2.43}$$

Equation (2.43) can be used with (2.42) in order to obtain a direct relationship between the maximum combined shear velocity and the wave shear velocity

$$u_{*m} = u_{*w}\sqrt{C_\mu} \tag{2.44}$$

Jonsson (1966) defined a wave friction factor for pure wave motion, f_w. By analogy, we introduce a generalized wave friction factor for wave and current motion.

$$\tau_{wm} = \frac{1}{2}\rho f_{wc} U_b^2 \tag{2.45}$$

Re-arranging (2.45)

$$\sqrt{\frac{f_{wc}}{2}} = \sqrt{\frac{\tau_w}{\rho U_b^2}} = \frac{u_{*w}}{U_b} = \frac{u_{*w}\omega}{A_b} \tag{2.46}$$

where A_b is the wave excursion amplitude and is given by

$$A_b = \frac{U_b}{\omega} \tag{2.47}$$

Equations (2.44) and (2.46) can be used in the definition of ζ_0 (2.29)

$$\zeta_0 = \frac{z_0}{l} = \frac{k_n/30}{\kappa u_{*m}/\omega} = \frac{k_n/30}{\kappa u_{*w}\sqrt{C_\mu}/\omega} = \frac{\sqrt{2}}{30\kappa}\frac{k_n}{C_\mu A_b}\sqrt{\frac{C_\mu}{f_{wc}}} \tag{2.48}$$

The definition of the maximum bottom wave shear stress is used to close the problem. The maximum shear stress associated with the wave for the original Grant-Madsen type model is

$$\frac{\tau_{wm}}{\rho} = \max\left\{\left[\nu_t \frac{\partial u_w}{\partial z}\right]_{z+z_b\to 0}\right\} \tag{2.49}$$

Introducing (2.35) into (2.50) and taking the limit, the magnitude of the maximum wave shear velocity squared at the bottom for the original Grant-Madsen model is

$$u_{*w}^2 = \frac{\kappa u_{*m} U_b}{2\sqrt{\left\{\ker^2\left(2\sqrt{\zeta_0}\right) + \mathrm{kei}^2\left(2\sqrt{\zeta_0}\right)\right\}}} \tag{2.50}$$

For the modified Grant-Madsen type model,

$$\frac{\tau_{wm}}{\rho} = \max\left\{\left[\nu_t \frac{\partial u_w}{\partial z}\right]_{z+z_b\to z_0}\right\} \tag{2.51}$$

Using the definition of u_d in (2.13), (2.51) can be re-written as

$$\frac{\tau_{wm}}{\rho} = u_{*w}^2 = U_b\left[\frac{\nu_t}{l}\left|\frac{\partial u_d}{\partial \zeta}\right|\right]_{z+z_b\to z_0} \tag{2.52}$$

Using the definition of ν_t in (2.17) yields

$$u_{*w}^2 = \kappa u_{*m} U_b \left[\zeta \left| \frac{\partial u_d}{\partial \zeta} \right| \right]_{z+z_b \to z_0} \tag{2.53}$$

Considering (2.32), (2.53) can be re-written as

$$u_{*w}^2 = \kappa u_{*m} U_b \sqrt{\zeta_0} \left| A \left\{ \ker' \left(2\sqrt{\zeta_0} \right) + i \mathrm{kei}' \left(2\sqrt{\zeta_0} \right) \right\} \right| \tag{2.54}$$

where the primes denote differentiation with respect to the argument of the function and A is given by (2.31). If ϕ_{wc} and u_{*c} are given and using (2.24) and $u_{*m} = \sqrt{\tau_m/\rho}$, (2.54) is an implicit equation for u_{*w}.

Using (2.46) in (2.54), a relationship can be obtained for the friction factor, f_{wc}, and the parameter ζ_0

$$\sqrt{\frac{f_{wc}}{C_\mu}} = \kappa \sqrt{2\zeta_0} \left| A \left(\ker' \left(2\sqrt{\zeta_0} \right) + i \mathrm{kei}' \left(2\sqrt{\zeta_0} \right) \right) \right| \tag{2.55}$$

A relationship between the friction factor, f_{wc}, and the relative roughness parameter, A_b/k_n , can be obtained using (2.48)

$$C_\mu \frac{A_b}{k_n} = \frac{\sqrt{2}}{30\kappa\zeta_0} \sqrt{\frac{C_\mu}{f_{wc}}} \tag{2.56}$$

Equations (2.55) and (2.56) can be used in order to develop a modified wave friction factor diagram which shows the dependency of the friction factor to the relative roughness.

The phase angle between the shear stress and the near bottom velocity is given by

$$\theta_t = \arctan\left(\frac{-\mathrm{kei}\left(2\sqrt{\zeta_0}\right)}{\ker\left(2\sqrt{\zeta_0}\right)}\right) \tag{2.57}$$

for the original Grant-Madsen model and

$$\theta_t = \arctan\left(\frac{\Im m\left|A\left(\ker'\left(2\sqrt{\zeta_0}\right)+i\mathrm{kei}'\left(2\sqrt{\zeta_0}\right)\right)\right|}{\Re e\left|A\left(\ker'\left(2\sqrt{\zeta_0}\right)+i\mathrm{kei}'\left(2\sqrt{\zeta_0}\right)\right)\right|}\right) \tag{2.58}$$

for the modified Grant-Madsen model.

Note that the primary difference between the original and modified Grant-Madsen type models is in the evaluation of the shear stress, i.e. the original Grant-Madsen model evaluates the shear stress at the limit of $z + z_b \to 0$ while the modified Grant-Madsen model evaluates the shear stress at $z + z_b = z_0$. $z_b = 0$ for the original Grant-Madsen model while $z_b = z_0$ for the modified Grant-Madsen model. Another modification of the original Grant-Madsen model is associated with the choice of α in the definition of the wave boundary layer thickness, (2.18). This modification will be discussed in Chapter 3.

2.2.2 Three-Layered Models

The formulation for the three-layered modified Grant-Madsen (Madsen and Wikramanayake, 1991) and Barreto-Acobe (2001) eddy viscosity models is:

$$\nu_t = \begin{cases} \kappa u_{*m}\left(z + z_b\right) & z + z_b < \alpha l \\ \kappa u_{*m}\alpha l & \alpha l < z + z_b < \alpha l/\varepsilon \\ \kappa u_{*c}\left(z + z_b\right) & \alpha l/\varepsilon < z + z_b \end{cases} \tag{2.59}$$

where

z_b = either z_0 (Barreto-Acobe, 2001) or 0

l = scale of wave boundary layer thickness, given by (2.19)

α = fraction of the wave boundary layer thickness over which the eddy viscosity varies linearly and

ε is a parameter that expresses the relative magnitude of the current and combined wave-current turbulence intensities ($\varepsilon \leq 1$).

$$\varepsilon = \frac{u_{*c}}{u_{*m}} \tag{2.60}$$

The three-layered models have a continuous eddy viscosity profile, unlike the original and modified Grant-Madsen models presented in section (2.2.1), and will therefore yield a smooth velocity profile. The intermediate layer, $\alpha l < z < \alpha l/\varepsilon$, provides a realistic transition from the wave boundary layer to the current boundary layer. While the two-layered Grant-Madsen type models utilized different eddy viscosity formulations for the wave and current problems, the same eddy viscosity formulation will be used for both the wave problem and current problem with the three-layered eddy viscosity models.

Wave Solution

Since the vertical variation of the eddy viscosity has been defined (2.59), it can be used in the governing equation for the waves and solved for the three regions of importance. In the lower region, $z + z_b < \alpha l$, the governing equation for the waves (2.14) is

$$\frac{d}{dz}\left[\kappa u_{*m}\left(z + z_b\right)\frac{du_d}{dz}\right] - i\omega u_d = 0 \tag{2.61}$$

In the intermediate region, $\alpha l < z + z_b < \alpha l/\varepsilon$, where the eddy viscosity is constant, the governing equation for the waves (2.14) is

$$\frac{d}{dz}\left[\kappa u_{*m}\alpha l\frac{du_d}{dz}\right] - i\omega u_d = 0 \tag{2.62}$$

Finally, for the upper region, $z + z_b > \alpha l/\varepsilon$, the governing equation for the waves (2.14) is

$$\frac{d}{dz}\left[\kappa u_{*c}\left(z + z_b\right)\frac{du_d}{dz}\right] - i\omega u_d = 0 \tag{2.63}$$

Using (2.26) in (2.61) for the lower region, $\zeta < \alpha$

$$\frac{d}{d\zeta}\left[\zeta\frac{du_d}{d\zeta}\right] - iu_d = 0 \tag{2.64}$$

Using Hildebrand (1976), the general solution of (2.64) is

$$u_d = A\left\{\ker\left(2\sqrt{\zeta}\right) + i\text{kei}\left(2\sqrt{\zeta}\right)\right\} + B\left\{\text{ber}\left(2\sqrt{\zeta}\right) + i\text{bei}\left(2\sqrt{\zeta}\right)\right\} \tag{2.65}$$

where *ker*, *kei*, *ber*, and *bei* are Kelvin functions of zeroth order and A and B are complex constants.

For the intermediate region, $\alpha < \zeta < \alpha/\varepsilon$, (2.62) becomes

$$\frac{d^2u_d}{d\zeta^2} - \frac{i}{\alpha}u_d = 0 \tag{2.66}$$

The general solution of (2.66) is

$$u_d = C\exp\left(\sqrt{i/\alpha}\zeta\right) + D\exp\left(-\sqrt{i/\alpha}\zeta\right) \tag{2.67}$$

where $\sqrt{i} = (1+i)/\sqrt{2}$ and C and D are complex constants.

For the upper region, $\zeta > \alpha/\varepsilon$, (2.63) becomes

$$\frac{d}{d\zeta}\left[\zeta\varepsilon\frac{du_d}{d\zeta}\right] - iu_d = 0 \tag{2.68}$$

The solution for (2.68) is

$$u_d = E\left\{\ker\left(2\sqrt{\zeta/\varepsilon}\right) + i\text{kei}\left(2\sqrt{\zeta/\varepsilon}\right)\right\} + F\left\{\text{ber}\left(2\sqrt{\zeta/\varepsilon}\right) + i\text{bei}\left(2\sqrt{\zeta/\varepsilon}\right)\right\} \tag{2.69}$$

where E and F are complex constants.

In order to determine A, B, C, D, E, and F, boundary and matching conditions must be invoked. The boundary and matching conditions for the preceding equations governing the waves are:

$u_d = -1$ at $\zeta = \zeta_0$

$u_{d-} = u_{d+}$ at $\zeta = \alpha$

$\frac{\partial}{\partial\zeta}[u_{d-}] = \frac{\partial}{\partial\zeta}[u_{d+}]$ at $\zeta = \alpha$

$u_{d-} = u_{d+}$ at $\zeta = \alpha/\varepsilon$

$\frac{\partial}{\partial\zeta}[u_{d-}] = \frac{\partial}{\partial\zeta}[u_{d+}]$ at $\zeta = \alpha/\varepsilon$

$u_d \to 0$ as $\zeta \to \infty$

Applying the no-slip boundary condition at the bottom,$u_d = -1$ at $\zeta = \zeta_0$, to (2.65), yields

$$-1 = A\left\{\ker\left(2\sqrt{\zeta_0}\right) + ikei\left(2\sqrt{\zeta_0}\right)\right\} + B\left\{\text{ber}\left(2\sqrt{\zeta_0}\right) + i\text{bei}\left(2\sqrt{\zeta_0}\right)\right\} \tag{2.70}$$

Matching the velocity and velocity gradients (shear stress) using (2.65) and (2.67) at $\zeta = \alpha$ from above and below gives

$$A\left\{\ker\left(2\sqrt{\alpha}\right) + i\text{kei}\left(2\sqrt{\alpha}\right)\right\} + B\left\{\text{ber}\left(2\sqrt{\alpha}\right) + i\text{bei}\left(2\sqrt{\alpha}\right)\right\} =$$

$$C\exp\left(\sqrt{i\alpha}\right)+D\exp\left(-\sqrt{i\alpha}\right) \tag{2.71}$$

$$A\left\{\mathrm{ker}'\left(2\sqrt{\alpha}\right)+i\mathrm{kei}'\left(2\sqrt{\alpha}\right)\right\}+B\left\{\mathrm{ber}'\left(2\sqrt{\alpha}\right)+i\mathrm{bei}'\left(2\sqrt{\alpha}\right)\right\}=$$

$$C\sqrt{i}\exp\left(\sqrt{i\alpha}\right)-D\sqrt{i}\exp\left(-\sqrt{i\alpha}\right) \tag{2.72}$$

From the boundary condition far away from the bottom $u_d \to 0$ at $z \to \infty$ or $\zeta \to \infty$, it can be seen that

$$F=0 \tag{2.73}$$

since ber and bei become exponentially large when their arguments go toward infinity (Abramowitz and Stegun, 1972).

Matching the velocity and velocity gradients (shear stress) using (2.67) and (2.69) with $F=0$ at $\zeta=\alpha/\varepsilon$ yields

$$C\exp\left(\sqrt{i\alpha}\Big/\varepsilon\right)+D\exp\left(-\sqrt{i\alpha}\Big/\varepsilon\right)=E\left\{\mathrm{ker}\left(2\sqrt{\alpha}/\varepsilon\right)+i\mathrm{kei}\left(2\sqrt{\alpha}/\varepsilon\right)\right\} \tag{2.74}$$

$$C\sqrt{i}\exp\left(\sqrt{i\alpha}\right)-D\sqrt{i}\exp\left(-\sqrt{i\alpha}\right)=E\left\{\mathrm{ker}'\left(2\sqrt{\alpha}/\varepsilon\right)+i\mathrm{kei}'\left(2\sqrt{\alpha}/\varepsilon\right)\right\} \tag{2.75}$$

In the previous equations (2.72) and (2.75), the prime notation implies differentiation with respect to the argument of the function. At this point, there are five equations (2.70), (2.71), (2.72), (2.74), and (2.75) and five unknown constants, A, B, C, D, and E. These equations can be solved analytically in terms of α, ζ_o, and ε.

For the original Grant-Madsen type model, α is the only variable and must be fitted

from experimental data. Later, the modified Grant-Madsen type model developed a relationship for α as a function of the relative roughness. For the three-layered Barreto-Acobe model, α is pre-determined based on boundary layer studies and is discussed in Section (3.1.3).

Current Solution

The current problem is governed by equation (2.16) with the eddy viscosity specified by (2.59). Invoking boundary and matching conditions, the governing equation for the lower region, $z + z_b < \alpha l$, is

$$\kappa u_{*m} (z + z_b) \frac{du_c}{dz} = u_{*c}^2 \tag{2.76}$$

Invoking the no-slip condition at $z + z_b = z_0$, the solution to (2.76) is

$$u_c = \frac{u_{*c}}{u_{*m}} \frac{u_{*c}}{\kappa} \ln \left[\frac{z + z_b}{z_0} \right] \tag{2.77}$$

For the intermediate region, $\alpha l < z + z_b < \alpha l/\varepsilon$, the eddy viscosity is constant and the governing equation for the current problem is

$$\kappa u_{*m} \alpha l \frac{du_c}{dz} = u_{*c}^2 \tag{2.78}$$

Considering the condition of matching current velocities at $z + z_b = \alpha l$, the solution to (2.78) is

$$u_c = \frac{u_{*c}}{u_{*m}} \frac{u_{*c}}{\kappa} \left(\frac{z + z_b}{\alpha l} - 1 + \ln \left[\frac{\alpha l}{z_0} \right] \right) \tag{2.79}$$

For the upper region, $z+z_b > \alpha l/\varepsilon$, the eddy viscosity is linear yielding a logarithmic velocity profile

$$u_c = \frac{u_{*c}}{\kappa}\left[\ln\left(\frac{z+z_b}{\alpha l/\varepsilon}\right)+C\right] \tag{2.80}$$

Invoking the matching condition at $z+z_b = \alpha l/\varepsilon$, the constant C is determined and can be substituted into (2.80) to yield

$$u_c = \frac{u_{*c}}{\kappa}\left(\ln\left(\frac{z+z_b}{\alpha l/\varepsilon}\right)+1+\frac{u_{*c}}{u_{*m}}\left[\ln\left(\frac{\alpha l}{z_0}\right)-1\right]\right) \tag{2.81}$$

Wave Friction Factor and Closure Hypothesis

In order to evaluate the equations in the three-layered turbulent wave-current bottom boundary layer model, α , ε , and ζ_0 must be specified. $\zeta_b = z_b/l$ is a term that translates the velocity profile in the vertical direction by an amount z_b. The solution is in terms of $\zeta = (z_b+z)/l$ and is therefore independent of z_b. However, z is the vertical distance above the bottom so z_b must be specified in order to plot the velocity profile, $u(z)$. Therefore, similar to the closure hypothesis for the two-layered models, a wave friction factor concept in the definition of the bottom shear stress will be utilized in order to close the three-layered model problem.

C_μ can be written in terms of the previously defined parameters, μ and ε.

$$\sqrt{C_\mu} = \frac{u_{*m}}{u_{*w}} = \frac{(u_{*c}/u_{*w})}{(u_{*c}/u_{*m})} = \frac{\mu}{\varepsilon} \tag{2.82}$$

The definition of the wave shear stress for the three-layered model type is

$$\frac{\tau_{wm}}{\rho} = \lim_{z+z_b \to z_0} \left\{ \left| \nu_t U_b \frac{\partial u_d}{\partial z} \right| \right\} \tag{2.83}$$

Equation (2.83) can be evaluated at $z = z_0$, i.e. $z_b = 0$.

Introducing the appropriate expressions for ν_t and u_d into (2.83),

$$u_{*w}^2 = \lim_{\zeta \to \zeta_0} \left\{ \left| \kappa u_{*m} \zeta U_b \frac{\partial u_d}{\partial \zeta} \right| \right\}$$

$$= \kappa u_{*w} \sqrt{C_\mu} U_b \lim_{\zeta \to \zeta_0} \left\{ \left| \sqrt{\zeta} \frac{\partial u_d}{\partial \left(2\sqrt{\zeta}\right)} \right| \right\}$$

$$= \kappa u_{*w} \sqrt{C_\mu} U_b \lim_{\zeta \to \zeta_0} \sqrt{\zeta} \left\{ \left| A \left[\ker'\left(2\sqrt{\zeta}\right) + i\mathrm{kei}'\left(2\sqrt{\zeta}\right) \right] + B \left[\mathrm{ber}'\left(2\sqrt{\zeta}\right) + i\mathrm{bei}'\left(2\sqrt{\zeta}\right) \right] \right| \right\} \tag{2.84}$$

Using (2.46) in (2.84), a relationship can be obtained for the friction factor, f_{wc}, and the parameter ζ_0

$$\sqrt{\frac{f_{wc}}{C_\mu}} = \kappa \sqrt{2\zeta_0} \left| A \left[\ker'\left(2\sqrt{\zeta_0}\right) + i\mathrm{kei}'\left(2\sqrt{\zeta_0}\right) \right] + B \left[\mathrm{ber}'\left(2\sqrt{\zeta_0}\right) + i\mathrm{bei}'\left(2\sqrt{\zeta_0}\right) \right] \right| \tag{2.85}$$

A relationship between the friction factor, f_{wc}, and the relative roughness parameter, A_b/k_n, can be obtained using (2.48).

$$C_\mu \frac{A_b}{k_n} = \frac{\sqrt{2}}{30\kappa\zeta_0} \sqrt{\frac{C_\mu}{f_{wc}}} \tag{2.86}$$

Equations (2.85) and (2.86) can be used in order to develop a modified wave friction factor diagram which shows the dependency of the friction factor to the relative

roughness.

The phase angle between the shear stress and the near bottom velocity is given by

$$\theta_t = \arctan\left(\frac{\Im m\left|\, A\,\left[\ker'\left(2\sqrt{\zeta_0}\right)+i\mathrm{kei}'\left(2\sqrt{\zeta_0}\right)\right]+B\,\left[\mathrm{ber}'\left(2\sqrt{\zeta_0}\right)+i\mathrm{bei}'\left(2\sqrt{\zeta_0}\right)\right]\right|}{\Re e\left|\, A\,\left[\ker'\left(2\sqrt{\zeta_0}\right)+i\mathrm{kei}'\left(2\sqrt{\zeta_0}\right)\right]+B\,\left[\mathrm{ber}'\left(2\sqrt{\zeta_0}\right)+i\mathrm{bei}'\left(2\sqrt{\zeta_0}\right)\right]\right|}\right) \tag{2.87}$$

Chapter 3

Model Results and Approximations for Applications

In the present chapter, the results of the models are shown in the form of friction factor diagrams, phase angle diagrams, and α_r diagrams. The selection of α is discussed for each flow model type and approximate formulas to represent the results analytically are presented. Additional approximations for the three-layered Barreto-Acobe model are developed and two preferred models are selected and presented based on physical and mathematical plausibility. A procedure for obtaining predictions of the current velocity profile using the preferred models is then outlined. Lastly, an example calculation is given for a possible method of specifying the current motion.

3.1 Selection of α and Boundary Layer Thickness

A model's velocity profile should contain the information needed in order to define boundary layer thickness with reasonable accuracy. The selection of α, the fraction over which the eddy viscosity varies linearly in the wave boundary layer, is critical for the application of each flow model presented in Chapter 2. The original and modified two-layer Grant-Madsen (1979 and 1986) models treat α as a fitting param-

eter that must be determined using available laboratory and field data. Madsen and Salles (1998) later suggested treating α as a function of relative roughness with their two-layer model. Madsen and Wikramanayake (1991) and Styles and Glenn (2000 and 2002) treat α as a fitting parameter with their three-layer models but Barreto-Acobe (2001) suggested that α does not have to be a fitting parameter when used in conjunction with her three-layer flow model.

3.1.1 Constant α

The fitting parameter, α, defines the height of the wave boundary layer for the Grant-Madsen models. The wave boundary layer thickness is obtained by requiring the orbital velocity to approach the free stream velocity to within a small fraction of the free stream velocity. Grant (1977) and Grant and Madsen (1979) originally suggested a value of 2. Later, Grant and Madsen (1986) updated the value of this fitting parameter and suggested that the value of α is a scaling constant between 1 and 2, depending on the data available. The selection of the α-value involves a compromise made by comparison of predictions and observations. For their three-layer model, Madsen and Wikramanayake (1991) proposed that a value of 0.5 be selected as the value of the free parameter α. Styles and Glenn (2002) used $\alpha = 0.15$, 0.3, and 0.5 for field data collected off the southern coast of New Jersey in $1994 - 1995$ in conjunction with their three-layer model.

3.1.2 α as a Function of Roughness

Madsen and Salles (1998) suggested that the value of α is a function of the relative roughness and should not be treated as a single constant. They defined the wave boundary layer thickness as the value of z for which the velocity magnitude is within 5% of the free stream velocity. They expressed α as

$$\alpha = \gamma \exp\left(2.96\left[\frac{C_\mu A_b}{k_n}\right]^{-0.071} - 1.45\right) \tag{3.1}$$

regarding γ as a fitting parameter to be based on comparison with data available. Using $\gamma = 1$, Madsen and Mathisen (1996) obtained good agreement for large roughness values. However, they used $\gamma = 1/3$ in order to obtain good agreement with the numerical results of Davies et al. (1998) for intermediate roughness values. For $C_\mu A_b/k_n = 100$ and $\gamma = 1$, (3.1) yields $\alpha = 2.0$, which is in agreement with the original value suggested by Grant and Madsen (1979).

3.1.3 α as a Function of Boundary Layer Thickness

Barreto-Acobe (2001) suggested that α in a three-layer model does not have to be a fitting parameter determined from wave-current flow data as it is in the original Grant-Madsen and modified Grant-Madsen two-layer models. A transition height was adopted for the eddy viscosity based on an explanation supporting experimental data obtained for the region where $z/\delta < 0.15$ by Daily and Harleman (1966). The wave boundary layer height, z_m, was selected as the location where the maximum velocity is predicted. The location, z_r, where the eddy viscosity transitions from linearly increasing to constant is defined as 15% of the wave boundary layer height. The subscript r is used to indicate the location where the eddy viscosity changes from linearly increasing to constant and represents the real physical distance above the bottom boundary. In non-dimensional terms,

$$\zeta_m = \frac{z_m + z_b}{l} \tag{3.2}$$

and

$$\alpha_r = \frac{z_r}{l} = 0.15\frac{z_m}{l} = 0.15\left(\zeta_m - \zeta_b\right) \tag{3.3}$$

where α_r is the normalized distance above the bottom where the eddy viscosity transition occurs.

In terms of the parameter α

$$\alpha = \frac{z_r + z_b}{l} = \alpha_r + \zeta_b \tag{3.4}$$

where

$$\zeta_b = \frac{z_b}{l} \tag{3.5}$$

3.2 Approximate Equations

Approximate equations for the modified two-layered Grant-Madsen model type as well as the three-layered Barreto-Acobe model are presented below. Additional approximations for the three-layered Barreto-Acobe model are developed in Section 3.2.2.

3.2.1 Approximations to the Grant-Madsen Models

Approximations to the modified two-layered Grant-Madsen model and the modified Madsen-Salles (1998) model are presented in the following sections.

Modified Grant-Madsen Model

The friction factor for the modified Grant-Madsen model may be approximated by the following

$$f_{wc} = C_\mu \exp\left\{ A \left(\frac{C_\mu A_b}{k_n} \right)^{-B} - C \right\} \tag{3.6}$$

where C_μ and μ are defined in Chapter 2 and the constants A, B, and C are given in Table 3.1 for the applicable ranges of relative roughness. These values were used by Madsen (1994) in application with his two-layered modified flow model with constant α.

Table 3.1: Parameters for the friction factor equation for the modified Grant-Madsen model (3.6)

Range of Application	**A**	**B**	**C**
$0.2 < \frac{C_\mu A_b}{k_n} < 10^2$	7.02	0.078	8.82
$10^2 < \frac{C_\mu A_b}{k_n} < 10^4$	5.61	0.109	7.30

The phase angle (in degrees) between the shear stress and the near bottom velocity may be approximated by the explicit relationship

$$\theta_t = 33 - 6 \left[\log_{10} \left(\frac{C_\mu A_b}{k_n} \right) \right] \quad \text{for} \quad 0.2 < \frac{C_\mu A_b}{k_n} < 10^3 \tag{3.7}$$

For $\frac{C_\mu A_b}{k_n} > 10^3$, the following explicit formula may be used

$$\theta_t = \arcsin \left(\frac{\pi/2}{\ln\left(2.7\sqrt{f_{wc}} \frac{C_\mu A_b}{k_n} \right)} \right) \quad \text{for} \quad \frac{C_\mu A_b}{k_n} > 10^3 \tag{3.8}$$

Madsen-Salles Model

The friction factor for the Madsen-Salles model may also be approximated by the expression given by (3.6) with the constants A, B, and C given in Table 3.2 for the applicable ranges of relative roughness.

The phase angle (in degrees) between the shear stress and the near bottom velocity may be approximated by the explicit relationship

$$\theta_t = \begin{cases} 38.1 - 8.3\left[\log_{10}\left(\frac{C_\mu A_b}{k_n}\right)\right] & \text{for } 0.2 < \frac{C_\mu A_b}{k_n} < 10^2 \\ 30.6 - 4.7\left[\log_{10}\left(\frac{C_\mu A_b}{k_n}\right)\right] & \text{for } 10^2 < \frac{C_\mu A_b}{k_n} < 10^4 \end{cases} \tag{3.9}$$

These expressions were obtained by Salles (1997) from application of his two-layered modified flow model with α given by (3.1) and $\gamma = 1$.

Table 3.2: Parameters for the friction factor equation for the Madsen-Salles model (3.6)

Range of Application	**A**	**B**	**C**
$0.2 < \frac{C_\mu A_b}{k_n} < 10^2$	8.89	0.059	10.68
$10^2 < \frac{C_\mu A_b}{k_n} < 10^4$	5.63	0.106	7.33

3.2.2 Barreto-Acobe Model Approximations

The equations necessary for the application of the Barreto-Acobe (2001) model are given below. The friction factor for the Barreto-Acobe model is equivalent to the friction factor approximation presented for the Grant-Madsen model in (3.6) and Table 3.1 with the upper limit of relative roughness extended to 10^6.

An approximate analytical formula for the determination of α_r was given by Barreto-Acobe (2001)

$$\alpha_r = Y \exp\left\{1.2\left(\frac{C_\mu A_b}{k_n}\right)^{-0.2} - 2.12\right\} - 0.02\left(\frac{C_\mu A_b}{k_n}\right)^{-0.3} \tag{3.10}$$

where Y is a factor that depends on ε.

$$Y = \begin{cases} S\varepsilon + I & \text{for } S\varepsilon + I \leq 1 \\ 1 & \text{for } S\varepsilon + I \geq 1 \end{cases} \tag{3.11}$$

where

$$S = -0.026\left[\log_{10}\left(\frac{C_\mu A_b}{k_n}\right)\right]^2 + 0.284\left[\log_{10}\left(\frac{C_\mu A_b}{k_n}\right)\right] + 0.942 \tag{3.12}$$

and

$$I = -0.013\left[\log_{10}\left(\frac{C_\mu A_b}{k_n}\right)\right] + 0.712 \tag{3.13}$$

Note that $\alpha = \alpha_r + \zeta_b$ where ζ_b is defined in equation (3.5).

Additional Approximations for the Barreto-Acobe Model

Additional approximations for the Barreto-Acobe model have been developed and are presented below. The friction factor for the Barreto-Acobe model is again defined by (3.6) where C_μ and μ are defined in Chapter 2 and the constants A, B, and C are given in Table 3.3 for the applicable ranges of relative roughness.

An approximation for the determination of α_r is

$$\alpha_r = \exp\left\{A\left(\frac{C_\mu A_b}{k_n}\right)^{-B} - C\right\} \tag{3.14}$$

where the constants A, B, and C are given in Table 3.4 for the applicable ranges of relative roughness. For $\varepsilon < 0.2$, the effect of the current is negligible when compared

to the waves. Hence, $\varepsilon < 0.2$ is considered *pure wave* motion. Therefore, when using Table 3.4, $\varepsilon = 0.2$ must be used for values of ε less than 0.2 in order to obtain accurate results.

The phase angle (in degrees) between the shear stress and the near bottom velocity

Table 3.3: Parameters for the friction factor equation for the modified Barreto-Acobe model (3.6)

Range of Application	**A**	**B**	**C**
$0.1 < \frac{C_\mu A_b}{k_n} < 10^3$	6.19	0.087	8.05
$10^3 < \frac{C_\mu A_b}{k_n} < 10^6$	5.77	0.086	7.83

may be approximated by the explicit relationship

$$\theta_t = \begin{cases} 40 - 5\left[\log_{10}\left(\frac{C_\mu A_b}{k_n}\right)(1+\varepsilon)\right] & 10^{-1} < \frac{C_\mu A_b}{k_n} < 10^3 \\ \arcsin\left(\frac{\pi}{2\kappa}\sqrt{f_{wc}}\right)(1.1 - 0.5\varepsilon) & 10^3 < \frac{C_\mu A_b}{k_n} < 10^6 \end{cases} \tag{3.15}$$

Also note that if $\theta_t > 45$ degrees , then $\theta_t = 45$ degrees and again note that if $\varepsilon < 0.2$, then $\varepsilon = 0.2$ must be used with (3.15).

Table 3.4: Parameters for the α_r equation for the modified Barreto-Acobe model (3.14). Note that if $\varepsilon < 0.2$, then $\varepsilon = 0.2$ must be used.

Range of Application	$0.1 < \frac{C_\mu A_b}{k_n} < 10^3$	$10^3 < \frac{C_\mu A_b}{k_n} < 10^6$
A	$1.07\exp\left[-0.681\left(\varepsilon - 0.2\right)\right]$	$1.02\exp\left[-0.715\left(\varepsilon - 0.2\right)\right]$
B	$0.214\exp\left[-0.168\left(\varepsilon - 0.2\right)\right]$	$0.17\exp\left[-1.53\left(\varepsilon - 0.2\right)\right]$
C	$2.07\exp\left[-0.757\left(\varepsilon - 0.2\right)\right]$	$2.13\exp\left[-0.47\left(\varepsilon - 0.2\right)\right]$

3.3 Model Results

The results of the two-layer original and modified Grant-Madsen (1979, 1986) models, two-layer Madsen-Salles (1998) model, and the three-layer Barreto-Acobe (2001) model are shown in the form of a friction factor diagram (Figure 3-1), phase angle diagrams (Figures 3-2, 3-3, and 3-4), and an α_r diagram (Figure 3-5).

The approximate formulas for the friction factor, f_{wc}, are in agreement for two-layer modified Grant-Madsen model and Madsen-Salles model presented in Chapter 2. Note that the primary difference between the original and modified Grant-Madsen type models is in the evaluation of the shear stress, i.e. the original Grant-Madsen model evaluates the shear stress at the limit of $z + z_b \to 0$ while the modified Grant-Madsen model evaluates the shear stress at $z + z_b = z_0$. The friction factor is fairly insensitive to these differences in shear stress evaluation for small roughness values. However, there is an appreciable difference in friction factors when dealing with large roughness values. Figures 3-2, 3-3, and 3-4 depict the phase angle between the shear stress and near-bottom velocity. A physical inconsistency of the original Grant-Madsen model is clearly shown in Figure 3-2 where the phase grows unrealistically large for large roughness values. The phase difference for the modified Grant-Madsen model, which evaluates the shear stress at $z + z_b = z_0$, produces realistic results, as depicted in Figure 3-2. Notice that for small roughness values, the phase difference for the original and modified Grant-Madsen models are in agreement.

3.4 Selection of Preferred Flow Models

In the original two-layer Grant-Madsen (1979, 1986) model, there is an inconsistency in the model based on the definition of the eddy viscosity used in the wave problem and the current problem. Also, it is known that the wave-associated turbulence at the upper edge of the wave boundary layer should approach zero. Therefore, the increasing eddy viscosity defined in (2.17) for all heights above the bottom boundary that

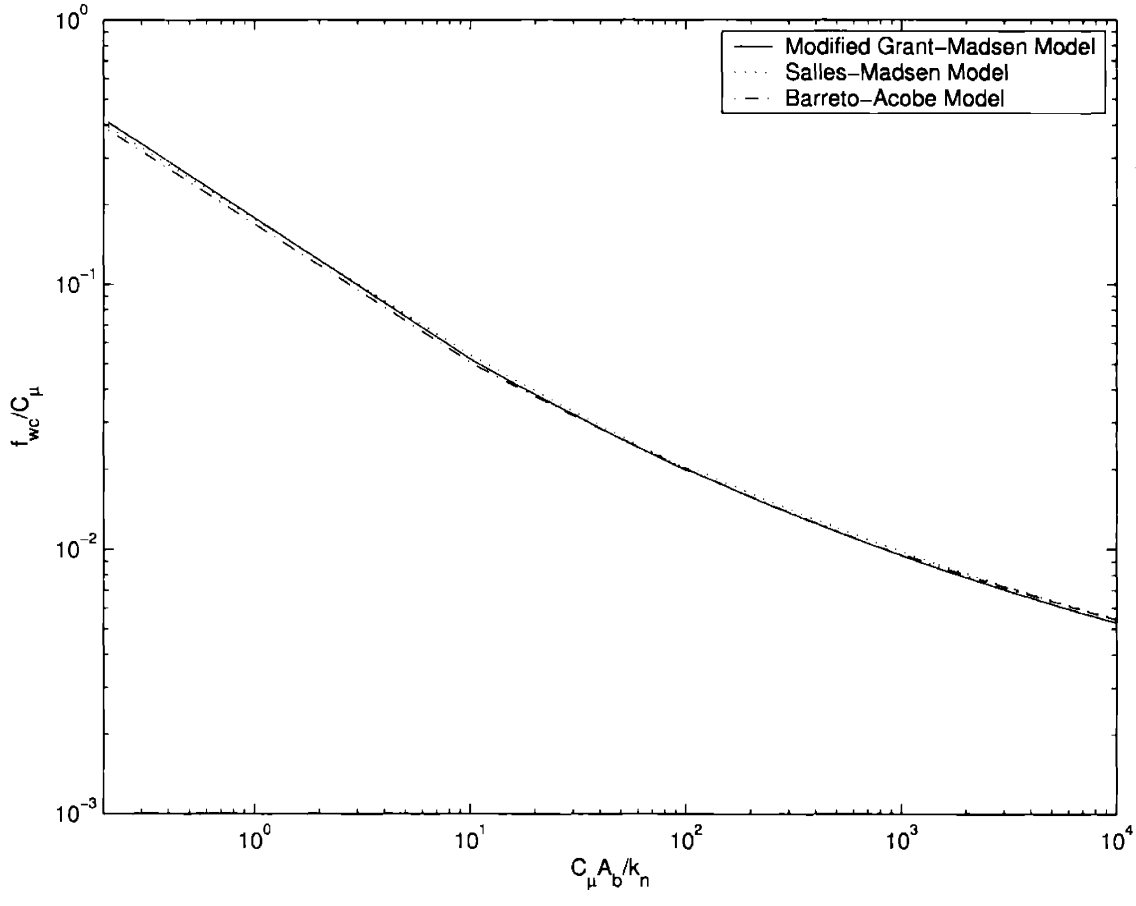

Figure 3-1: Comparison of friction factor equations (3.6) for the two-layer modified Grant-Madsen (1994) model (Table 3.1), the two-layer Salles-Madsen (1998) model (Table 3.2), and the three-layer Barreto-Acobe (2001) model (Table 3.3)

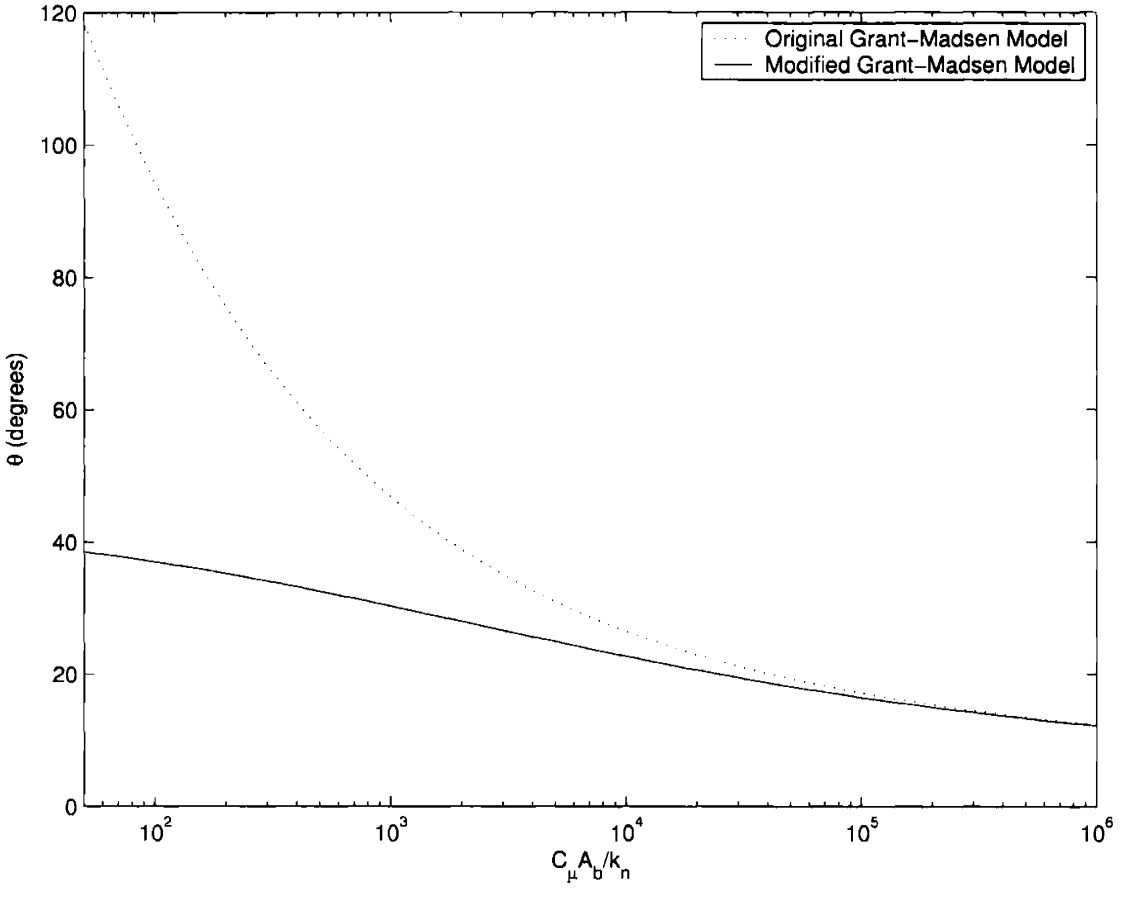

Figure 3-2: Phase angle diagram for the original two-layer Grant-Madsen model (2.57) and the modified two-layer Grant-Madsen model (2.58)

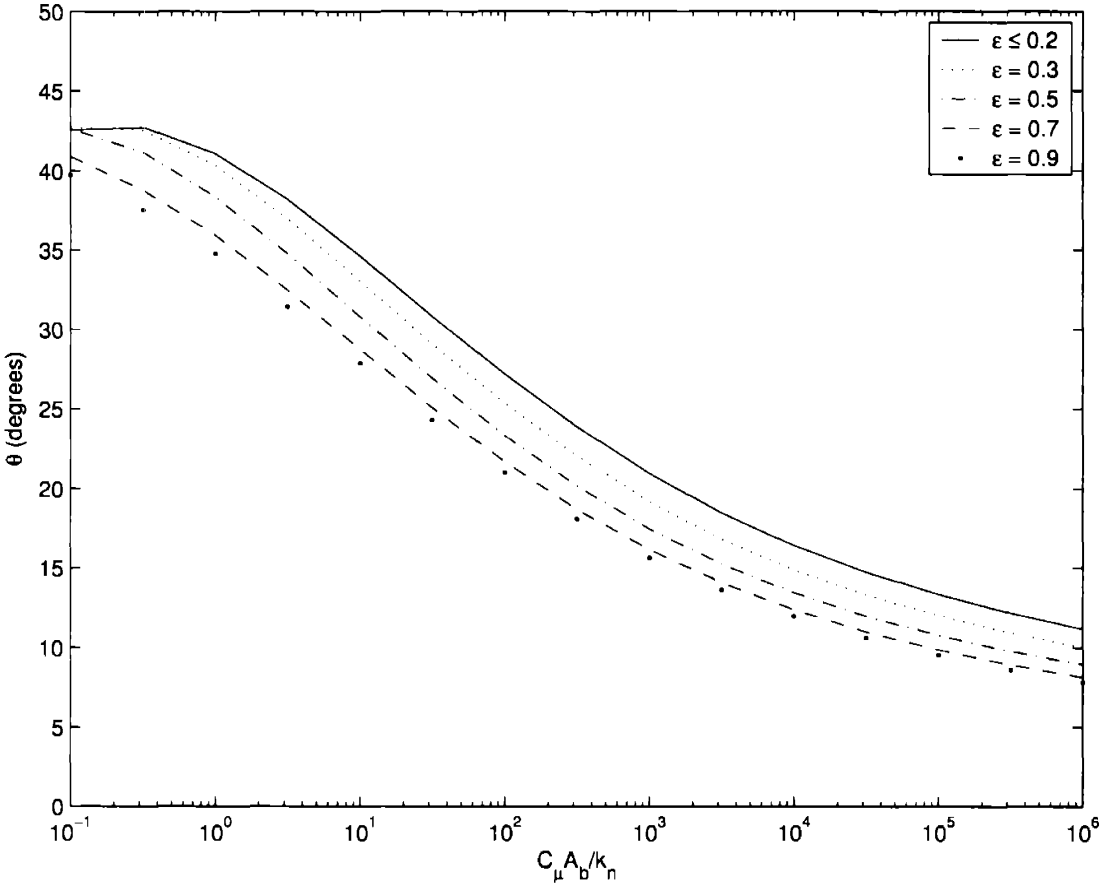

Figure 3-3: Phase angle diagram for waves and currents for the three-layer Barreto-Acobe (2001) model for various ε values (2.87)

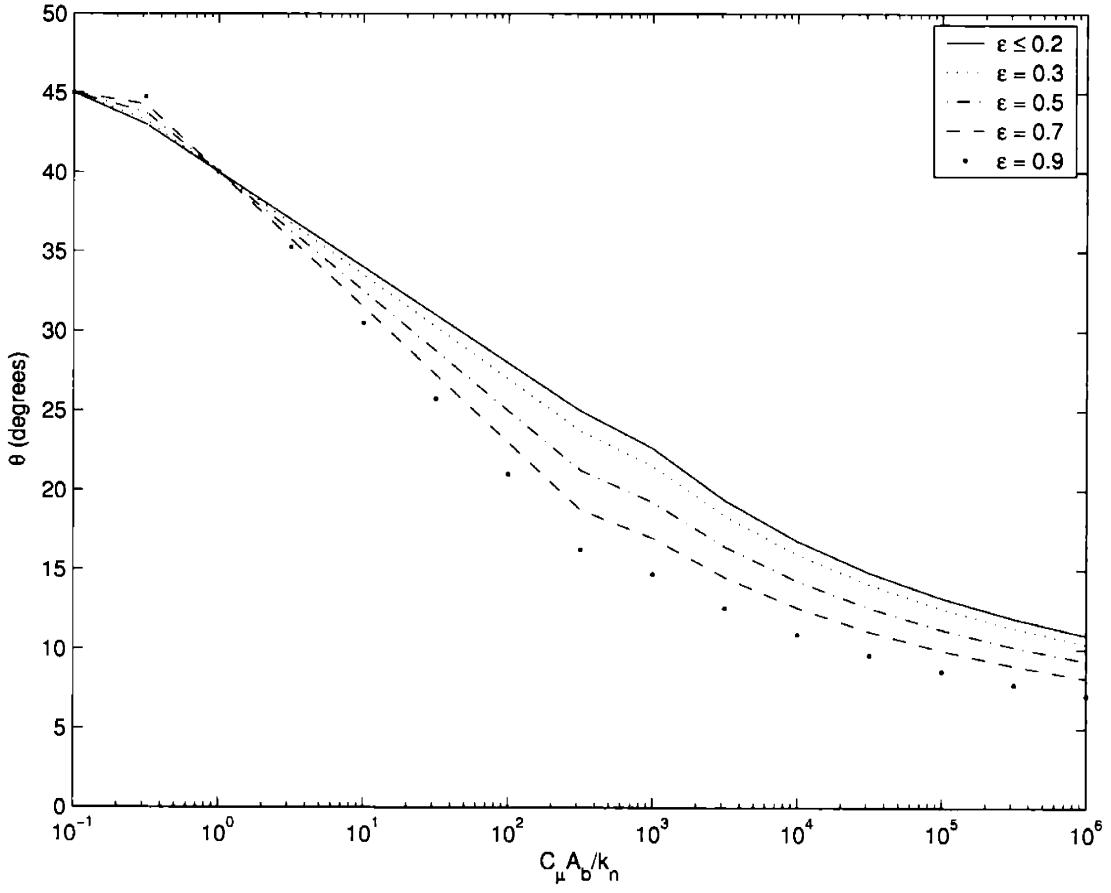

Figure 3-4: Phase angle diagram for waves and currents for the three-layer Barreto-Acobe approximation given in (3.15) for various ε values. Note that 45° is the maximum value for the phase difference.

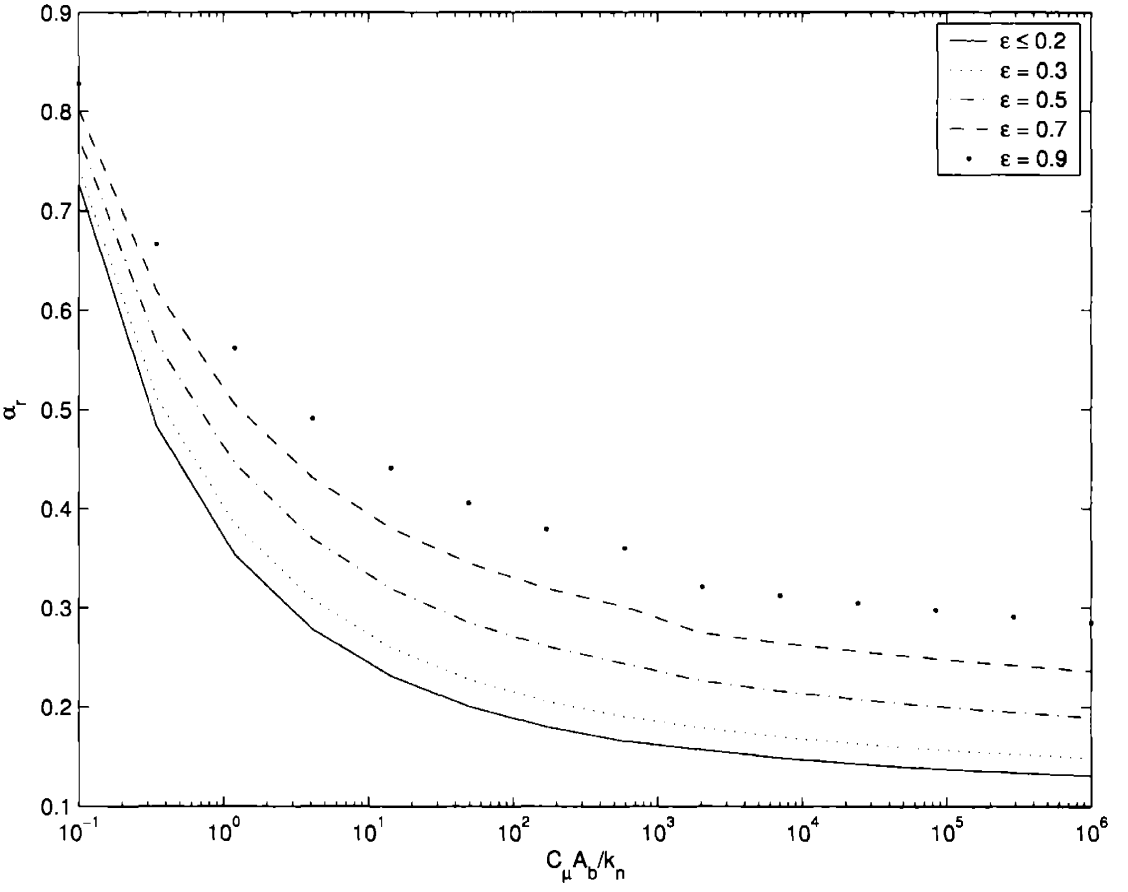

Figure 3-5: α_r diagram for waves and currents for the three-layer Barreto-Acobe approximation given in (3.14) for various ε values

is used for the solution of the wave problem is physically unrealistic. Furthermore, since the eddy viscosity is discontinuous, the resulting velocity profile is not smooth. The original Grant-Madsen model works well for small distances above the bottom (i.e. the wave-dominated region) and for heights within the current boundary layer that are not influenced by the wave boundary layer. However, it does not accurately predict the current velocity for the transition region in between the wave-dominated region and the current-dominated region. In addition, the model performs poorly for large roughnesses because it inherently evaluates the bottom boundary condition (no-slip) at $z = z_0$ and there can be a large gap in the velocity profile for $0 < z < z_0$ when dealing with large roughness elements.

Madsen and Salles (1998) developed a two-layer eddy viscosity model specially designed for very rough bottoms. They discovered that the wave boundary layer thickness is not simply proportional to the boundary layer length scale, i.e. α is not a constant. Instead, they found α to be a function of the relative roughness, as given in (3.1). Even though α is no longer a free parameter in their model, it is a function of a fitting parameter, γ in (3.1). A significant improvement of this model when compared to previous model developments is that the bottom boundary, no-slip condition can be applied at $z = 0$ by introducing the translation distance $z_b = z_0$. The result is a velocity profile that is identical to that of the classical Grant-Madsen model, but shifted downward so that the no-slip condition is applied at $z = 0$. Therefore, this model prevents the prediction of negative velocities for small values of z. A shortcoming of their model is that a fitting parameter is still involved and no single value of γ in (3.1) works well for all data sets as discussed in Section 3.1.2.

Madsen and Wikramanayake (1991) developed a three-layer eddy viscosity model removing some of the shortcomings of the original Grant-Madsen model. Two major improvements in their model include the use of the same eddy viscosity definition for both the wave and current problems and the use of a continuous eddy viscosity which results in a velocity profile that is smooth. However, there is still a model-specific

fitting parameter, α, that must be determined for each application of the model. No single value of the fitting parameter works well for all data sets and a compromise must always be made depending on the data available. Since the model evaluates the bottom boundary, no-slip condition at $z = z_0$, there can be a large gap in the velocity profile for $0 < z < z_0$ when dealing with large roughness elements as is the case with the original Grant-Madsen model. Hence, the improved model also performs well for small roughnesses but does not perform very well for large roughnesses.

Barreto-Acobe (2001) developed a three-layer model that could apply the bottom boundary, no-slip condition at either $z = 0$ or $z = z_0$. Her eddy viscosity model provides a continuous transition between the region where the turbulence is dominated by wave motion and the region where the turbulence is dominated by the current. The three-layered Barreto-Acobe model provides a transition point between the wave and current dominated regions that is a pre-set fraction of the boundary layer height as determined by previous boundary layer laboratory experiments. This means that the model is entirely predictive and the dependence on application-specific fitting parameters is eliminated.

Based on the above discussion, the two preferred models that will be used throughout the remainder of this text are the Madsen and Salles (1998) two-layer model and the Barreto-Acobe (2001) three-layer model. These models are the most physically realistic since they allow the bottom boundary no-slip condition to be applied at $z = 0$. It is also highly desirable that α is not simply a constant in each of these models. α is not a fitting parameter in the three-layer Barreto-Acobe flow model, whereas α is a function of the relative roughness and γ, a fitting parameter, for the two-layer Madsen-Salles flow model.

3.5 Solution Procedure for Practical Applications

In this section, practical problems will be solved using the approximate formulas presented in Section 3.2 for the preferred models.

3.5.1 Specifications

The wave motion is specified in terms of its period, T, and the near-bottom orbital velocity predicted by potential theory, U_b. There are two ways to specify the current: (1) by a current shear stress, τ_c, and its direction relative to the wave motion, ϕ_{wc} or (2) by its magnitude at a certain height above the bottom, u_c at $z = z_{ref}$, and its direction relative to the wave motion, ϕ_{wc}. The bottom roughness must also be specified as an equivalent Nikuradse sand grain roughness, k_n. The relative roughness parameter, A_b/k_n, is determined using wave and roughness characteristics. In other words,

$$k_n = 30z_0, \quad \omega = \frac{2\pi}{T}, \quad \text{and} \quad A_b = \frac{U_b}{\omega}$$

3.5.2 Current Specified by Current Shear Stress

The following solution procedures are applicable for the two-layered modified Grant-Madsen model and the three-layered Barreto-Acobe model if the current is specified by its current shear stress, τ_c , and its direction relative to the wave motion, ϕ_{wc}

Two-layer Solution Procedure

1. With the current shear stress and fluid density known, determine the current shear velocity

$$u_{*c} = \sqrt{\frac{\tau_c}{\rho}} \tag{3.16}$$

2. Then, for the first iteration, assume $\mu \approx 0$ and $C_\mu = 1$.

3. Determine the friction factor, f_{wc}, from (3.6) and Table 3.2 paying special attention

to the relative roughness parameter and range of application.

4. Calculate the wave shear velocity, u_{*w}, from

$$u_{*w} = \sqrt{\frac{1}{2} f_{wc} U_b} \tag{3.17}$$

5. Find the new value of μ, using

$$\mu = \frac{u_{*c}}{u_{*w}} \tag{3.18}$$

6. Determine the new value of C_μ, from

$$C_\mu = \sqrt{1 + 2\mu^2 \left|\cos \phi_{wc}\right| + \mu^4} \tag{3.19}$$

7. Repeat Steps 3 through 5 until C_μ converges. Three significant figures is sufficient precision.

8. Calculate u_{*m} and l from

$$u_{*m} = u_{*w} \sqrt{C_\mu} \quad \text{and} \quad l = \frac{\kappa u_{*m}}{\omega} \tag{3.20}$$

9. Calculate α from (3.1) paying special attention to the relative roughness parameter and range of application and using $\gamma = 1$. Later, the value for the fitting parameter, γ, can be adjusted based on available data.

10. For applications with the two-layer modified Grant-Madsen model with $z_b = z_0$,

$$\zeta_b = \zeta_0 = \frac{z_0}{l} \tag{3.21}$$

11. The current profile can now be determined using the equations outlined in Section 2.2.1.

Three-layer Solution Procedure

1. With the current shear stress and fluid density known, determine the current shear velocity

$$u_{*c} = \sqrt{\frac{\tau_c}{\rho}} \tag{3.22}$$

2. Then, for the first iteration, assume $\mu \approx 0$ and $C_\mu = 1$.

3. Determine the friction factor, f_{wc}, from (3.6) and Table 3.3 paying special attention to the relative roughness parameter and range of application.

4. Calculate the wave shear velocity, u_{*w}, from

$$u_{*w} = \sqrt{\frac{1}{2} f_{wc} U_b} \tag{3.23}$$

5. Find the new value of μ, using

$$\mu = \frac{u_{*c}}{u_{*w}} \tag{3.24}$$

6. Determine the new value of C_μ, from

$$C_\mu = \sqrt{1 + 2\mu^2 \left|\cos \phi_{wc}\right| + \mu^4} \tag{3.25}$$

7. Repeat Steps 3 through 5 until C_μ converges. Three significant figures is sufficient precision.

8. Calculate u_{*m}, ε, and l from

$$u_{*m} = u_{*w}\sqrt{C_\mu}, \quad \varepsilon = \frac{u_{*c}}{u_{*m}}, \quad \text{and} \quad l = \frac{\kappa u_{*m}}{\omega} \tag{3.26}$$

9. Calculate α_r from (3.14) and Table 3.4 paying special attention to the relative roughness parameter and range of application.

10. For applications with the three-layer Barreto-Acobe model with $z_b = z_0$,

$$\zeta_b = \zeta_0 = \frac{z_0}{l} \quad \text{and} \quad \alpha = \alpha_r + \zeta_b \tag{3.27}$$

11. The current profile can now be determined using the equations outlined in Section 2.2.2.

3.5.3 Current Specified by Current Velocity at Reference Height

The following solution procedures are valid for a current that is specified by its magnitude at a certain height above the bottom, u_c at $z = z_{ref}$, and its direction relative

to the wave motion, ϕ_{wc} when using the preferred models presented in Section 3.4. For this procedure, we assume that the reference height is in the upper layer, i.e. $z_{ref} + z_b > \alpha l$ for the two-layer Grant-Madsen model and $z_{ref} + z_b > \alpha l/\varepsilon$ for the three-layer Barreto-Acobe model. For most cases, this assumption is valid because most of the water depth is within this layer.

Two-layer Solution Procedure

1. Solve wave-current interaction (Steps 3-10 of Section 3.5.2) assuming $u_{*c} = 0$ for the first iteration and obtain u_{*m}, l, and α.
2. Use these values of u_{*m}, l, and α in the equation governing the current in the upper region (2.39) in order to solve for u_{*c}. After rearrangement, this equation is

$$0 = \frac{u_{*c}}{\kappa}\left[\ln\left(\frac{z_{ref} + z_b}{\alpha l}\right) + \frac{u_{*c}}{u_{*m}}\left[\ln\left(\frac{\alpha l}{z_0}\right)\right]\right] - u_c \tag{3.28}$$

3. With the new estimate of u_{*c} obtained in Step 2, repeat Steps 1 and 2 until the value of u_{*c} converges.
4. Verify the assumption $z_{ref} + z_b > \alpha l$.

Three-layer Solution Procedure

1. Solve wave-current interaction (Steps 3-10 of Section 3.5.2) assuming $u_{*c} = 0$ for the first iteration and obtain u_{*m}, l, and α.
2. For the first approximation of u_{*c} , assume that $\left[\ln\left(\frac{z_{ref}+z_b}{\alpha l/\varepsilon}\right)\right]$ is small (no estimate of ε is available). Then, the equation governing the current in the upper region (2.81) simplifies to

$$0 = \frac{u_{*c}}{\kappa}\left[1 + \frac{u_{*c}}{u_{*m}}\left[\ln\left(\frac{\alpha l}{z_0}\right) - 1\right]\right] - u_c \tag{3.29}$$

3. Solve (3.29) for u_{*c} using the values of u_{*m}, l, and α obtained in Step 1.
4. Solve wave-current interaction (Steps 3-10 of Section 3.5.2) with this u_{*c} in order

to obtain new values for u_{*m}, l, and α and to obtain an initial estimate of ε.

5. Use this estimate of ε in the $\left[\ln\left(\frac{z+z_b}{\alpha l/\varepsilon}\right)\right]$ term of the equation governing the current in the upper region (2.81). After rearrangement, this equation is

$$0 = \frac{u_{*c}}{\kappa}\left[\ln\left(\frac{z_{ref}+z_b}{\alpha l/\varepsilon}\right)+1+\frac{u_{*c}}{u_{*m}}\left[\ln\left(\frac{\alpha l}{z_0}\right)-1\right]\right]-u_c \tag{3.30}$$

6. Solve (3.30) for u_{*c} using the values of u_{*m}, l, α, and ε obtained in Step 4.

7. With the new estimate of u_{*c} obtained in Step 6, repeat Steps 4 and 6 until the value of u_{*c} converges.

8. Verify the assumption $z_{ref}+z_b > \alpha l/\varepsilon$.

3.6 Example

The conditions specified in the following example correspond to measurements obtained at the LEO-15 site off the coast of southern New Jersey and used by Styles and Glenn (2002). The results of the full preferred models for this data set are shown in Chapters 4 and 5.

3.6.1 Example of Current Specified by Current Velocity at a Reference Height, Roughness Unknown

Four current meters were deployed at 45, 80, 165, and 250 cm above the bottom. Horizontal resultant velocities and angles were calculated for each location and a best fit law-of-the-wall logarithmic velocity profile was used in order to determine the current velocity at a reference elevation.

The wave parameters are

$$U_b = 21.65 \text{ cm/sec} \quad \text{and} \quad A_b = 35.05 \text{ cm}$$

For this problem, the current velocity is specified at a reference height as follows:

$$u_c = 8.4 \text{ cm/sec} \quad \text{at} \quad z_{ref} = 250 \text{ cm}$$

The angle between waves and current is

$$\phi_{wc} = 20.8 \text{ deg}$$

This is a difficult problem to solve because the equivalent roughness is not known. In order to solve this problem with a bottom boundary layer, wave-current interaction flow model, an initial value of k_n is assumed ($k_n = 1$ cm, for example). Next, an initial value of C_μ is assumed ($C_\mu = 1$, corresponding to a case of pure waves, is a good first approximation). From the initial estimate of C_μ and k_n, the relative roughness ratio is calculated. This ratio is used in order to determine f_{wc} (using (3.6) and Table 3.2 for the two-layer model and Table 3.3 for the three-layer model), and subsequently τ_{wm}, u_{*w}, and μ^2. C_μ is calculated using μ^2 and compared with the initial C_μ guess. If the two results are not in agreement, then the procedure is repeated with the latter value of C_μ used as the new initial estimate for the procedure. Once the C_μ values converge, ε is calculated. Following the determination of ε, u_{*m}, l, z_0, and z_b are calculated. Finally, α is determined (using (3.1) for the two-layer preferred model and (3.14) and Table 3.4 for the three-layer model) and a theoretical velocity is calculated at a pre-selected reference height and compared with the measured velocity at said reference height. If the two velocities are not equivalent, then a new k_n is chosen and the entire procedure is repeated until the measured and calculated velocities converge (i.e. for every value of k_n, a new C_μ must be determined).

Model Results

The results obtained with the two-layer Madsen-Salles model with variable α are shown in Table 3.5. The results obtained with the three-layer Barreto-Acobe model with α not a fitting parameter are shown in Table 3.6. Resulting velocity profiles for the three-layer Barreto-Acobe model and the two-layer Madsen-Salles model with $\gamma = 1/4$ and $\gamma = 1$ are shown in Figures 3-6 and 3-7.

Table 3.5: Results of two-layer Madsen-Salles model with variable α for range of $\gamma = 1/4, 1/3, 1/2, 1$

	$\gamma = 1/4$	$\gamma = 1/3$	$\gamma = 1/2$	$\gamma = 1$
k_n (cm)	37	24	14	6
z_0 (cm)	1.24	0.81	0.45	0.19
u_{*m} (cm/sec)	6.57	5.91	5.16	4.24
u_{*w} (cm/sec)	6.53	5.85	5.10	4.16
l (cm)	4.26	3.83	3.34	2.74
α	1.12	1.36	1.82	3.06

Table 3.6: Results of three-layer Barreto-Acobe model with α not a fitting parameter

k_n	19 cm
z_0	0.63 cm
u_{*m}	5.39 cm/sec
u_{*w}	5.33 cm/sec
C_μ	1.145
l	3.49 cm
α	0.48
α_r	0.3
ε	0.152

The selection of a particular bottom boundary layer flow model is of critical importance when evaluating data. Application results may vary greatly depending on the model selected and the adopted value of the fitting parameter within a particular model (if applicable). Since γ is not known a priori, the range $\gamma = 1/4$, $1/3$, $1/2$, and 1 was applied with the two-layer Madsen-Salles model for this example. The

Nikuradse sand grain roughness can vary by more than a factor of 6 depending on the value of γ selected (as shown in Table 3.5). It is expected that as γ increases, the value for the Nikuradse sand grain roughness decreases. A smaller γ-value corresponds to a smaller α-value and therefore a steeper slope for the eddy viscosity within the wave boundary layer, $z+z_b < \alpha l$. A larger k_n is therefore required in order for the velocity profile to go through the designated velocity at $z = z_{ref}$. The resulting velocity profiles for the three-layer Barreto-Acobe model and the two-layer Madsen-Salles model with $\gamma = 1/4$ and $\gamma = 1$ are shown in Figure 3-6. Notice that for $z > 10$ cm from the boundary, the profiles are identical. However, near the bottom boundary, the profiles are very different, as seen in Figure 3-7. Near-bottom characteristics are important for sediment transport since the highest sediment concentration is found near the boundary. Therefore, sediment transport calculations are very sensitive to the selection and application of a particular bottom boundary flow model. Two- and three-layer flow model applications will be discussed in greater detail in Chapters 4 and 5.

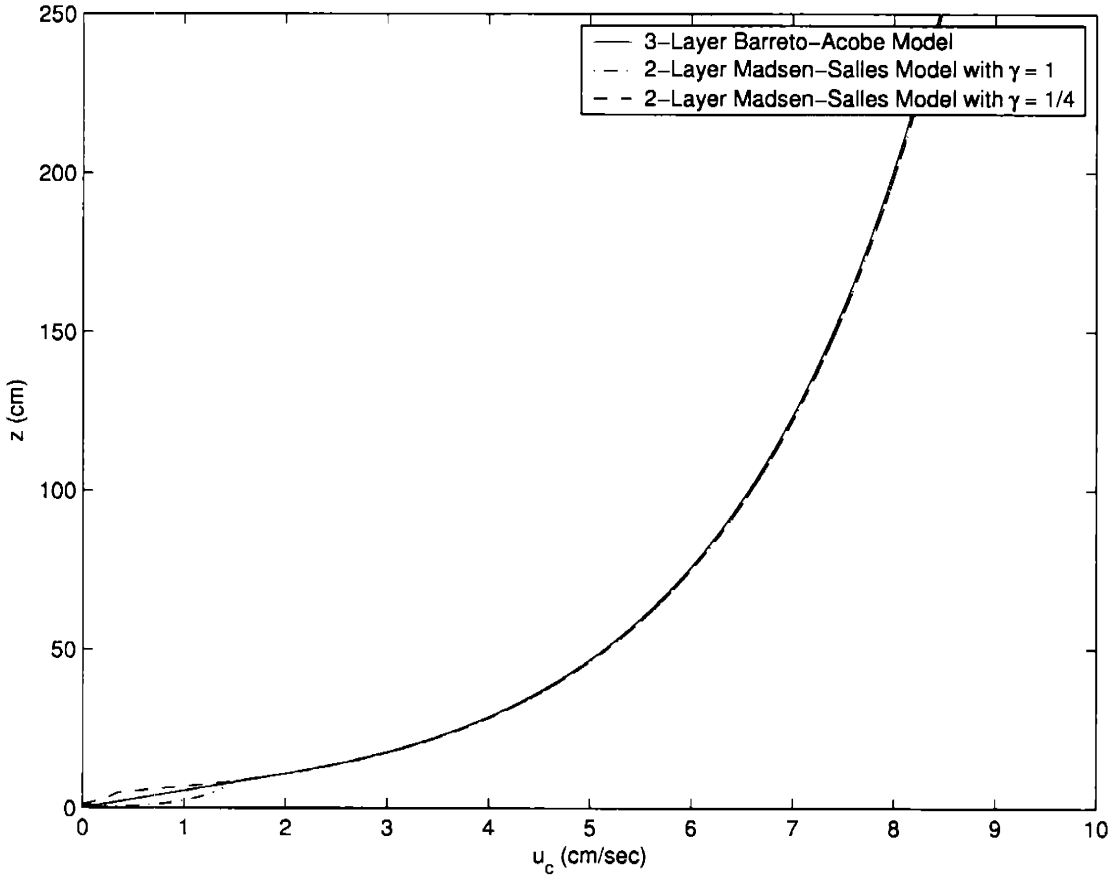

Figure 3-6: Velocity profiles for the two-layer Madsen-Salles model with $\gamma = 1/4$ and $\gamma = 1$ and the three-layer Barreto-Acobe model

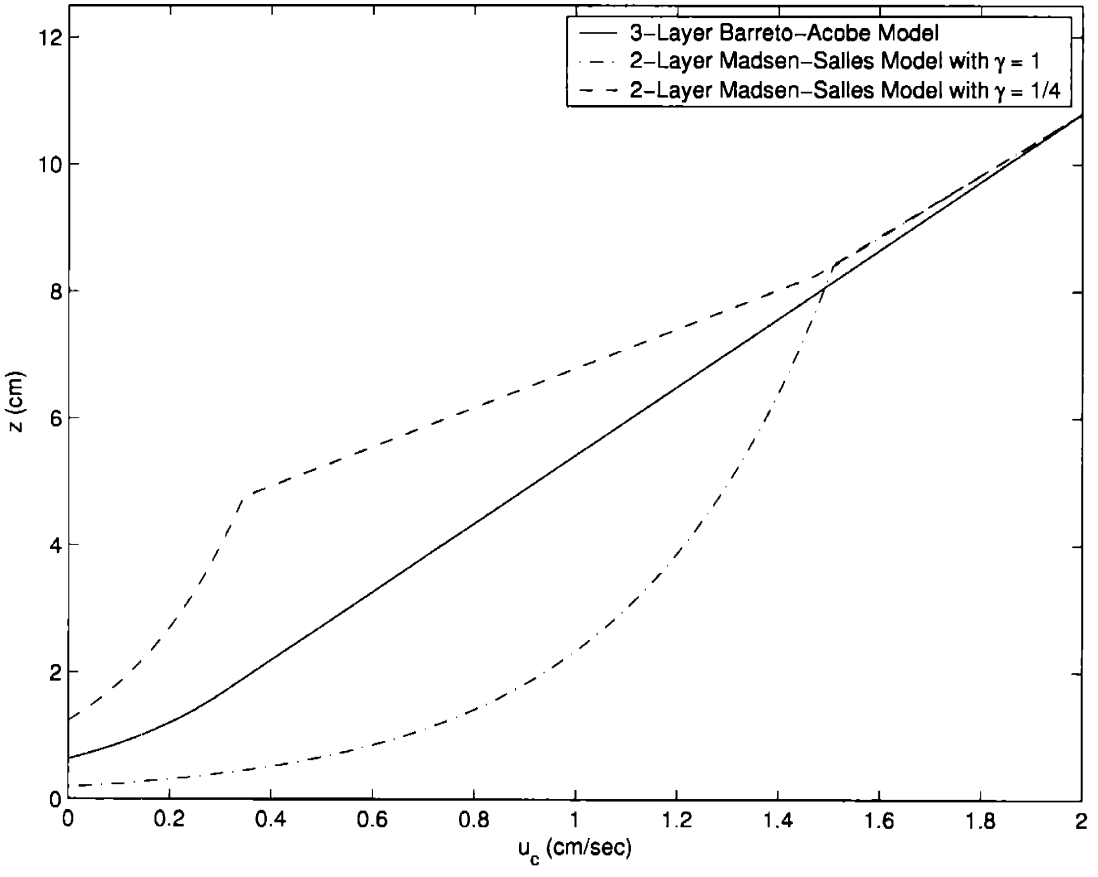

Figure 3-7: Velocity profiles near the bottom boundary for the two-layer Madsen-Salles model with $\gamma = 1/4$ and $\gamma = 1$ and the three-layer Barreto-Acobe model

Chapter 4

Ripple Geometry and Equivalent Bed Roughness

In this chapter, empirical relationships are developed in order to relate bottom roughness and ripple geometry. The two-layer Madsen-Salles and three-layer Barreto-Acobe flow models are then applied to fixed bed laboratory data collected by Bagnold (1946), Sleath (1985), and Mathisen and Madsen (1996, 1999). The preferred flow models are also applied to movable bed laboratory and field data collected by Carstens et al. (1969), Lofquist (1986), Rosengaus (1987), Mathisen (1989), and Styles and Glenn (2002). For the Mathisen and Madsen (1996) data set, both wave attenuation and current profile data are available. Therefore, wave attenuation measurements were used in order to calculate the bottom roughness for the cases of pure waves and waves in the presence of a current while current measurements were used in order to establish the bottom roughness for the case of currents in the presence of waves. Ripple geometry and roughness models based on the fixed and movable bed laboratory and field data are presented and will be used to evaluate the preferred flow models in Chapter 5.

4.1 Empirical Relationships

The formation of sediment bedforms under the influence of oscillatory waves is a consequence of fluid/sediment interaction. Bedforms will result if the near-bed velocity exceeds the critical velocity required for initiation of sediment motion. Bedforms are of practical importance because sediment transport, wave attenuation, and near-bed currents are all affected by bedform geometry.

Bottom roughness has been considered to be proportional to ripple geometry as

$$k_n = \alpha_n \eta \tag{4.1}$$

where η is the ripple height.

Bottom roughness can also be considered proportional to ripple steepness, i.e. the ratio of ripple height over ripple length as

$$k_n = \beta_n \eta \frac{\eta}{\lambda} \tag{4.2}$$

where λ is the ripple length.

In application with their flow model, Grant and Madsen (1982) suggest $\beta_n = 27.7$ when using (4.2) for steep ripples.

In the following sections, the preferred flow models are used in conjunction with fixed and movable bed data in order to establish the associated values for α_n and β_n in equations (4.1) and (4.2). All of the laboratory and field data used in this text are tabulated and reported in Appendix A through Appendix E.

4.2 Fixed Bed Data

4.2.1 Monochromatic Pure Wave Experiments

Bagnold (1946) and Sleath (1985) measured energy dissipation over beds with fixed artificial ripples using an oscillatory bed apparatus. Mathisen and Madsen (1996) used a programmable piston-type wavemaker in a 28-meter long wave flume with glass sidewalls and placed triangular bars along the bottom of the flume. Wave gages were used in order to measure wave attenuation by relating voltage output to surface displacement. Tables 4.1 and 4.2 show the mean and standard deviation values for α_n and β_n using the preferred flow models in application with monochromatic pure wave experiments.

Table 4.1: Mean and standard deviation values for α_n and β_n using the two-layer Madsen-Salles model in application with monochromatic pure wave experiments

Data Source	Number of Data Points	α_n	β_n
Bagnold (1946)	59	12.1 $\pm$4.02	80.69 $\pm$26.79
Sleath (1985)	61	4.95 $\pm$2.38	21.27 $\pm$10.22
Mathisen and Madsen (1996)	9	11.99 $\pm$6.52	89.16 $\pm$32.02

Table 4.2: Mean and standard deviation values for α_n and β_n using the three-layer Barreto-Acobe model in application with monochromatic pure wave experiments

Data Source	Number of Data Points	α_n	β_n
Bagnold	59	15.00 $\pm$4.72	100.05 $\pm$31.43
Sleath	61	6.21 $\pm$3.14	26.66 $\pm$13.47
Mathisen and Madsen (1996)	9	13.69 $\pm$6.50	103.68 $\pm$28.20

4.2.2 Spectral Pure Wave Experiments

Mathisen and Madsen (1996) also performed spectral pure wave experiments. Spectral waves problems are simplified with the introduction of a representative monochromatic wave. The representative periodic wave is defined by its near-bottom orbital velocity, U_{br}, radian frequency, ω_r, and direction of propagation, ϕ_r. Given the directional near-bottom orbital velocity spectrum, $S_{ub}(\omega, \theta)$, the representative wave orbital velocity amplitude proposed by Madsen (1994) is defined as

$$U_{br} = \sqrt{2 \iint S_{ub}(\omega, \theta)\, d\omega\, d\theta} \tag{4.3}$$

The representative wave radian frequency is defined as

$$\omega_r = \frac{\iint \omega S_{ub}(\omega, \theta)\, d\omega\, d\theta}{\iint S_{ub}(\omega, \theta)\, d\omega\, d\theta} \tag{4.4}$$

Finally, the direction of propagation of the representative periodic wave is defined as

$$\tan \phi_{wr} = \frac{\iint S_{ub}(\omega, \theta) \sin\theta\, d\omega\, d\theta}{\iint S_{ub}(\omega, \theta) \cos\theta\, d\omega\, d\theta} \tag{4.5}$$

The representative wave near-bottom orbital excursion amplitude, A_{br}, is calculated as

$$A_{br} = \frac{U_{br}}{\omega_r} \tag{4.6}$$

Tables 4.3 and 4.4 show the mean and standard deviation values for α_n and β_n using the preferred flow models in application with the spectral pure wave experiments of Mathisen and Madsen (1996).

Table 4.3: Mean and standard deviation values for α_n and β_n using the two-layer Madsen-Salles model in application with spectral pure wave experiments

Data Source	Number of Data Points	α_n	β_n
Mathisen and Madsen (1996)	3	15.46 $\pm$6.81	103.07 $\pm$45.40

Table 4.4: Mean and standard deviation values for α_n and β_n using the three-layer Barreto-Acobe model in application with spectral pure wave experiments

Data Source	Number of Data Points	α_n	β_n
Mathisen and Madsen (1996)	3	16.31 $\pm$5.33	108.75 $\pm$35.51

4.2.3 Combined Wave-Current Experiments

Mathisen and Madsen (1996) simulated wave and current boundary layer flows with a wave flume equipped with a current generation system consisting of a 1200 gpm pump and associated recirculation piping. Even though Mathisen and Madsen used 1.5 cm high triangular bars spaced at 10 cm and 20 cm intervals, only those experiments with 10 cm spacing were used for the analysis in this text because they were found to realistically represent the drag force experienced by equilibrium bedforms. Tables 4.5, 4.6, 4.7, and 4.8 show the mean and standard deviation values for α_n and β_n using the preferred flow models in application with the combined wave-current flow experiments of Mathisen and Madsen (1996). Since both wave attenuation data and current profile data are available, there are two roughness length scales to consider, namely waves in the presence of currents, k_{wc}, and currents in the presence of waves, k_{cw}. Only the wave attenuation data provided by Mathisen and Madsen (1996) were used in order

to obtain the α_n and β_n values reported in Tables 4.5 and 4.6. Tables 4.7 and 4.8 show α_n and β_n values when only the current profile measurements were used with the two-layer Madsen-Salles model (with $\gamma = 1$) and the three-layer Barreto-Acobe flow model.

Table 4.5: Mean and standard deviation values for α_n and β_n using the two-layer Madsen-Salles model with wave attenuation data in application with combined wave/current experiments

Data Source	Number of Data Points	α_n	β_n
Mathisen and Madsen (1996)	9	17.43 $\pm$6.91	145.46 $\pm$34.00

Table 4.6: Mean and standard deviation values for α_n and β_n using the three-layer Barreto-Acobe model with wave attenuation data in application with combined wave/current experiments

Data Source	Number of Data Points	α_n	β_n
Mathisen and Madsen (1996)	9	19.02 $\pm$6.71	160.77 $\pm$35.16

Table 4.7: Mean and standard deviation values for α_n and β_n using the two-layer Madsen-Salles model with $\gamma = 1$ and current profile data in application with combined wave/current experiments

Data Source	Number of Data Points	α_n	β_n
Mathisen and Madsen (1996)	7	19.48 $\pm$7.48	129.89 $\pm$49.87

Table 4.8: Mean and standard deviation values for α_n and β_n using the three-layer Barreto-Acobe model and current profile data in application with combined wave/current experiments

Data Source	Number of Data Points	α_n	β_n
Mathisen and Madsen (1996)	7	27.77 $\pm$8.29	185.11 $\pm$55.24

4.2.4 Spectral Wave-Current Experiments

Mathisen and Madsen (1996) also performed combined spectral wave/current experiments. Again, there are two roughness length scales to consider since both wave attenuation data and current profile data are available, namely waves in the presence of currents, k_{wc}, and currents in the presence of waves, k_{cw}. Only the wave attenuation data provided by Mathisen and Madsen (1996) were used in order to obtain the α_n and β_n values reported in Tables 4.9 and 4.10. Tables 4.11 and 4.12 show α_n and β_n values when only the current profile measurements were used with the two-layer Madsen-Salles model (with $\gamma = 1$) and the three-layer Barreto-Acobe flow model.

Table 4.9: Mean and standard deviation values for α_n and β_n using the two-layer Madsen-Salles model with wave attenuation data in application with combined spectral wave/current experiments

Data Source	Number of Data Points	α_n	β_n
Mathisen and Madsen (1996)	2	14.17 $\pm$2.12	94.49 $\pm$14.14

Table 4.10: Mean and standard deviation values for α_n and β_n using the three-layer Barreto-Acobe model with wave attenuation data in application with combined spectral wave/current experiments

Data Source	Number of Data Points	α_n	β_n
Mathisen and Madsen (1996)	2	16.43 $\pm$0.32	109.50 $\pm$2.12

Table 4.11: Mean and standard deviation values for α_n and β_n using the two-layer Madsen-Salles model with $\gamma = 1$ and current profile data in application with combined spectral wave/current experiments

Data Source	Number of Data Points	α_n	β_n
Mathisen and Madsen (1996)	2	14.17 $\pm$2.12	94.49 $\pm$14.14

Table 4.12: Mean and standard deviation values for α_n and β_n using the three-layer Barreto-Acobe model and current profile data in application with combined spectral wave/current experiments

Data Source	Number of Data Points	α_n	β_n
Mathisen and Madsen (1996)	2	19.46 $\pm$3.66	129.71 $\pm$24.72

4.2.5 Estimates for α_n and β_n Using Fixed Bed Data

Based on the fixed bed laboratory data presented in this section, empirical relationships were developed using the two-layer Madsen-Salles and three-layer Barreto-Acobe flow models.

Using wave attenuation data and the two-layer Madsen-Salles model,

$$k_n = (10 \pm 6)\,\eta \tag{4.7}$$

and

$$k_n = (65 \pm 47)\,\eta\frac{\eta}{\lambda} \tag{4.8}$$

Using current measurements and the two-layer Madsen-Salles model with $\gamma = 1$,

$$k_n = (17 \pm 7)\,\eta \tag{4.9}$$

and

$$k_n = (115 \pm 44)\,\eta\frac{\eta}{\lambda} \tag{4.10}$$

Using wave attenuation data and the three-layer Barreto-Acobe model,

$$k_n = (12 \pm 7)\,\eta \tag{4.11}$$

and

$$k_n = (77 \pm 52)\,\eta\frac{\eta}{\lambda} \tag{4.12}$$

Using current measurements and the three-layer Barreto-Acobe model,

$$k_n = (25 \pm 8)\,\eta \tag{4.13}$$

and

$$k_n = (167 \pm 51)\,\eta\frac{\eta}{\lambda} \tag{4.14}$$

The average and standard deviation values for α_n and β_n were calculated by equally weighting the number of data points used.

4.3 Movable Bed Data

4.3.1 Monochromatic Pure Wave Experiments

Carstens et al. (1969) measured the energy dissipation over a movable bed by monitoring the air pressure and the water level in the risers above their water tunnel. All of the tests were conducted at approximately the same period with varying orbital amplitude. Lofquist (1986) measured the energy dissipation in a wave tunnel with the use of pressure taps at either end. Rosengaus (1987) and Mathisen (1989) performed experiments in a wave flume and the energy dissipation was measured by recording the change in wave height along the flume. Tables 4.13 and 4.14 show the mean and standard deviation values for α_n and β_n using the preferred flow models in application with monochromatic pure wave experiments.

Table 4.13: Mean and standard deviation values for α_n and β_n using the two-layer Madsen-Salles model in application with monochromatic pure wave experiments

Data Source	Number of Data Points	α_n	β_n
Carstens et al. (1969)	35	14.81 ±6.45	120.94 ±161.61
Lofquist (1986)	82	12.30 ±5.61	72.41 ±33.24
Rosengaus (1987)	18	7.03 ±2.53	42.65 ±14.52
Mathisen (1989)	18	3.45 ±1.80	24.12 ±10.85
Rosengaus (1987) and Mathisen (1989)	26	8.09 ±3.61	50.45 ±21.58

4.3.2 Field Data

The field data used in this thesis were obtained at the LEO-15 site off the coast of southern New Jersey and used by Styles and Glenn (2002). Four current meters were deployed at 45, 80, 165, and 250 cm above the bottom. Horizontal resultant velocities and angles were calculated for each location and a best fit law-of-the-wall logarithmic velocity profile was used in order to determine the current velocity at a reference elevation, z_{ref}, a current specification similar to the one used in Section 3.5.3.

Determination of Current Shear Velocity and Apparent Roughness

Indirect estimates of the current shear velocity and apparent hydraulic roughness were obtained by fitting logarithmic profiles to the BASS current measurements. The current velocity equation, based on the classic law-of-the-wall for combined wave-current flow is

$$V_c = \frac{u_{*c}}{\kappa} \ln\left(\frac{z}{z_{0a}}\right) \tag{4.15}$$

Table 4.14: Mean and standard deviation values for α_n and β_n using the three-layer Barreto-Acobe model in application with monochromatic pure wave experiments

Data Source	Number of Data Points	α_n	β_n
Carstens et al. (1969)	35	18.18 $\pm$8.35	149.64 $\pm$206.32
Lofquist (1986)	82	14.34 $\pm$5.22	86.05 $\pm$38.32
Rosengaus (1987)	18	8.56 $\pm$3.57	51.91 $\pm$21.22
Mathisen (1989)	18	4.50 $\pm$2.46	31.40 $\pm$14.84
Rosengaus (1987) and Mathisen (1989)	26	10.00 $\pm$4.17	62.45 $\pm$25.21

where V_c is the current velocity and z_{0a} is the apparent hydraulic roughness.
A horizontal resultant velocity and resultant angle was calculated for each current meter location. Shear velocities and apparent roughness values were calculated for those bursts that satisfied the following criteria:

1. Current meter measurements indicated a current greater than 5 cm/sec at the 80 cm level and

2. The maximum veering angle, i.e. the difference in direction, between the current sensors is less than 10 degrees.

Regression analysis was applied using the law-of-the-wall fit in (4.15) to the data points that satisfied the above criteria and those bursts with R^2 values greater than 0.95 were considered for further analysis. The results of these calculations produced 47 bursts in total and are tabulated and reported in Appendix E.

Application of Preferred Models

For each data burst, the two preferred wave-current interaction models were run in order to produce an estimate of the bottom roughness length scale, k_n. Because γ is a fitting parameter of the Madsen-Salles model and not known a priori, each run was repeated with the following range: $\gamma = 1/3, 1/2$, and 1. Mean and standard deviation values for α_n and β_n using the preferred flow models in application with field data are shown in Tables 4.15, 4.16, 4.17, and 4.18.

Table 4.15: Mean and standard deviation values for α_n and β_n using the two-layer Madsen-Salles model with $\gamma = 1/3$ in application with combined flow field data

Data Source	Number of Data Points	α_n	β_n
Styles and Glenn (2002)	47	9.11 $\pm$9.74	54.77 $\pm$64.40

Table 4.16: Mean and standard deviation values for α_n and β_n using the two-layer Madsen-Salles model with $\gamma = 1/2$ in application with combined flow field data

Data Source	Number of Data Points	α_n	β_n
Styles and Glenn (2002)	47	5.34 $\pm$5.37	32.05 $\pm$35.70

Table 4.17: Mean and standard deviation values for α_n and β_n using the two-layer Madsen-Salles model with $\gamma = 1$ in application with combined flow field data

Data Source	Number of Data Points	α_n	β_n
Styles and Glenn (2002)	47	2.41 $\pm$2.19	14.44 $\pm$14.71

Table 4.18: Mean and standard deviation values for α_n and β_n using the three-layer Barreto-Acobe model in application with combined flow field data

Data Source	Number of Data Points	α_n	β_n
Styles and Glenn (2002)	47	5.25 $\pm$3.43	30.99 $\pm$23.54

4.3.3 Estimates for α_n and β_n Using Movable Bed Data

Based on the movable bed laboratory and field data presented in this section, empirical relationships were developed using the two-layer Madsen-Salles and three-layer Barreto-Acobe flow models.

Using wave attenuation data and the two-layer Madsen-Salles model,

$$k_n = (11 \pm 6)\,\eta \tag{4.16}$$

and

$$k_n = (71 \pm 79)\,\eta\frac{\eta}{\lambda} \tag{4.17}$$

Using current measurements and the two-layer Madsen-Salles model with $\gamma = 1$,

$$k_n = (2.5 \pm 2)\,\eta \tag{4.18}$$

and

$$k_n = (14 \pm 15)\,\eta\frac{\eta}{\lambda} \tag{4.19}$$

Using wave attenuation data and the three-layer Barreto-Acobe model, the following

values were obtained:

$$k_n = (13 \pm 7)\,\eta \tag{4.20}$$

and

$$k_n = (86 \pm 101)\,\eta\frac{\eta}{\lambda} \tag{4.21}$$

Using current measurements and the three-layer Barreto-Acobe model,

$$k_n = (5 \pm 3)\,\eta \tag{4.22}$$

and

$$k_n = (31 \pm 24)\,\eta\frac{\eta}{\lambda} \tag{4.23}$$

The average and standard deviation values for α_n and β_n were calculated by equally weighting the number of data points used.

4.4 Summary and Conclusions

Two ripple geometry and equivalent bed roughness models were developed in this chapter, of the forms presented in equations (4.1) and (4.2). Values for α_n and β_n were calculated using fixed and movable laboratory and field data. For the Mathisen and Madsen (1996) fixed bed laboratory data set, both wave attenuation and current profile data are available. Therefore, wave attenuation measurements were used in

order to calculate the bottom roughness for the cases of pure waves and waves in the presence of a current while current measurements were used in order to establish the bottom roughness for the case of currents in the presence of waves. For the two-layer Madsen-Salles model with $\gamma = 1$, the ripple geometry and equivalent bed roughness models are statistically consistent for both movable and fixed laboratory data, regardless of whether wave attenuation data or current profile data were used in order to calculate the bottom roughness length scale, as seen in (4.7), (4.8), (4.9), (4.10), (4.16), and (4.17). However, for the three-layer Barreto-Acobe flow model, the ripple geometry and equivalent bed roughness models using laboratory wave attenuation and current profile data are statistically different, as seen in (4.11), (4.12), (4.13), (4.14), (4.20), and (4.21).

All the models presented in this thesis assume that the bottom roughness may be described by a single roughness length scale, k_n. However, differences between roughness values for waves and currents can arise from bedform geometry and/or near-bottom flow characteristics. The experimental results of Mathisen and Madsen (1996) were used to check the single roughness assumption. While the three-layer Barreto-Acobe model yields smaller standard deviation values for the roughness, the two-layer Madsen-Salles model appears to be more robust in that one length scale, k_n, may be justifiably used for the cases of pure waves, waves in the presence of a current, and currents in the presence of waves. When using the three-layer Barreto-Acobe model with combined wave-current flow, one must use a roughness value that is application-specific, i.e. a different roughness value must be used depending on whether wave attenuation or current profile predictions are desired. In cases where current profiles are to be predicted, the roughness model that must be used with the three-layer Barreto-Acobe model is significantly larger when compared to the roughness model that must be be applied when wave attenuation is to be predicted.

Even though two ripple geometry and equivalent bed roughness models were presented in this chapter, the model of the form (4.1) involving the empirical constant

α_n generally has smaller standard deviation values and therefore provides a better fit than the model involving β_n presented in (4.2), as seen in Tables 4.1 - 4.18. Therefore, the recommended conceptual model for practical applications involving movable bed data is of the form $k_n = \alpha_n \eta$.

The ripple geometry and roughness model that is statistically consistent with both the two-layer Madsen-Salles and the three-layer Barreto-Acobe flow models for the prediction of wave associated bottom shear stress using both movable and fixed bed wave attenuation data from the laboratory is:

$$k_n = (11 \pm 6)\eta \tag{4.24}$$

The average and standard deviation values for α_n were calculated by equally weighting all laboratory data (movable and fixed bed) for the two-layer Madsen-Salles model and the three-layer Barreto-Acobe model.

Since the field is the natural environment for the application of the flow models presented in this thesis, the following ripple geometry and equivalent bed roughness model is statistically consistent with the field data presented in this chapter and is recommended for practical applications:

$$k_n = (2.5 \pm 2)\eta \tag{4.25}$$

Notice that (4.25) is considerably smaller than the three-layer Barreto-Acobe field data results (4.22). This discrepancy is in accordance with the observation that a single roughness scale is not applicable when using the three-layer Barreto-Acobe flow model. Just as the results of the three-layer Barreto-Acobe model are larger when using current measurements when compared to wave attenuation measurements in the laboratory, the same argument can be applied with field data. Since all of the laboratory wave attenuation measurements are statistically consistent, regardless of which

flow model was used, and since one roughness length scale can be justifiably used for the two-layer Madsen-Salles model, one could reasonably expect that the Madsen-Salles field data results would be consistent with wave attenuation data (supposing that wave attenuation could be available for field data applications). Therefore, the significantly larger roughness values obtained with the three-layer Barreto-Acobe model from field data (4.22) are to be expected as a consequence of the roughness scale for currents in the presence of waves being larger than that for waves in the presence of currents.

It is not known at this time why the model recommended for field applications in (4.25) is much different from the model (4.24) that is consistent with the all of the laboratory data presented in this chapter. Since laboratory experiments usually involve superior accuracy of measurements, one may attribute the differences to scale effects since laboratory data also involve shorter wave periods. In addition, fixed bed laboratory data also involve sharper roughnesses and therefore the associated drag forces are different than drag forces typically encountered in the field. However, since the results of both fixed and movable bed laboratory data presented in this text are statistically consistent, this effect can be considered negligible in the present context.

Chapter 5

Ripple Model and Application of the Preferred Flow Models

In the present chapter, a model for wave-generated ripples is developed based on available movable bed laboratory and field data. The two-layer Madsen-Salles flow model and the three-layer Barreto-Acobe flow model are then applied in conjunction with the ripple geometry and roughness models for the cases of known and unknown ripple geometry. Pure wave movable bed data from Carstens et al. (1969), Lofquist (1986), Rosengaus (1987), and Mathisen (1989) and combined wave-current data collected by Mathisen and Madsen (1996) and Styles and Glenn (2002) are used in order to assess the predictive capabilities of the preferred flow models. Predicted and observed values for f_w and u_{*c} are graphically depicted using the ripple geometry and roughness relationships developed for the flow models.

5.1 Model of Wave-Generated Ripples

In the absence of direct measurements, ripple height estimates are often needed for applications of wave-current interaction flow models.

Wikramanayake and Madsen (1991) found that the ratio of the mobility number,

defined as

$$\theta_m = \frac{(A_b\omega)^2}{(s-1)\,gd} \tag{5.1}$$

to the nondimensional sediment parameter, defined as

$$S_* = \frac{d}{4\nu}\left[(s-1)\,gd\right]^{1/2} \tag{5.2}$$

was well correlated with ripple data where A_b is the bottom excursion amplitude, ω is the wave frequency, d is the sediment diameter, ν is the kinematic viscosity of water, s is the ratio of the sediment density to the fluid density, and g is the acceleration due to gravity.

An empirical ripple model was calibrated by plotting the relative ripple height, η/A_b and the relative ripple length, λ/A_b as a function of this ratio using the laboratory and field data presented in Chapter 4 in addition to the data of Boyd et al. (1988), Dingler (1974), Inman (1957), Inman and Bowen (1963), Kennedy and Falcon (1965), Lambie (1984), Lofquist (1978), Miller and Komar (1980), Mogridge and Kamphuis (1972), Nielsen (1979, 1984) and Sato (1988). All of the data used in this text are tabulated and presented in Appendix A through Appendix E. The following model was produced:

$$\frac{\eta}{A_b} = \begin{cases} 0.24X^{-0.24} & \text{for } X \leq 3 \\ 0.25X^{-0.3} & \text{for } X \geq 3 \end{cases} \tag{5.3}$$

and

$$\frac{\lambda}{A_b} = \begin{cases} 1.42X^{-0.24} & \text{for } X \leq 3 \\ 1.52X^{-0.24} & \text{for } X \geq 3 \end{cases} \tag{5.4}$$

where X, the nondimensional wave and sediment parameter, is defined by

$$X = \frac{\theta_m}{S_*} = \frac{4\nu \left(A_b \omega\right)^2}{d\left[\left(s-1\right) g d\right]^{1.5}} \tag{5.5}$$

The results of the calibration are given in Figure 5-1 and Figure 5-2.

A measure of the model's performance can be seen in the average and standard deviation values of the variables ϵ_1 and ϵ_2, where

$$\epsilon_1 = \frac{(\eta/A_b)_{\text{observed}}}{(\eta/A_b)_{\text{predicted}}} \tag{5.6}$$

and

$$\epsilon_2 = \frac{(\lambda/A_b)_{\text{observed}}}{(\lambda/A_b)_{\text{predicted}}} \tag{5.7}$$

For $X \leq 3$, the average and standard deviation values of ϵ_1 from (5.6) are 1.00 and 0.29, respectively. For $X \geq 3$, the average and standard deviation values of ϵ_1 from (5.6) are 1.00 and 0.72, respectively. For $X \leq 3$, the average and standard deviation values of ϵ_2 from (5.7) are 1.00 and 0.27, respectively. For $X \geq 3$, the average and standard deviation values of ϵ_1 from (5.7) are 1.00 and 0.50, respectively. At the present time it is unknown why some data sets do not behave as "expected" and hence contribute to large values of standard deviation for ϵ_1 and ϵ_2 for $X \geq 3$. Therefore, further investigation is needed.

Notice that for $X \geq 3$, η decays at a faster rate than for $X \leq 3$. This is physically plausible since ripple steepness is likely to decrease with increasing flow intensity and an intense storm may even cause ripples to washout. The models presented in (5.3) and (5.4) are not perfectly continuous at $X = 3$, however, the discontinuity may be considered insignificant for the present applications.

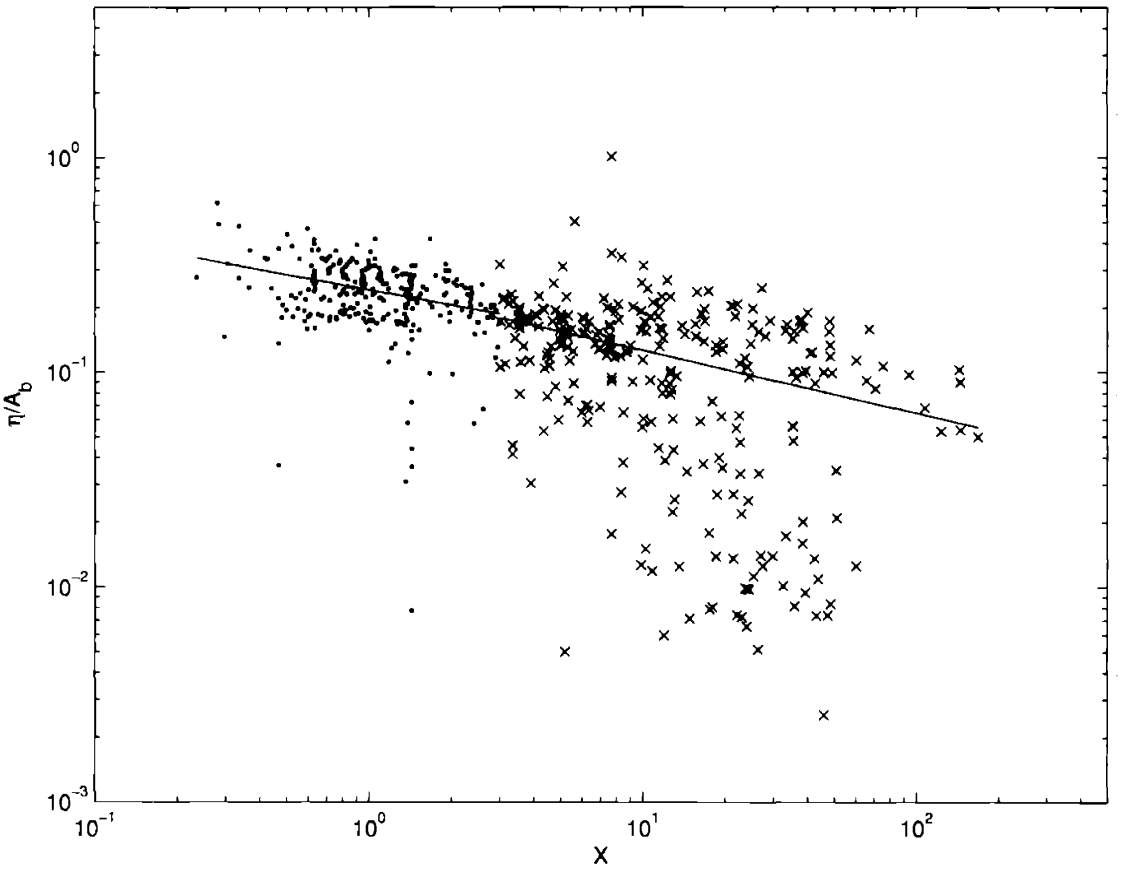

Figure 5-1: Relative ripple height as a function of the nondimensional wave and sediment parameter, X. The solid line denotes the best fit curve, presented in (5.3). For $X < 3$, the average and standard deviation values of ϵ_1 from (5.6) are 1.00 and 0.29, respectively. For $X > 3$, the average and standard deviation values of ϵ_1 from (5.6) are 1.00 and 0.72, respectively.

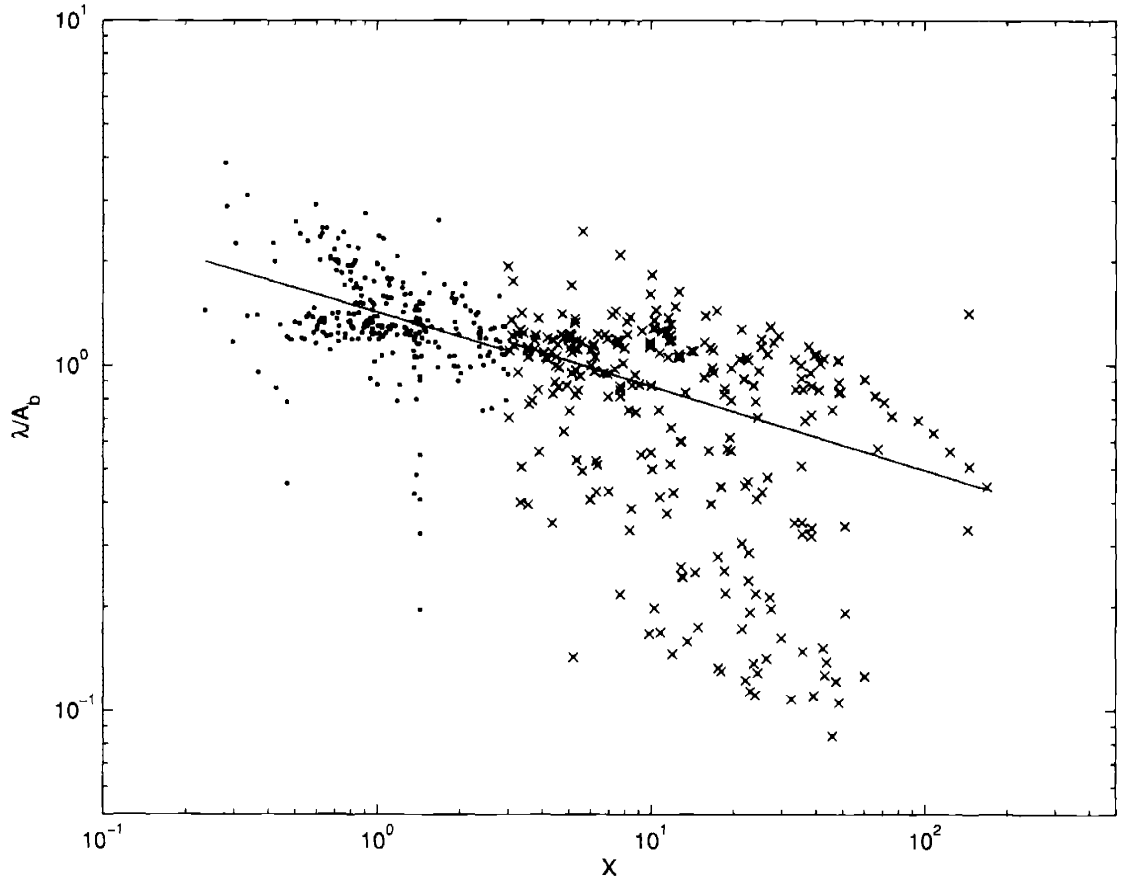

Figure 5-2: Relative ripple length as a function of the nondimensional wave and sediment parameter, X. The solid line denotes the best fit curve, presented in (5.4). For $X < 3$, the average and standard deviation values of ϵ_2 from (5.7) are 1.00 and 0.27, respectively. For $X > 3$, the average and standard deviation values of ϵ_2 from (5.7) are 1.00 and 0.50, respectively.

5.2 Evaluation of the Combined Ripple Geometry and Roughness Models

The predictive capabilities of the preferred flow models were assessed using pure wave data collected by Carstens et al. (1969), Lofquist (1986), Rosengaus (1987), and Mathisen (1989), fixed bed laboratory data collected by Mathisen and Madsen (1996), and field data used by Styles and Glenn (2002). Based on the ripple geometry and roughness model presented in Chapter 4, $k_n = 11\eta$ was used in conjunction with the preferred flow models for the cases where the ripple geometry is assumed known prior to the application of the flow models. $k_n = 11\eta$ is statistically consistent with the laboratory data presented in Chapter 4 and was applied with both the two-layer Madsen-Salles model and the three-layer Barreto-Acobe model.

For the movable bed, pure wave data, a measure of each model's performance can be seen in the average and standard deviation values of the variable ψ, where

$$\psi = \frac{f_{w,\ \text{observed}}}{f_{w,\ \text{predicted}}} \tag{5.8}$$

For the combined wave-current flow data, a measure of each model's performance can be seen in the average and standard deviation values of the variable ϕ, where

$$\phi = \frac{u_{*c,\ \text{observed}}}{u_{*c,\ \text{predicted}}} \tag{5.9}$$

5.2.1 Movable Bed Laboratory Data

Predicted and observed f_w values were obtained from the movable bed laboratory data of Carstens et al. (1969), Lofquist (1986), Rosengaus (1987), and Mathisen

(1989) in the presence and absence of known ripple geometry.

Ripple Geometry Known

Assuming the ripple geometry is known, the two-layer Madsen-Salles and three-layer Barreto-Acobe flow models can be applied using $k_n = 11\eta$ from (4.24) where η is a measured or observed value. The two-layer Madsen-Salles model slightly underpredicts the friction factor as shown in Figure 5-3 and the average and standard deviation values of ψ from (5.8) are 1.06 and 0.30, respectively. The two-layer model appears to underpredict f_w considerably for large roughnesses. Similarly, as shown in Figure 5-4, the three-layer Barreto-Acobe model also underpredicts the friction factor, especially for large roughnesses. The average and standard deviation values of ψ from (5.8) are 1.19 and 0.32, respectively. However, due to the presence of a wide variety of movable laboratory and field data, one would be hard-pressed to find a more suitable roughness relationship in the form of $k_n = \alpha_n \eta$ where α_n is a known and generally valid constant.

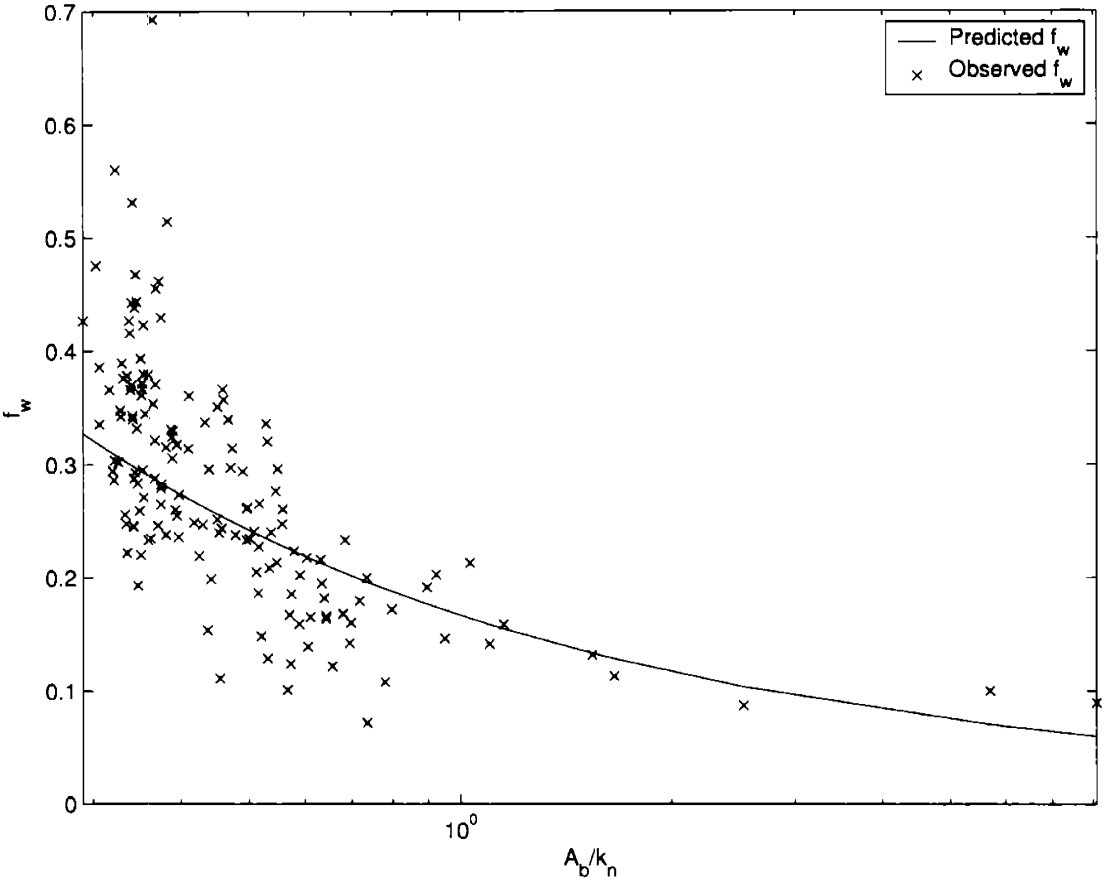

Figure 5-3: Comparison of observed and predicted f_w using the two-layer Madsen-Salles model and $k_n = 11\eta$ with measured values of η and movable bed laboratory data. The average and standard deviation values of ψ from (5.8) are 1.06 and 0.30, respectively.

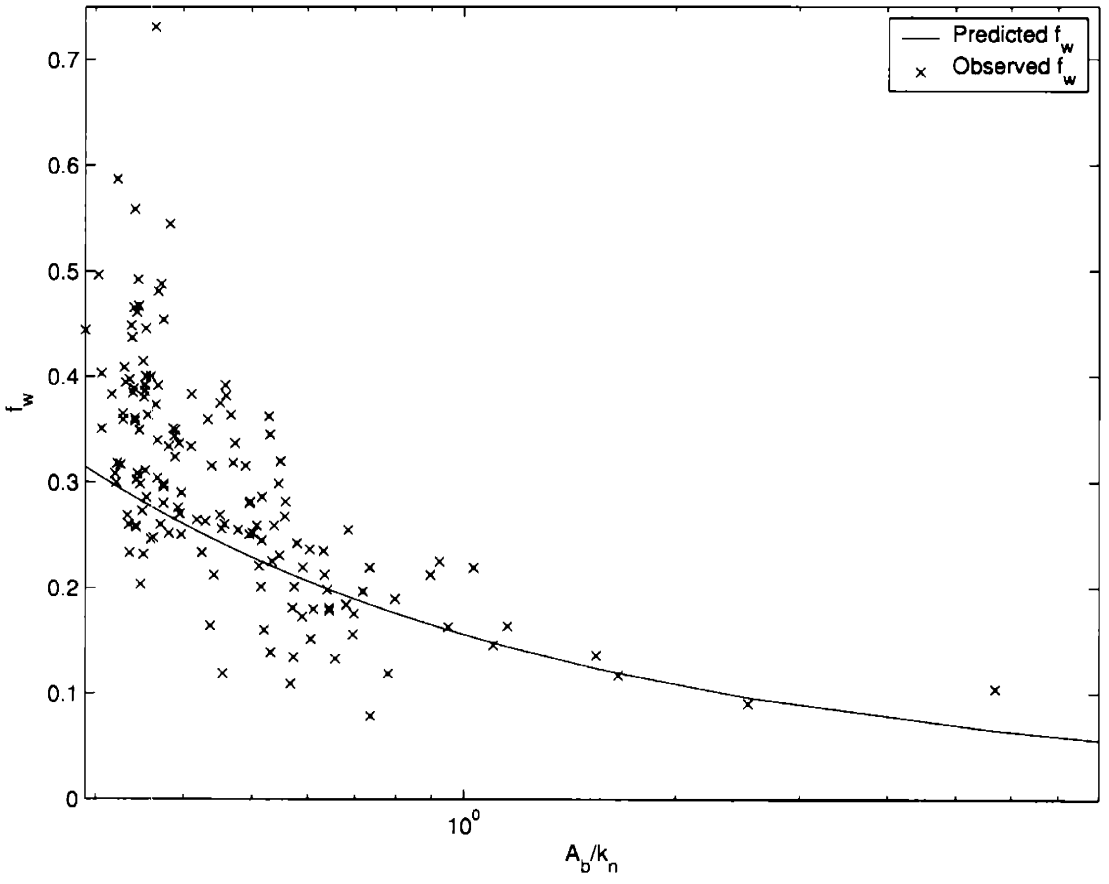

Figure 5-4: Comparison of observed and predicted f_w using the three-layer Barreto-Acobe model and $k_n = 11\eta$ with measured values of η and movable bed laboratory data. The average and standard deviation values of ψ from (5.8) are 1.19 and 0.32, respectively.

Ripple Geometry Unknown

For the practical case where ripple geometry is not known or measured directly, the model developed for wave-generated ripples in Section 5.1 can be applied in conjunction with the ripple geometry and roughness model presented in Chapter 4, namely $k_n = 11\eta$ where η is computed from (5.3). 152 experiments were used in total; 88 experiments with $X < 3$ and 64 experiments with $X > 3$. For $X < 3$, where X is given in (5.5), the two-layer Madsen-Salles model underpredicts the friction factor as shown in Figure 5-5 and the average and standard deviation values of ψ from (5.8) are 1.21 and 0.26, respectively. For $X > 3$, given in (5.5), the two-layer Madsen-Salles model overpredicts the friction factor as shown in Figure 5-5 and the average and standard deviation values of ψ from (5.8) are 0.91 and 0.25, respectively. Again, the two-layer model underpredicts f_w considerably for large roughnesses. As shown in Figure 5-6, the three-layer Barreto-Acobe model underpredicts the friction factor for all values of X, where X is given in (5.3). For $X < 3$ and using the three-layer Barreto-Acobe flow model, the average and standard deviation values of ψ from (5.8) are 1.35 and 0.29, respectively. For $X > 3$, the average and standard deviation values of ψ from (5.8) are 1.06 and 0.28, respectively. Again, as is the case with the two-layer model, the three-layer model also underpredicts f_w considerably for large roughnesses. For the case of unknown ripple geometry, two ripple geometry and roughness models are applied in conjunction with a flow model. Considering that the results presented in Figures 5-5 and 5-6 involve the application of three models in total, each model with its own variability, the performance of the two-layer Madsen-Salles and three-layer Barreto-Acobe flow models are well within reason.

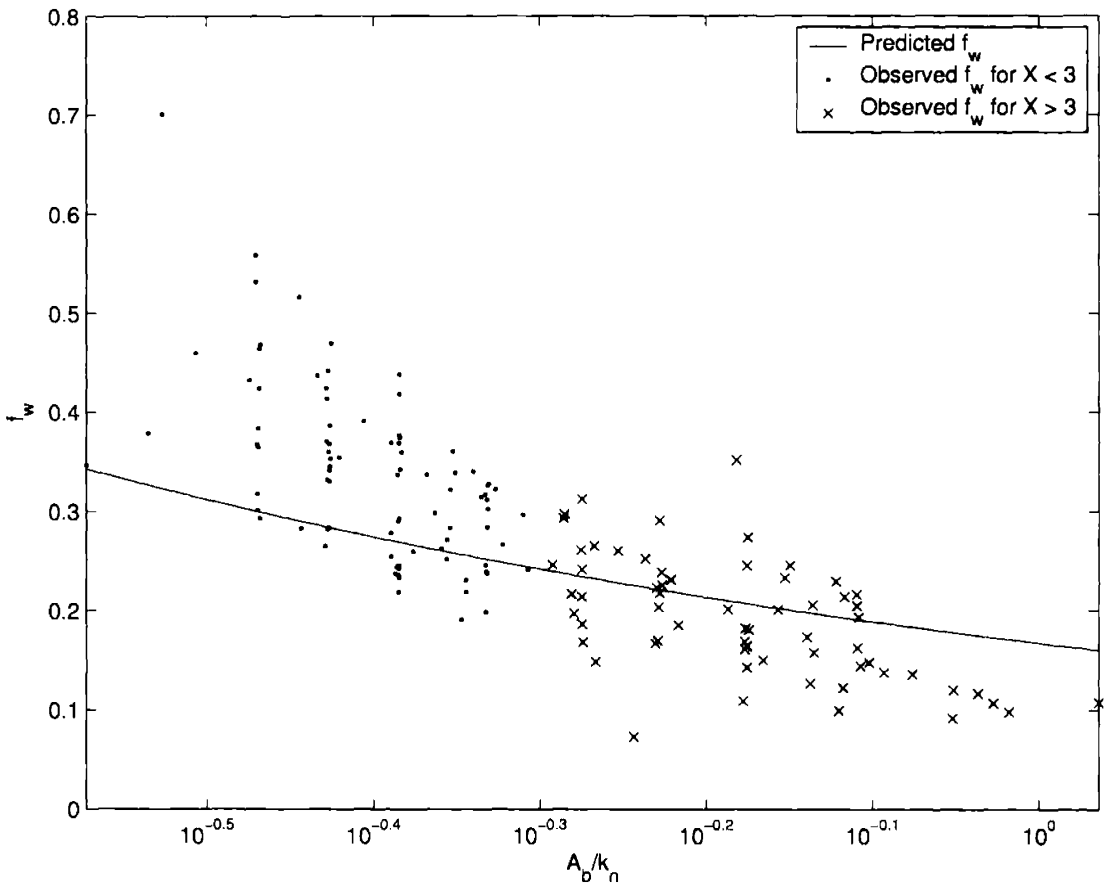

Figure 5-5: Comparison of observed and predicted f_w using the two-layer Madsen-Salles model and $k_n = 11\eta$ where η is determined from (5.3). For $X < 3$, the average and standard deviation values of ψ from (5.8) are 1.21 and 0.26, respectively. For $X > 3$, the average and standard deviation values of ψ from (5.8) are 0.91 and 0.25, respectively.

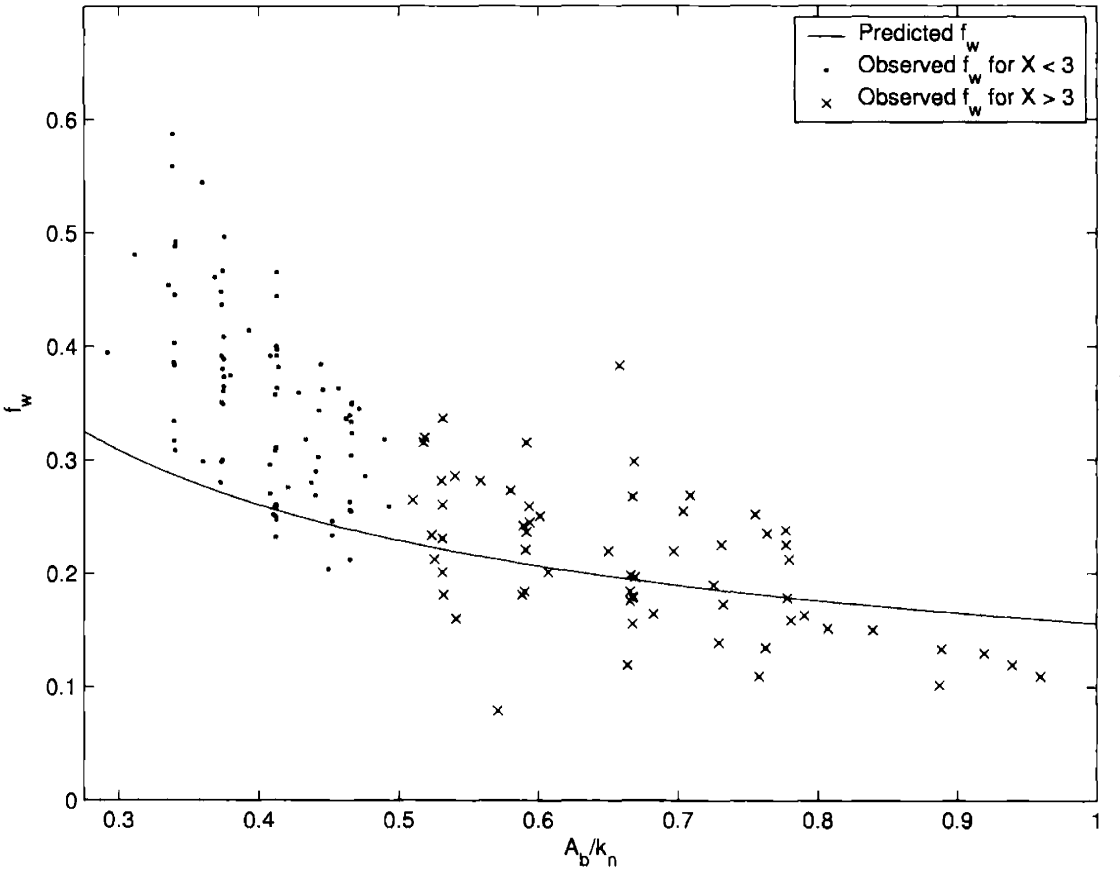

Figure 5-6: Comparison of observed and predicted f_w using the three-layer Barreto-Acobe model and $k_n = 11\eta$ where η is determined from (5.3). For $X < 3$, the average and standard deviation values of ψ from (5.8) are 1.35 and 0.29, respectively. For $X > 3$, the average and standard deviation values of ψ from (5.8) are 1.06 and 0.28, respectively.

5.2.2 Combined Flow Laboratory Data of Mathisen and Madsen (1996)

Predicted and observed u_{*c} values were obtained from the preferred flow models and logarithmic profile fits to current meter data collected by Mathisen and Madsen (1996) for artificial roughness elements. The results of the combined ripple geometry and roughness model are shown in Figures 5-7, 5-8, 5-9, and 5-10. In Figure 5-7, the two-layer Madsen-Salles model with $\gamma = 1$ was used with $k_n = 11\eta$. The model clearly underpredicts u_{*c} as a result of k_n being too small and the average and standard deviation values of ϕ from (5.9) are 1.09 and 0.08, respectively. Based on Table 4.5, the average α_n-value for this particular data set is 17. Therefore, as evident in Figure 5-8, the fit is greatly improved when $k_n = 17\eta$ is used in conjunction with the two-layer Madsen-Salles model. For the improved fit, the average and standard deviation values of ϕ from (5.9) are 1.00 and 0.08, respectively. Even though the average value of ϕ improved when using $k_n = 17\eta$, the standard deviation remained identical to the value obtained when $k_n = 11\eta$ was applied with the two-layer Madsen-Salles model.

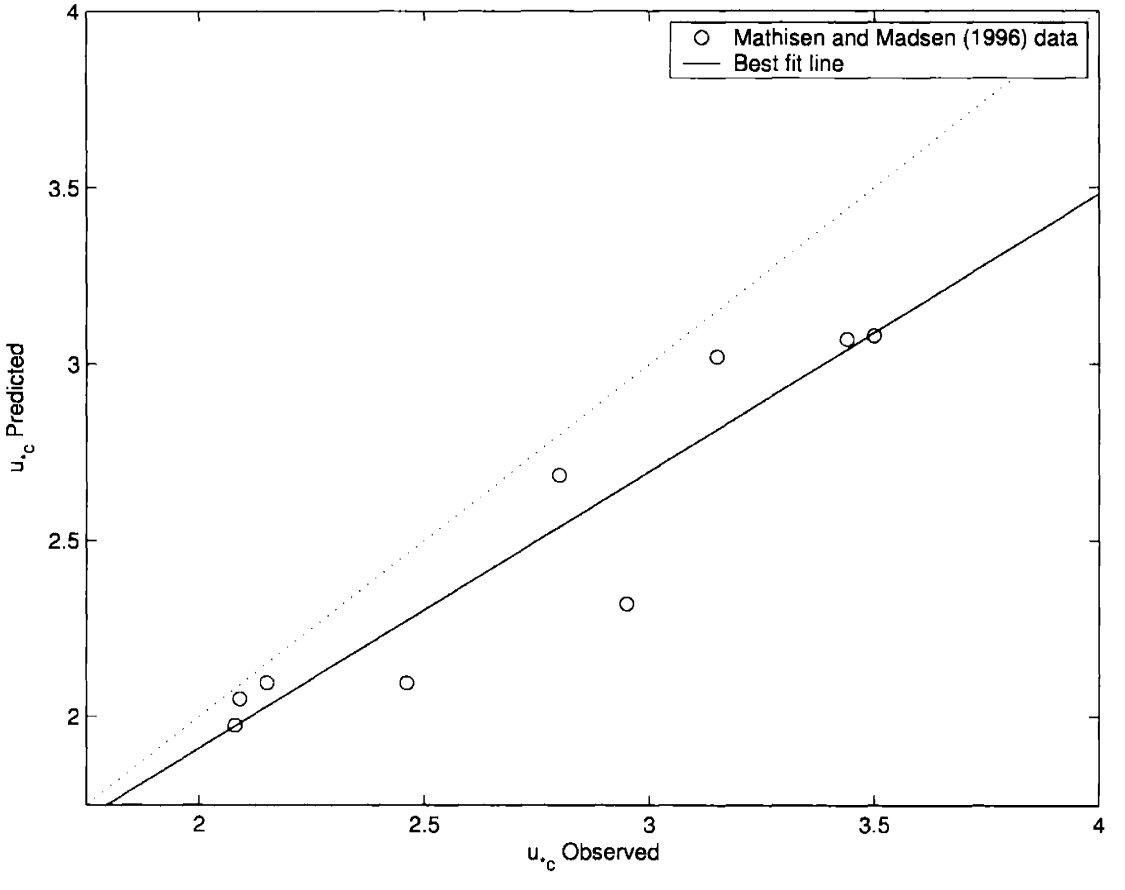

Figure 5-7: Comparison of observed and predicted u_{*c} using the two-layer Madsen-Salles model with $\gamma = 1$ and $k_n = 11\eta$ with laboratory data used by Mathisen and Madsen (1996). The average and standard deviation values of ϕ from (5.9) are 1.09 and 0.08, respectively.

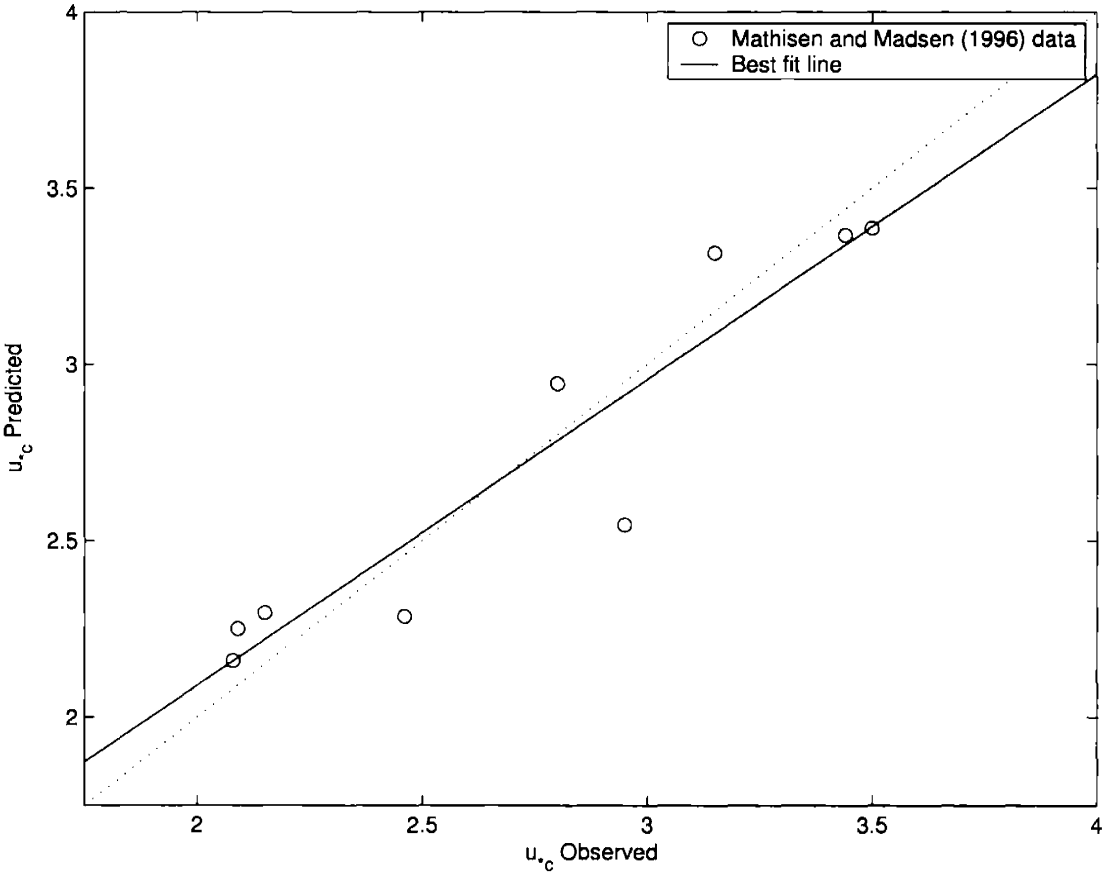

Figure 5-8: Comparison of observed and predicted u_{*c} using the two-layer Madsen-Salles model with $\gamma = 1$ and $k_n = 17\eta$ with laboratory data used by Mathisen and Madsen (1996). The average and standard deviation values of ϕ from (5.9) are 1.00 and 0.08, respectively.

In Figure 5-9, the three-layer Barreto-Acobe model was used with $k_n = 11\eta$. The model also clearly underpredicts u_{*c} as a result of k_n being too small and the average and standard deviation values of ϕ from (5.9) are 1.31 and 0.09, respectively. Based on Table 4.6, the average α_n-value for this particular data set is 19. Therefore, as evident in Figure 5-10, the fit is greatly improved when $k_n = 19\eta$ is used in conjunction with the three-layer Barreto-Acobe model.

Even after applying $k_n = 19\eta$, the three-layer Barreto-Acobe model still underpredicts u_{*c} and the average and standard deviation values of ϕ from (5.9) are 1.16 and 0.08, respectively. Recall that the values obtained in Table 4.6 were determined for the condition of waves in the presence of currents, i.e. wave attenuation data was used in order to determine the α and β values reported in Chapter 4. Since $k_{wc} < k_{cw}$ for the three-layer Barreto-Acobe model as discussed in Chapter 4, the model expectedly underpredicts u_{*c}. This feature is not apparent when using the two-layer Madsen-Salles model because a single roughness value, k_n can be used, i.e. $k_{wc} \approx k_{cw}$ as discussed in Chapter 4.

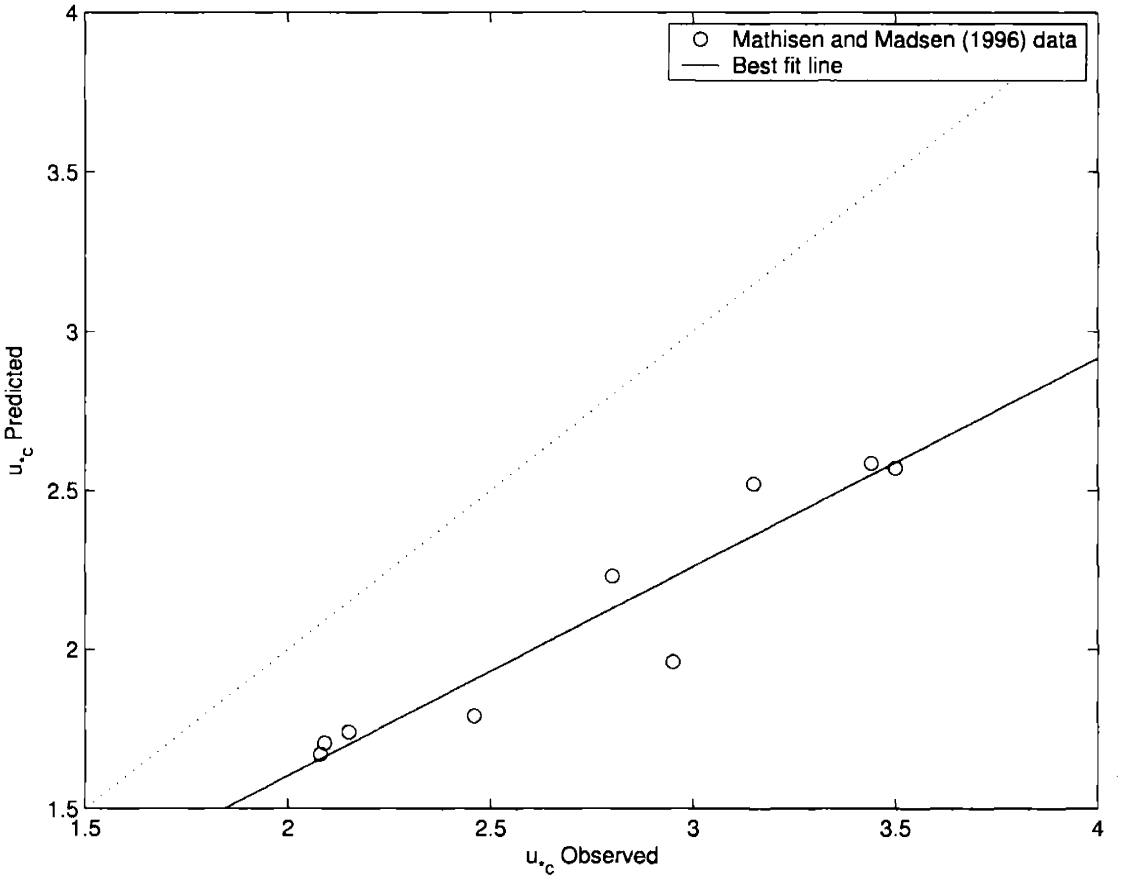

Figure 5-9: Comparison of observed and predicted u_{*c} using the three-layer Barreto-Acobe model and $k_n = 11\eta$ with laboratory data used by Mathisen and Madsen (1996). The average and standard deviation values of ϕ from (5.9) are 1.31 and 0.09, respectively.

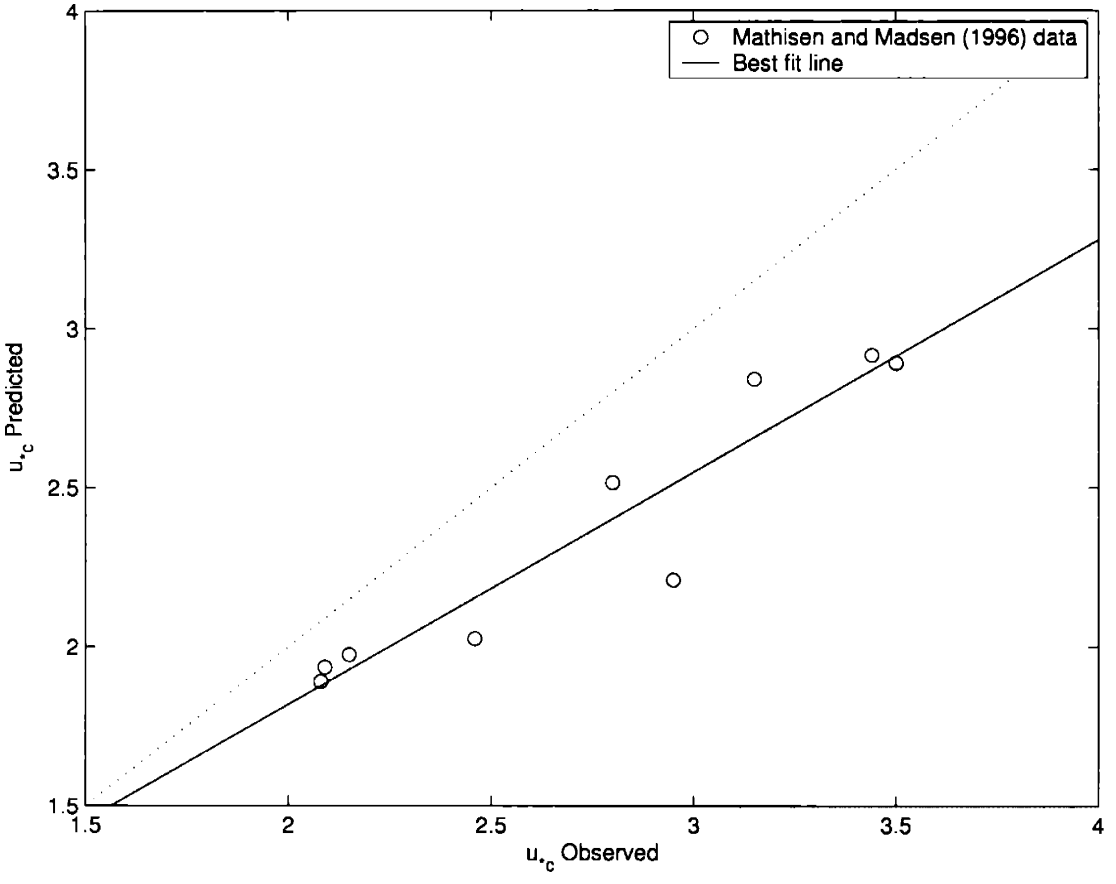

Figure 5-10: Comparison of observed and predicted u_{*c} using the three-layer Barreto-Acobe model and $k_n = 19\eta$ with laboratory data used by Mathisen and Madsen (1996). The average and standard deviation values of ϕ from (5.9) are 1.16 and 0.08, respectively.

5.2.3 Field Data of Styles and Glenn (2002)

Predicted and observed u_{*c} values were obtained from the field data of Styles and Glenn (2002) in the presence and absence of known ripple geometry.

Ripple Geometry Known

Assuming the ripple geometry is known, the two-layer Madsen-Salles and three-layer Barreto-Acobe flow models can be applied using $k_n = 2.5\eta$ from (4.25) where η is a measured or observed value. Predicted and observed u_{*c} values were obtained from the preferred flow models and logarithmic profile fits to current meter data used by Styles and Glenn (2002). The results of the combined ripple geometry and roughness model are shown in Figures 5-11, 5-12, and 5-13.

In Figure 5-11, the two-layer Madsen-Salles model with $\gamma = 1$ was used with $k_n = 2.5\eta$, the recommended ripple geometry and roughness model for application with field data (4.25). The model clearly predicts u_{*c} well since the ripple geometry and roughness model was developed with this data set (Table 4.17) and the average and standard deviation values of ϕ from (5.9) are 0.98 and 0.20, respectively.

In Figure 5-12, the three-layer Barreto-Acobe model was used with $k_n = 2.5\eta$. The model underpredicts u_{*c} as a result of k_n being too small and the average and standard deviation values of ϕ from (5.9) are 1.24 and 0.25, respectively. Based on the analysis presented in Chapter 4, a single roughness length scale cannot be applied universally when using the three-layer Barreto-Acobe flow model. One must use an increased value for k_n with current measurements, i.e. $k_n = 5\eta$ should be applied with field data and the three-layer Barreto-Acobe flow model (4.22). Therefore, as evident in Figure 5-13, the fit is greatly improved when $k_n = 5\eta$ is used in conjunction with the three-layer Barreto-Acobe model. For the improved fit, the average and standard deviation values of ϕ from (5.9) are 1.04 and 0.21, respectively.

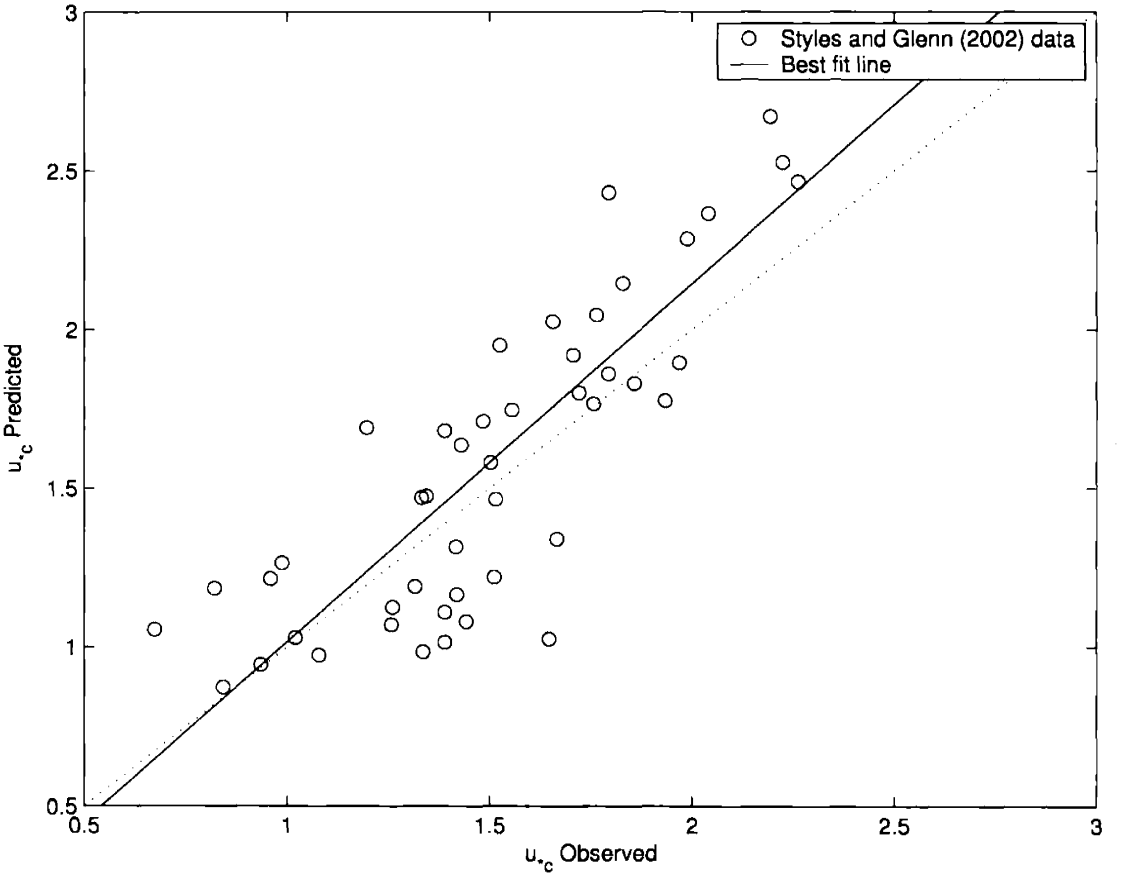

Figure 5-11: Comparison of observed and predicted u_{*c} using the two-layer Madsen-Salles model with $\gamma = 1$ and $k_n = 2.5\eta$ with field data used by Styles and Glenn (2002) and measured values of η. The average and standard deviation values of ϕ from (5.9) are 0.98 and 0.20, respectively.

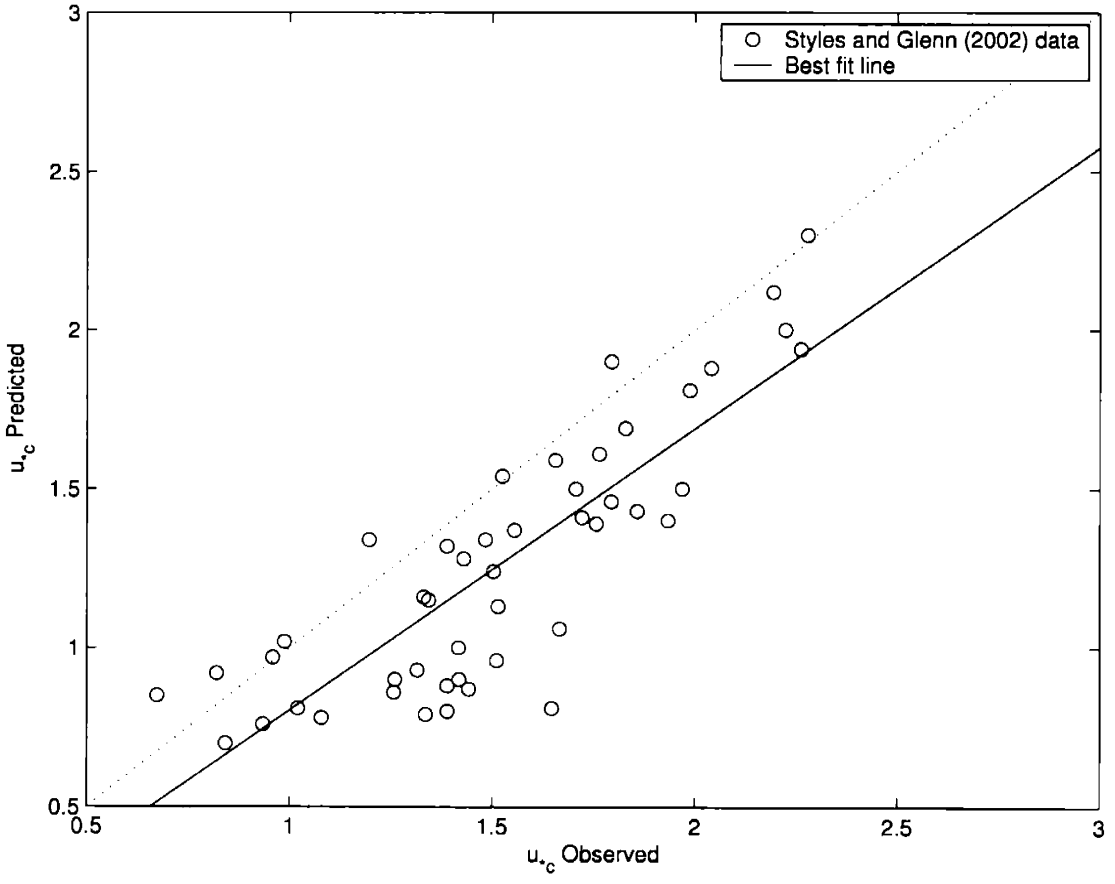

Figure 5-12: Comparison of observed and predicted u_{*c} using the three-layer Barreto-Acobe model and $k_n = 2.5\eta$ with field data used by Styles and Glenn (2002) and measured values of η. The average and standard deviation values of ϕ from (5.9) are 1.24 and 0.25, respectively.

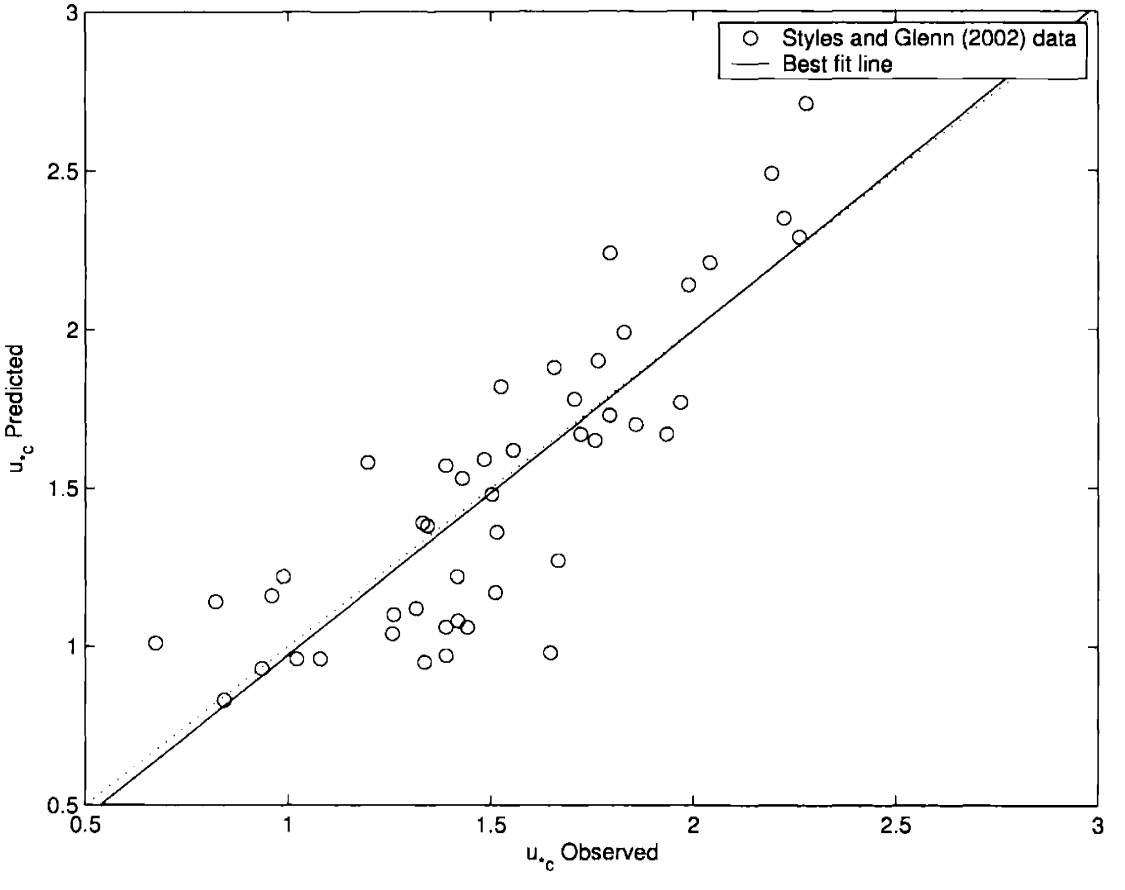

Figure 5-13: Comparison of observed and predicted u_{*c} using the three-layer Barreto-Acobe model and $k_n = 5\eta$ with field data used by Styles and Glenn (2002) and measured values of η. The average and standard deviation values of ϕ from (5.9) are 1.04 and 0.21, respectively.

Ripple Geometry Unknown

For the practical case where ripple geometry is not known or measured directly, the model developed for wave-generated ripples in Section 5.1 can be applied in conjunction with the ripple geometry and roughness model presented in Chapter 4, namely $k_n = 2.5\eta$ where η is computed from (5.3). Predicted and observed u_{*c} values were obtained from the preferred flow models and logarithmic profile fits to current meter data used by Styles and Glenn (2002). The results of the combined ripple geometry and roughness model are shown in Figures 5-14, 5-15, and 5-16.

In Figure 5-14, the two-layer Madsen-Salles model with $\gamma = 1$ was used with $k_n = 2.5\eta$, the recommended ripple geometry and roughness model for application with field data (4.25). 47 experiments were used in total; all 47 experiments with $X < 3$. The model clearly predicts u_{*c} well since the ripple geometry and roughness model was developed with this data set (Table 4.17) and the average and standard deviation values of ϕ from (5.9) are 1.03 and 0.17, respectively.

In Figure 5-15, the three-layer Barreto-Acobe model was used with $k_n = 2.5\eta$. The model underpredicts u_{*c} as a result of k_n being too small and the average and standard deviation values of ϕ from (5.9) are 1.29 and 0.21, respectively. Based on the analysis presented in Chapter 4, a single roughness length scale cannot be applied universally when using the three-layer Barreto-Acobe flow model. One must use an increased value for k_n with current measurements, i.e. $k_n = 5\eta$ should be applied with field data and the three-layer Barreto-Acobe flow model (4.22). Therefore, as evident in Figure 5-16, the fit is greatly improved when $k_n = 5\eta$ is used in conjunction with the three-layer Barreto-Acobe model. For the improved fit, the average and standard deviation values of ϕ from (5.9) are 1.09 and 0.16, respectively.

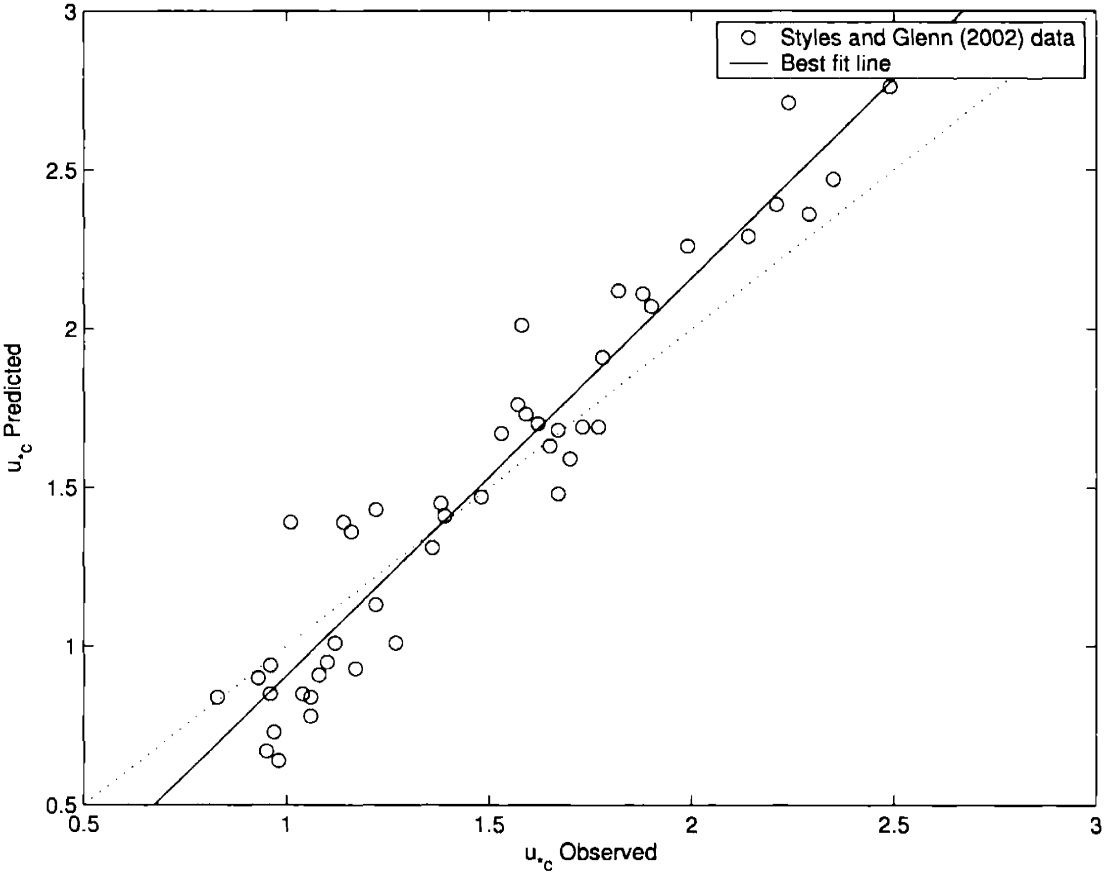

Figure 5-14: Comparison of observed and predicted u_{*c} using the two-layer Madsen-Salles model with $\gamma = 1$ and $k_n = 2.5\eta$ with field data used by Styles and Glenn (2002) where η is determined from (5.3). The average and standard deviation values of ϕ from (5.9) are 1.03 and 0.17, respectively. Note: 47 experiments were used in total; all 47 experiments with $X < 3$.

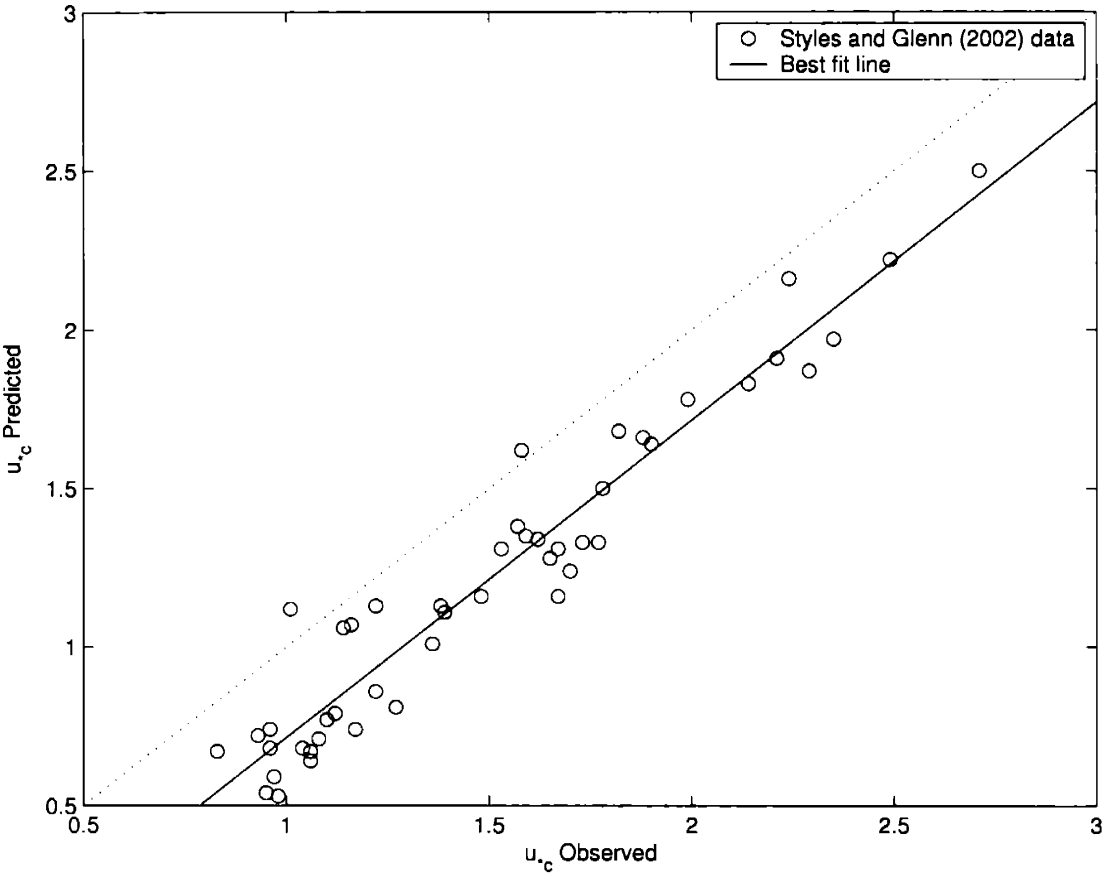

Figure 5-15: Comparison of observed and predicted u_{*c} using the three-layer Barreto-Acobe model and $k_n = 2.5\eta$ with field data used by Styles and Glenn (2002) where η is determined from (5.3). The average and standard deviation values of ϕ from (5.9) are 1.29 and 0.21, respectively. 47 experiments were used in total; all 47 experiments with $X < 3$.

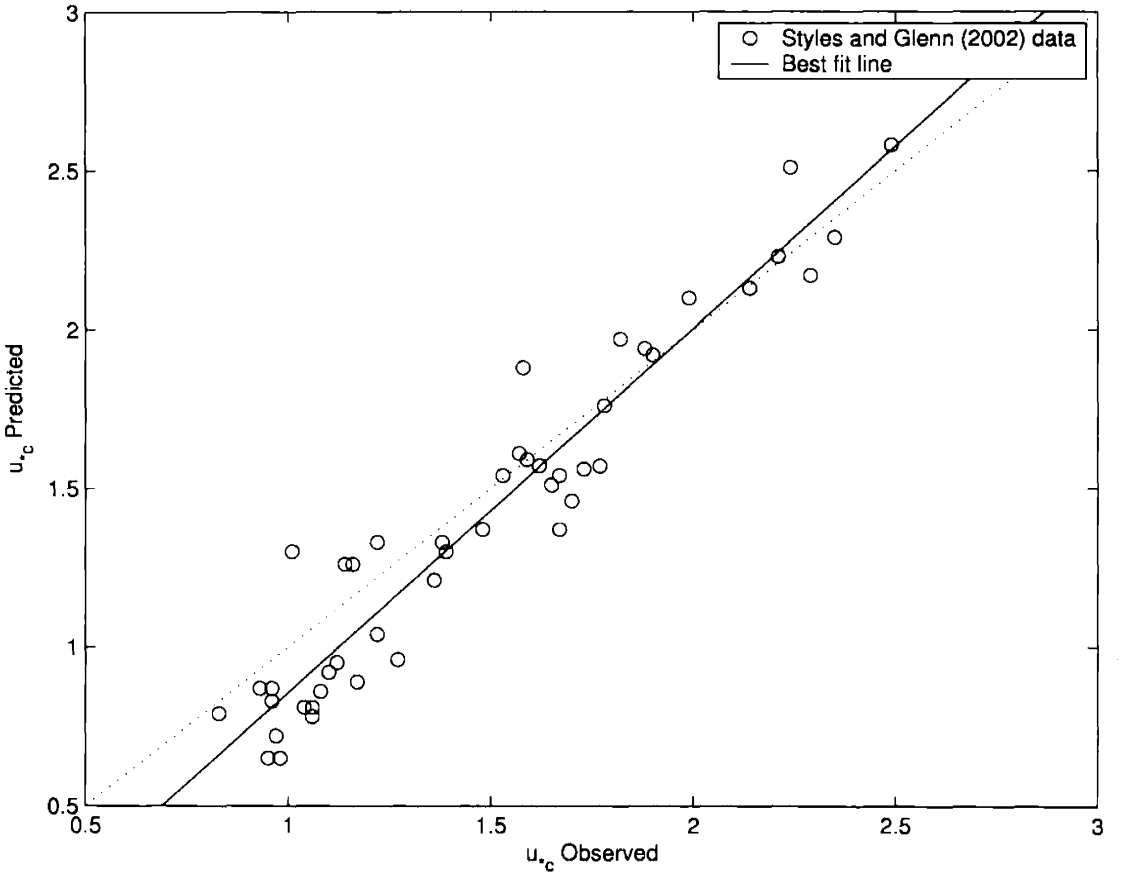

Figure 5-16: Comparison of observed and predicted u_{*c} using the three-layer Barreto-Acobe model and $k_n = 5\eta$ with field data used by Styles and Glenn (2002) where η is determined from (5.3). The average and standard deviation values of ϕ from (5.9) are 1.09 and 0.16, respectively. 47 experiments were used in total; all 47 experiments with $X < 3$.

5.3 Alternative Model of Wave-Generated Ripples

An alternative model for wave-generated ripples was considered for application with the ripple roughness and preferred flow models. Wikramanayake and Madsen (1990) applied the concept of the skin friction Shields parameter to the geometry of wave-generated ripples, where the skin friction Shields parameter is given by

$$\psi\prime = \frac{\tau\prime}{(s-1)\,\rho g d} \tag{5.10}$$

where

$$\tau\prime = \frac{1}{2} f_{w}\prime \rho U_{b_s}^2 \tag{5.11}$$

and $f_w\prime$ is defined as the wave friction factor (3.6) where $C_\mu = 1$ (pure wave motion) and the roughness, k_n, is replaced by d, the sediment grain diameter. For irregular wave experiments and (5.11), the significant values for the near-bottom orbital velocity and excursion amplitude were used, i.e. $U_{b_s} = \sqrt{2}U_b$ and $A_{b_s} = U_{b_s}/\omega$ where U_b is given by (4.3). Notice in Figure 3-1 that the friction factor approximations are nearly identical for the two-layer Madsen-Salles and the three-layer Barreto-Acobe flow models. With that being said, one can adopt either the friction factor approximation given by (3.6) and Table 3.2 corresponding to the two-layer Madsen-Salles model or (3.6) and Table 3.3 corresponding to the three-layer Barreto-Acobe model for application with (5.11). For the present context, the friction factor approximation given by (3.6) and Table 3.2 was adopted.

The empirical relationships for wave-generated ripples suggested by Wikramanayake and Madsen (1990) are given by

$$\frac{\eta}{A_b} = 0.276 - 0.33\sqrt{\psi\prime} \tag{5.12}$$

and

$$\frac{\eta}{\lambda} = 0.16 - 0.36\,(\psi\prime)^{2.3} \tag{5.13}$$

These relationships are valid for $\psi_{cr}\prime < \psi\prime < 0.7$, where $\psi_{cr}\prime$ is the critical Shields parameter required for initiation of motion of the sediment. Note that for $\psi\prime \geq 0.7$, sheet flow conditions exist and the sediment-fluid interface is a plane.

The relationships for η/A_b and λ/A_b are shown graphically for regular and irregular wave experiments in Figures 5-17, 5-18, 5-19, and 5-20. This model used the same data as the model developed in Section 5.1 and all data are tabulated and reported in Appendix A through Appendix E.

For the 338 regular wave experiments, the model performs well with the mean and standard deviation values of ϵ_1 from (5.6) 1.17 and 0.37, respectively. The mean and standard deviation values of ϵ_2 from (5.7) are 1.10 and 0.23, respectively. For the 205 irregular wave experiments, the mean and standard deviation values of ϵ_1 from (5.6) are 1.16 and 0.84, respectively. The mean and standard deviation values of ϵ_2 from (5.7) are 1.10 and 0.61, respectively. Even though this model was originally developed with monochromatic laboratory experimental data, the predicted values for both regular and irregular waves perform well on average. However, the performance of the model is compromised when one considers the relatively large standard deviation values, especially for irregular wave experiments. Therefore, the wave-generated ripple model developed in Section 5.1 was selected for the analyses presented in Section 5.2.

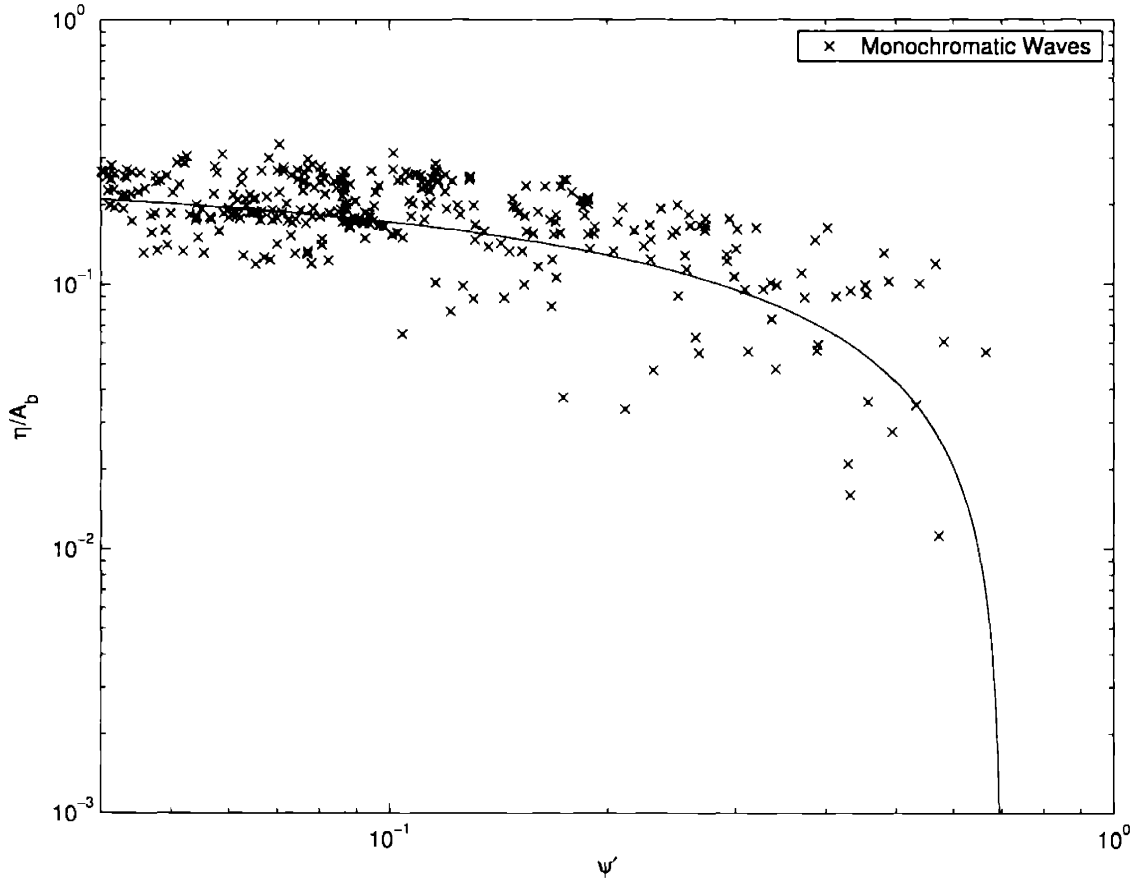

Figure 5-17: Relative ripple height as a function of the skin friction Shields parameter, $\psi\prime$. The solid line denotes the best fit curve, presented in (5.12). For regular waves, the average and standard deviation values of ϵ_1 from (5.6) are 1.17 and 0.37, respectively.

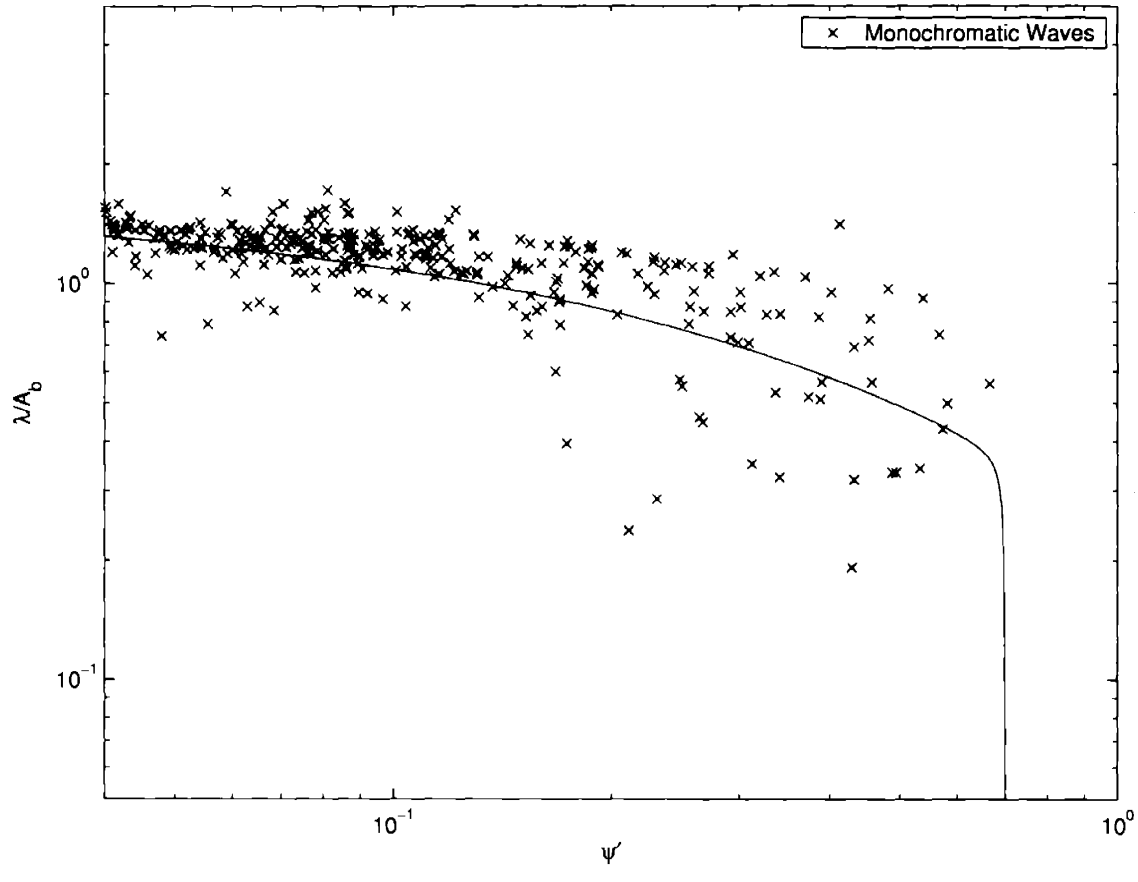

Figure 5-18: Relative ripple height as a function of the skin friction Shields parameter, $\psi\prime$. The solid line denotes the best fit curve, presented in (5.13). For regular waves, the average and standard deviation values of ϵ_2 from (5.7) are 1.10 and 0.23, respectively.

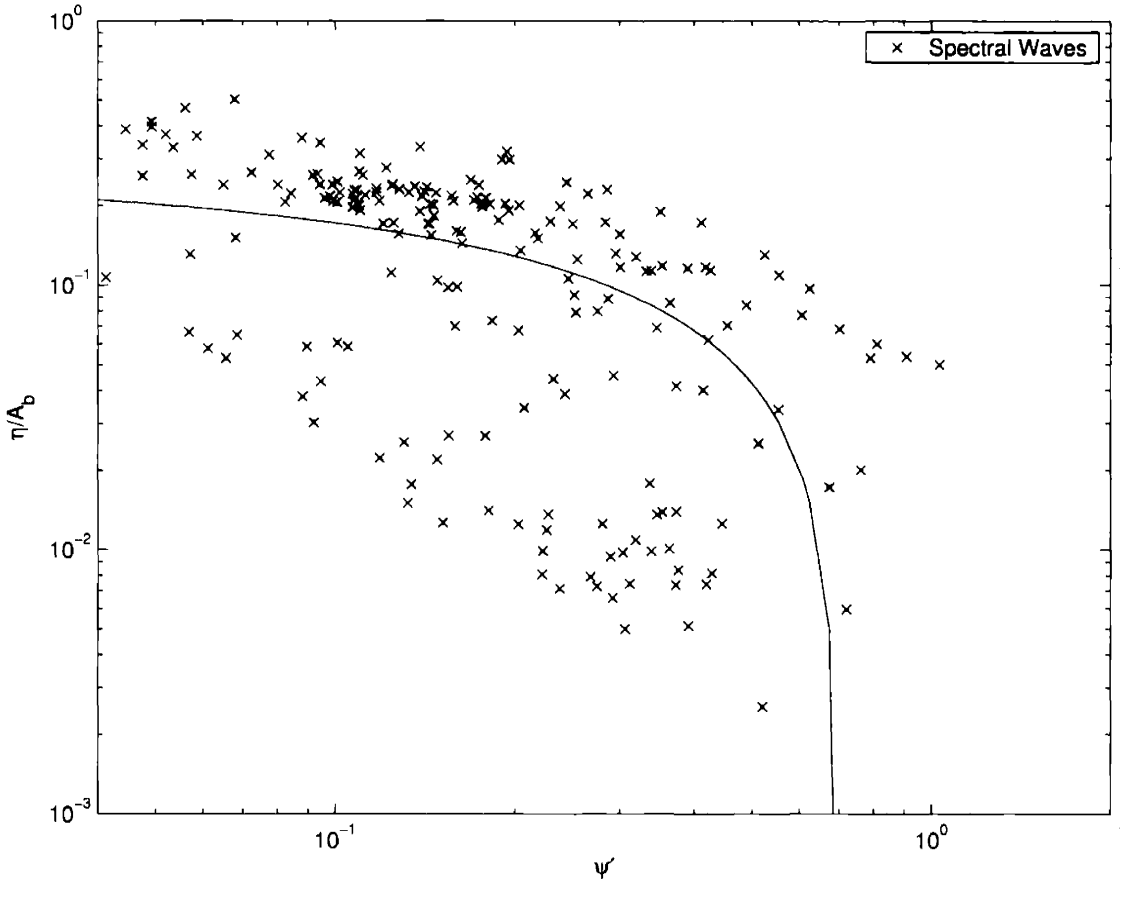

Figure 5-19: Relative ripple length as a function of the skin friction Shields parameter, $\psi\prime$. The solid line denotes the best fit curve, presented in (5.12). For irregular waves, the average and standard deviation values of ϵ_1 from (5.6) are 1.16 and 0.84, respectively.

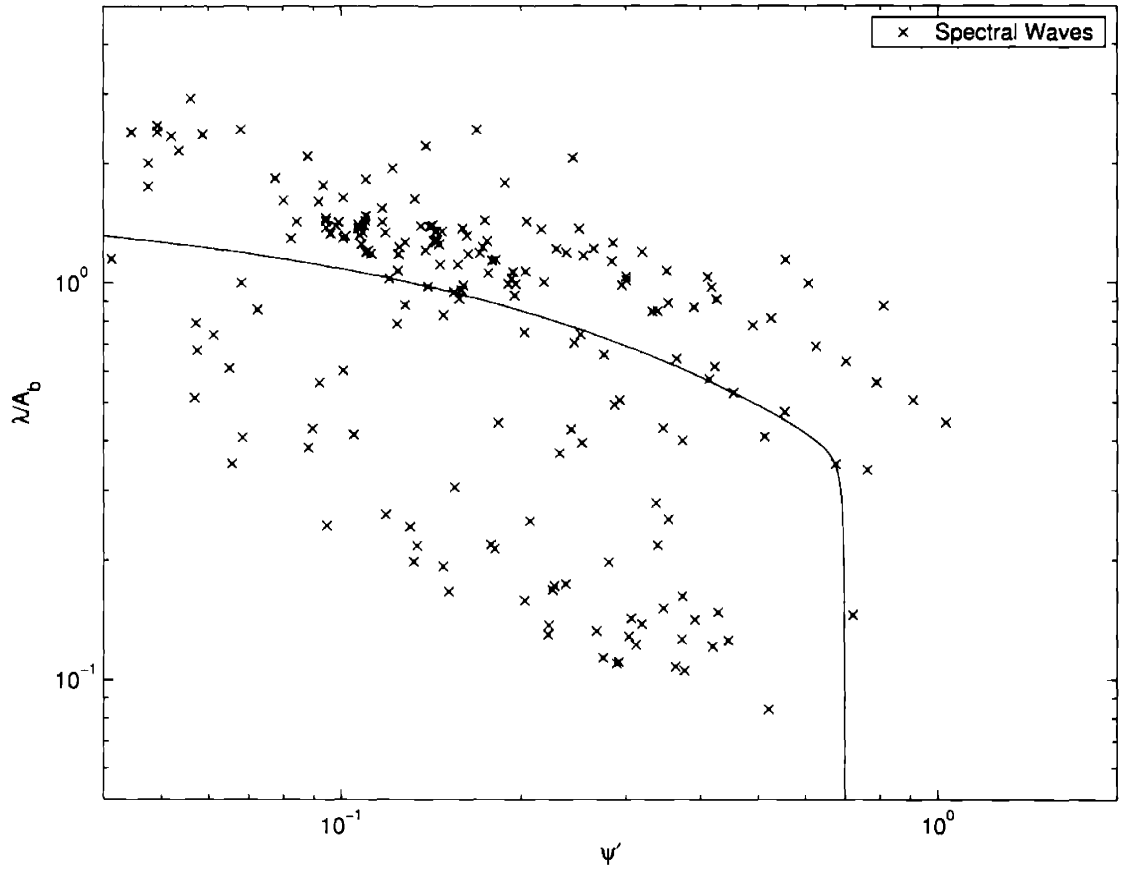

Figure 5-20: Relative ripple height as a function of the skin friction Shields parameter, $\psi\prime$. The solid line denotes the best fit curve, presented in (5.13). For irregular waves, the average and standard deviation values of ϵ_2 from (5.7) are 1.10 and 0.61, respectively.

Chapter 6

Conclusions

The main objective of this study was to present the evolution of simple models for turbulent wave-current bottom boundary layer flow, from the original two-layer Grant-Madsen (1979) model through a three-layer modified model presented by Barreto-Acobe (2001) and to arrive at a preferred flow model that adequately describes combined wave-current flow.

In the original two-layer Grant-Madsen (1979, 1986) model, there is an inconsistency in the model based on the definition of the eddy viscosity used in the wave problem and the current problem. Also, it is known that the wave-associated turbulence at the upper edge of the wave boundary layer should approach zero. Therefore, the increasing eddy viscosity defined in (2.17) for all heights above the bottom boundary that is used for the solution of the wave problem is physically unrealistic. Furthermore, since the eddy viscosity is discontinuous, the resulting current velocity profile is not smooth. The original Grant-Madsen model works well for small distances above the bottom (i.e. the wave-dominated region) and for heights within the current boundary layer that are not influenced by the wave boundary layer. However, it does not accurately predict the current velocity for the transition region between the wave-dominated region and the current-dominated region. In addition, the model performs poorly for large roughnesses because it inherently evaluates the

bottom boundary condition (no-slip) at $z = z_0$ and there can be a large gap in the velocity profile for $0 < z < z_0$ when dealing with large roughness elements.

Madsen and Salles (1998) developed a two-layer eddy viscosity model specially designed for very rough bottoms. They discovered that the wave boundary layer thickness is not simply proportional to the boundary layer length scale, i.e. α is not a constant. Instead, they found α to be a function of the relative roughness, as given in (3.1). Even though α is no longer a free parameter in their model, it is a function of a fitting parameter, γ in (3.1). A significant improvement of this model when compared to previous model developments is that the bottom boundary, no-slip condition can be applied at $z = 0$ by introducing the translation distance $z_b = z_0$. The result is a velocity profile that is identical to that of the classical Grant-Madsen model, but shifted downward so that the no-slip condition is applied at $z = 0$. Therefore, this model prevents the prediction of negative velocities for small values of z. A shortcoming of their model is that a fitting parameter is still involved and no single value of γ in (3.1) works well for all data sets as discussed in Section 3.1.2.

Madsen and Wikramanayake (1991) developed a three-layer eddy viscosity model removing some of the shortcomings of the original Grant-Madsen model. Two major improvements in their model include the use of the same eddy viscosity definition for both the wave and current problems and the use of a continuous eddy viscosity which results in a velocity profile that is smooth. However, there is still a model-specific fitting parameter, α, that must be determined for each application of the model. No single value of the fitting parameter works well for all data sets and a compromise must always be made depending on the data available. Since the model evaluates the bottom boundary, no-slip condition at $z = z_0$, there can be a large gap in the velocity profile for $0 < z < z_0$ when dealing with large roughness elements as is the case with the original Grant-Madsen model. Hence, the improved model also performs well for small roughnesses but does not perform very well for large roughnesses.

Barreto-Acobe (2001) developed a three-layer model that could apply the bottom

boundary, no-slip condition at either $z = 0$ or $z = z_0$. Her eddy viscosity model provides a continuous transition between the region where the turbulence is dominated by wave motion and the region where the turbulence is dominated by the current. Most importantly, however, the three-layered Barreto-Acobe model removes the necessity of fitting α to experimental data, by requiring this transition point between the wave and current dominated regions to be a pre-set fraction of the boundary layer thickness predicted by the model. This means that the model is entirely predictive and the dependence on application-specific fitting parameters is eliminated.

Based on the above discussion, the two preferred models that were selected for use throughout Chapters 4 and 5 of this text are the Madsen and Salles (1998) two-layer model and the Barreto-Acobe (2001) three-layer model. These models are the most physically realistic since they allow the bottom boundary no-slip condition to be applied at $z = 0$. It is also highly desirable that α is not simply a constant in each of these models. α is not a fitting parameter in the three-layer Barreto-Acobe flow model and α is a function of the relative roughness for the two-layer Madsen-Salles flow model.

Two ripple geometry and equivalent bed roughness models were developed in Chapter 4, of the forms presented in equations (4.1) and (4.2). Values for α_n and β_n were calculated using fixed and movable laboratory and field data. For the Mathisen and Madsen (1996) fixed bed laboratory data set, both wave attenuation and current profile data are available. Therefore, wave attenuation measurements were used in order to calculate the bottom roughness for the cases of pure waves and waves in the presence of a current while current measurements were used in order to establish the bottom roughness for the case of currents in the presence of waves. For the two-layer Madsen-Salles model with $\gamma = 1$, the ripple geometry and equivalent bed roughness models are statistically consistent for both movable and fixed laboratory data, regardless of whether wave attenuation data or current profile data were used in order to calculate the bottom roughness length scale, as seen in (4.7), (4.8), (4.9), (4.10),

(4.16), and (4.17). However, for the three-layer Barreto-Acobe flow model, the ripple geometry and equivalent bed roughness models using laboratory wave attenuation and current profile data are statistically different, as seen in (4.11), (4.12), (4.13), (4.14), (4.20), and (4.21).

All the models presented in this thesis assume that the bottom roughness may be described by a single roughness length scale, k_n. However, differences between roughness values for waves and currents can arise from bedform geometry and/or near-bottom flow characteristics. The experimental results of Mathisen and Madsen (1996) were used to check the single roughness assumption. While the three-layer Barreto-Acobe model yields smaller standard deviation values for the roughness, the two-layer Madsen-Salles model appears to be more robust in that one length scale, k_n, may be justifiably used for the cases of pure waves, waves in the presence of a current, and currents in the presence of waves. When using the three-layer Barreto-Acobe model with combined wave-current flow, one must use a roughness value that is application-specific, i.e. a different roughness value must be used depending on whether wave attenuation or current profile predictions are desired. In cases where current profiles are to be predicted, the roughness model that must be used with the three-layer Barreto-Acobe model is significantly larger when compared to the roughness model that must be be applied when wave attenuation is to be predicted.

Even though two ripple geometry and equivalent bed roughness models were presented in Chapter 4, the model of the form (4.1) involving the empirical constant α_n generally has smaller standard deviation values and therefore provides a better fit than the model involving β_n presented in (4.2), as seen in Tables 4.1 - 4.18. Therefore, the recommended conceptual model for practical applications involving movable bed data is of the form $k_n = \alpha_n \eta$.

The ripple geometry and roughness model that is statistically consistent with both the two-layer Madsen-Salles and the three-layer Barreto-Acobe flow models for the prediction of wave associated bottom shear stress using both movable and fixed bed

wave attenuation data from the *laboratory* is:

$$k_n = (11 \pm 6)\eta \tag{6.1}$$

The average and standard deviation values for α_n were calculated by equally weighting all laboratory data (movable and fixed bed) for the two-layer Madsen-Salles model and the three-layer Barreto-Acobe model.

Since the field is the natural environment for the application of the flow models presented in this thesis, the following ripple geometry and equivalent bed roughness model is statistically consistent with the *field* data presented in this chapter and is recommended for practical applications:

$$k_n = (2.5 \pm 2)\eta \tag{6.2}$$

It should be noted that $X < 3$ for all 47 combined flow field experiments. Therefore, the models can reliably be applied only for the range in which they were developed, i.e. for $X < 3$. We can expect that for $X > 3$, ripples start to be washed out, becoming three-dimensional with rounded crests. Most likely, these bedforms would have an α_n-value less than 2.5. At this point, we basically have no information from which to chose α_n for conditions when $X > 3$. However, based on the observation that laboratory data supports a single roughness model (6.1) regardless of whether $X < 3$ or $X > 3$, one can expect (with optimism) that a single roughness model would apply for all X-values with field data as well.

Notice that (6.2) is considerably smaller than the three-layer Barreto-Acobe field data results (4.22). This discrepancy is in accordance with the observation that a single roughness scale is not applicable when using the three-layer Barreto-Acobe flow model. Just as the results of the three-layer Barreto-Acobe model are larger when using current measurements when compared to wave attenuation measurements in

the laboratory, the same argument can be applied with field data. Since all of the laboratory wave attenuation measurements are statistically consistent, regardless of which flow model was used, and since one roughness length scale can be justifiably used for the two-layer Madsen-Salles model, one would expect that the Madsen-Salles field data results would be consistent with wave attenuation data (supposing that wave attenuation could be available for field data applications). Therefore, the significantly larger results obtained with the three-layer Barreto-Acobe model (4.22) are to be expected as a consequence of the roughness scale for currents in the presence of waves being larger than that for waves in the presence of currents.

It is not known at this time why the model recommended for field applications in (6.2) is much different from the model (6.1) that is consistent with the all of the laboratory data presented in this chapter. Since laboratory experiments usually involve superior accuracy of measurements, one may attribute the differences to scale effects since laboratory data also involves shorter wave periods. In addition, fixed bed laboratory data also involves sharper roughnesses and therefore the associated drag forces are different than drag forces typically encountered in the field. However, since the results of both fixed and movable bed laboratory data presented in this text are statistically consistent, this effect can be considered negligible in the present context.

In Chapter 5, wave and sediment characteristics were used to formulate a model for wave-generated ripples based on available laboratory and field data for movable and fixed beds. The two-layer Madsen-Salles flow model and the three-layer Barreto-Acobe flow model were then applied in conjunction with the ripple geometry and roughness models developed in Chapter 4 for the cases of known and unknown ripple geometry. Pure wave movable bed data from Carstens et al. (1969), Lofquist (1986), Rosengaus (1987), and Mathisen (1989) and combined wave-current data collected by Mathisen and Madsen (1996) and Styles and Glenn (2002) were used in order to assess the predictive capabilities of the preferred flow models. Predicted and observed values for f_w and u_{*c} were graphically depicted using the ripple geometry and roughness

relationships developed for the flow models.

Both the two-layer Madsen-Salles and three-layer Barreto-Acobe flow models performed reasonably well when applied in conjunction with the ripple geometry and roughness models developed in this thesis for the cases of known and unknown ripple geometry. For the case of movable bed laboratory data with *known* ripple geometry, the predicted values of f_w were on average approximately 6% less than the observed f_w values with a standard deviation of 30% with the two-layer Madsen-Salles model, and the predicted values of f_w were on average approximately 19% less than the observed f_w values with a standard deviation of 32% with the three-layer Barreto-Acobe model. For the case of movable bed laboratory data with *unknown* ripple geometry, 152 experiments were used in total; 88 experiments with $X < 3$ and 64 experiments with $X > 3$. The predicted values of f_w were on average approximately 21% less than the observed f_w values with a standard deviation of 26% for $X < 3$ and the predicted values of f_w were on average approximately 9% greater than the observed f_w values with a standard deviation of 25% for $X > 3$ with the two-layer Madsen-Salles model. For the case of movable bed laboratory data with unknown ripple geometry, the predicted values of f_w were on average approximately 35% less than the observed f_w values with a standard deviation of 29% for $X < 3$ and the predicted values of f_w were on average approximately 6% greater than the observed f_w values with a standard deviation of 28% for $X > 3$ with the three-layer Barreto-Acobe model.

For the case of combined flow fixed bed laboratory data, the predicted values of u_{*c} were on average approximately 9% less than the observed u_{*c} values with a standard deviation of 8% with the two-layer Madsen-Salles model with $\gamma = 1$, and the predicted values of u_{*c} were on average approximately 31% less than the observed u_{*c} values with a standard deviation of 9% with the three-layer Barreto-Acobe model. However, based on the fact that the three-layer Barreto-Acobe flow model requires multiple roughness length scales, i.e. $k_{cw} > k_{wc}$ for the three-layer Barreto-Acobe model, a larger α_n-value should be used in conjunction with this model to improve

the performance for the prediction of the current shear velocity (Figure 5-10).

For the case of combined flow field data with *known* ripple geometry, the predicted values of u_{*c} were on average approximately 2% greater than the observed u_{*c} values with a standard deviation of 20% for the two-layer Madsen-Salles model with $\gamma = 1$, and the predicted values of u_{*c} were on average approximately 24% less than the observed u_{*c} values with a standard deviation of 25% for the three-layer Barreto-Acobe model. Again, based on the fact that the three-layer Barreto-Acobe flow model requires multiple roughness length scales, i.e. $k_{cw} > k_{wc}$ for the three-layer Barreto-Acobe model, a larger α_n-value should be used in conjunction with this model to improve the performance for the prediction of the current shear velocity (Figure 5-13). For the case of combined flow field data with *unknown* ripple geometry, 47 experiments were used in total; all 47 experiments with $X < 3$. The predicted values of u_{*c} were on average approximately 3% less than the observed u_{*c} values with a standard deviation of 17% for the two-layer Madsen-Salles model with $\gamma = 1$, and the predicted values of u_{*c} were on average approximately 29% less than the observed u_{*c} values with a standard deviation of 21% for the three-layer Barreto-Acobe model. Again, based on the fact that the three-layer Barreto-Acobe flow model requires multiple roughness length scales, i.e. $k_{cw} > k_{wc}$ for the three-layer Barreto-Acobe model, a larger α_n-value should be used in conjunction with this model to improve the performance for the prediction of the current shear velocity (Figure 5-16).

Since one universal roughness length scale is applicable for the two-layer Madsen-Salles flow model with $\gamma = 1$, i.e. $k_w \approx k_{wc} \approx k_{cw}$, the two-layer Madsen-Salles model with $\gamma = 1$ is chosen as the preferred model for future applications. However, if a theoretical justification for different roughness scales to account for the effects of waves and currents over ripples could be formed, then the three-layer Barreto-Acobe model would be selected as the preferred flow model.

For future research, it is recommended to further investigate the roughness length scales with movable bed data, especially field data with values of $X > 3$. Particularly,

we have found from field data, all of which had $X < 3$, that (6.2) applies. Based on the observation that laboratory data supports a single roughness model (6.1) regardless of whether $X < 3$ or $X > 3$, one can expect (with optimism) that a single roughness model would apply for all X-values with field data as well. Field data with values of $X > 3$ could be used to check this assumption. Additionally, it is recommended to explore improved models for wave-generated ripples.

Appendix A

Monochromatic Pure Wave Experiments

Table A.1: Fixed Bed Attenuation Results for Monochromatic Pure Wave Experiments from Madsen and Mathisen (1996)

A_b (cm)	ω (1/s)	λ (cm)	η (cm)	f_e
6.09	2.80	10	1.5	0.3
7.9	2.39	10	1.5	0.22
8.84	2.17	10	1.5	0.18
4.2	2.80	10	1.5	0.36
5.72	2.39	10	1.5	0.29
6.21	2.17	10	1.5	0.27
5.96	2.80	20	1.5	0.15
7.97	2.39	20	1.5	0.13
9.15	2.17	20	1.5	0.1

Table A.2: Fixed Bed Oscillatory Data on Energy Dissipation over Fixed Ripples with Regular Waves from Bagnold (1946), $\lambda = 10$ cm

A_b (cm)	ω (1/s)	λ (cm)	η (cm)	f_e
5	3.13	10	1.5	0.206
5	3.88	10	1.5	0.254
5	5.86	10	1.5	0.3
5	8.2	10	1.5	0.265
5	9.66	10	1.5	0.245
10	1.24	10	1.5	0.233
10	1.38	10	1.5	0.246
10	1.79	10	1.5	0.224
10	1.94	10	1.5	0.223
10	2.64	10	1.5	0.237
10	2.66	10	1.5	0.196
10	3.76	10	1.5	0.237
10	5.72	10	1.5	0.208
15.25	1.23	10	1.5	0.139
15.25	1.61	10	1.5	0.146
15.25	1.64	10	1.5	0.154
15.25	2.57	10	1.5	0.138
15.25	2.59	10	1.5	0.15
15.25	2.86	10	1.5	0.164
15.25	3.2	10	1.5	0.144
15.25	3.55	10	1.5	0.155
15.25	4.21	10	1.5	0.137

Table A.3: Fixed Bed Oscillatory Data on Energy Dissipation over Fixed Ripples with Regular Waves from Bagnold (1946), $\lambda = 10$ cm; continued

A_b (cm)	ω (1/s)	λ (cm)	η (cm)	f_e
20.3	0.814	10	1.5	0.115
20.3	1.12	10	1.5	0.126
20.3	1.67	10	1.5	0.134
20.3	2.48	10	1.5	0.132
20.3	2.58	10	1.5	0.152
30.5	0.671	10	1.5	0.096
30.5	1.07	10	1.5	0.088
30.5	1.35	10	1.5	0.091
30.5	1.65	10	1.5	0.083
30.5	1.78	10	1.5	0.092

Table A.4: Fixed Bed Oscillatory Data on Energy Dissipation over Fixed Ripples with Regular Waves from Bagnold (1946), $\lambda = 20$ cm

A_b (cm)	ω (1/s)	λ (cm)	η (cm)	f_e
5	2.38	20	3	0.294
5	3.51	20	3	0.244
5	5.73	20	3	0.232
5	7.62	20	3	0.257
5	8.48	20	3	0.283
10	1.34	20	3	0.231
10	2.2	20	3	0.251
10	3.41	20	3	0.219
10	3.64	20	3	0.217
10	4.01	20	3	0.255
10	5.17	20	3	0.196
15.25	0.762	20	3	0.262
15.25	1.17	20	3	0.223
15.25	1.67	20	3	0.229
15.25	2.15	20	3	0.247
15.25	2.77	20	3	0.189
15.25	3.07	20	3	0.199

Table A.5: Fixed Bed Oscillatory Data on Energy Dissipation over Fixed Ripples with Regular Waves from Bagnold (1946), $\lambda = 20$ cm; continued

A_b (cm)	ω (1/s)	λ (cm)	η (cm)	f_e
20.3	1.16	20	3	0.199
20.3	1.49	20	3	0.224
20.3	1.73	20	3	0.214
20.3	1.9	20	3	0.211
20.3	2.3	20	3	0.178
30.5	0.561	20	3	0.13
30.5	0.759	20	3	0.139
30.5	0.919	20	3	0.146
30.5	1.07	20	3	0.143
30.5	1.2	20	3	0.153

Table A.6: Fixed Bed Oscillatory Data on Energy Dissipation over Fixed Ripples with Regular Waves from Sleath (1985)

A_b (cm)	ω (1/s)	λ (cm)	η (cm)	f_e
3.21	1.64	7.3	1.7	0.0486
3.21	2.2	7.3	1.7	0.0699
3.21	3.08	7.3	1.7	0.124
3.21	5.05	7.3	1.7	0.179
5.18	0.86	7.3	1.7	0.063
5.18	1.18	7.3	1.7	0.143
5.18	1.64	7.3	1.7	0.166
5.18	2.14	7.3	1.7	0.172
5.18	2.14	7.3	1.7	0.187
5.18	3.86	7.3	1.7	0.195
5.18	5.3	7.3	1.7	0.185
6.42	0.72	7.3	1.7	0.07
6.42	0.98	7.3	1.7	0.104
6.42	1.96	7.3	1.7	0.197
6.42	2.25	7.3	1.7	0.205
6.42	3.76	7.3	1.7	0.176
6.42	4.36	7.3	1.7	0.186
6.42	4.79	7.3	1.7	0.188
6.42	5	7.3	1.7	0.178
6.42	5.53	7.3	1.7	0.186
7.66	1.58	7.3	1.7	0.157
7.66	2.49	7.3	1.7	0.191
7.66	4.9	7.3	1.7	0.178
7.66	5.71	7.3	1.7	0.172

Table A.7: Fixed Bed Oscillatory Data on Energy Dissipation over Fixed Ripples with Regular Waves from Sleath (1985); continued

A_b (cm)	ω (1/s)	λ (cm)	η (cm)	f_e
10.3	0.565	7.3	1.7	0.0246
10.3	0.91	7.3	1.7	0.118
10.3	0.99	7.3	1.7	0.133
10.3	1.73	7.3	1.7	0.151
10.3	2.74	7.3	1.7	0.151
10.3	3.07	7.3	1.7	0.158
10.3	3.85	7.3	1.7	0.153
10.3	4.57	7.3	1.7	0.146
10.3	4.98	7.3	1.7	0.143
10.3	4.99	7.3	1.7	0.149
15.4	0.438	7.3	1.7	0.0369
15.4	0.452	7.3	1.7	0.0649
15.4	0.644	7.3	1.7	0.0634
15.4	0.616	7.3	1.7	0.0679
15.4	0.473	7.3	1.7	0.0752
15.4	0.851	7.3	1.7	0.1
15.4	1.1	7.3	1.7	0.103
15.4	1.73	7.3	1.7	0.113
15.4	2.08	7.3	1.7	0.118
15.4	2.7	7.3	1.7	0.125
15.4	2.7	7.3	1.7	0.118
15.4	3.31	7.3	1.7	0.115
15.4	3.83	7.3	1.7	0.112

Table A.8: Fixed Bed Oscillatory Data on Energy Dissipation over Fixed Ripples with Regular Waves from Sleath (1985); continued

A_b (cm)	ω (1/s)	λ (cm)	η (cm)	f_e
20.5	0.346	7.3	1.7	0.04
20.5	0.513	7.3	1.7	0.0561
20.5	0.745	7.3	1.7	0.083
20.5	1.18	7.3	1.7	0.0917
20.5	1.5	7.3	1.7	0.0932
20.5	1.91	7.3	1.7	0.103
20.5	2.43	7.3	1.7	0.105
20.5	2.81	7.3	1.7	0.103
30.8	0.37	7.3	1.7	0.0465
30.8	0.727	7.3	1.7	0.0624
30.8	0.922	7.3	1.7	0.0676
30.8	1.23	7.3	1.7	0.0747
30.8	1.75	7.3	1.7	0.0736
30.8	2.19	7.3	1.7	0.0823

Table A.9: Movable Bed Wave Tunnel Data on Ripple Geometry and Energy Dissipation under Regular Waves from Carstens et al. (1969)

A_b (cm)	ω (1/s)	λ (cm)	η (cm)	f_e
8.92	1.77	10.6	1.8	0.265
11.99	1.77	12.7	2.2	0.198
13.66	1.77	14.5	2.6	0.18
15.37	1.77	14.5	2.6	0.183
20.85	1.77	19.4	3.3	0.142
23.39	1.77	22.1	3.6	0.155
26.11	1.78	24.5	3.23	0.155
32.39	1.77	27	3.1	0.115
35.6	1.78	20.1	2.1	0.106
44.5	1.78	19.1	0.5	0.077
39.05	1.78	22	1.4	0.0717
28.08	1.77	24.5	3.2	0.134
8	1.76	10.4	1.9	0.385
18.16	1.77	10.9	1.5	0.112
23.7	1.78	10.6	1.3	0.0914
31.33	1.78	10	0.5	0.0849
8.18	1.77	10.4	2.1	0.202

Table A.10: Movable Bed Wave Tunnel Data on Ripple Geometry and Energy Dissipation under Regular Waves from Carstens et al. (1969); continued

A_b (cm)	ω (1/s)	λ (cm)	η (cm)	f_e
10.11	1.76	14.6	2.8	0.254
12.01	1.77	16.7	3.3	0.279
13.77	1.77	18.1	3.4	0.34
16.07	1.77	20.4	3.9	0.321
18.54	1.78	23.9	4.5	0.211
19.65	1.761	25.2	5.2	0.326
22.35	1.77	29	5.8	0.293
24.19	1.77	25.7	4.8	0.277
24.77	1.78	26.4	4.9	0.27
26.64	1.78	30	5.6	0.254
29.08	1.77	26.2	5	0.256
30.8	1.76	30.4	6	0.257
32.68	1.77	39.1	5.6	0.244
35.18	1.78	37.8	6.8	0.225
37.43	1.77	35.7	6.2	0.226
39.22	1.81	46.3	6.9	0.202
42.35	1.77	44.11	6.9	0.199
12.45	1.78	17.4	3.1	0.517

Table A.11: Movable Bed Wave Flume Data on Ripple Geometry and Energy Dissipation under Irregular Waves from Mathisen (1989) and Rosengaus (1987)

A_b (cm)	ω (1/s)	λ (cm)	η (cm)	f_e
6.43	2.51	8.2	1.1	0.0981
5.5	2.51	7.9	1.1	0.084
6.86	2.51	9.4	1.1	0.0772
6.93	2.51	9.1	1.1	0.095
5.76	2.51	7.7	1.2	0.116
6.48	2.51	8.3	1	0.122
6.46	2.51	8.7	1.1	0.159
5.42	2.51	7.6	1.2	0.271
6.95	2.51	8.2	1	0.166

Table A.12: Movable Bed Wave Flume Data on Ripple Geometry and Energy Dissipation under Regular Waves from Mathisen (1989) and Rosengaus (1987)

A_b (cm)	ω (1/s)	λ (cm)	η (cm)	f_e
9.08	2.39	9.9	1.6	0.173
5.55	2.39	7.4	1.3	0.243
7.23	2.39	8.9	1.5	0.223
12.05	2.39	10.6	1.6	0.18
6.07	2.9	8.6	1.3	0.165
9.16	2.03	10.2	1.6	0.113
6.43	2.62	8.7	1.4	0.187
9.27	2.39	10.9	1.7	0.177
9.01	2.39	10.1	1.6	0.156
4.61	2.39	6.5	1.2	0.193
6.44	2.39	8.1	1.3	0.19
8	2.39	8.8	1.2	0.107
9.39	2.39	9.2	1.3	0.094

Table A.13: Movable Bed Wave Flume Data on Ripple Geometry and Energy Dissipation under Regular Waves from Mathisen (1989) and Rosengaus (1987); continued

A_b (cm)	ω (1/s)	λ (cm)	η (cm)	f_e
10.3	2.39	9	1.2	0.084
7.16	2.39	8.9	1.3	0.178
4.75	2.51	7.7	1.1	0.195
8.1	2.51	8.6	1	0.0557
5.24	2.51	8.5	1.2	0.205
5.53	2.51	8.2	1.5	0.165
5.28	2.51	8	1.4	0.214
5.53	2.51	8.2	1.4	0.174
5.59	2.39	8.7	1.5	0.272
5.31	2.39	9.1	1.5	0.225
5.73	2.39	9.1	1.5	0.144
6.07	2.39	8.5	1.4	0.238
5.49	2.39	8.6	1.5	0.19

Table A.14: Movable Bed Wave Tunnel Data on Energy Dissipation over Equilibrium Ripples with Regular Waves from Lofquist (1986)

A_b (cm)	ω (1/s)	λ (cm)	η (cm)	f_e
26.9	0.86	31.8	3.8	0.126
30.7	0.75	36.4	4.1	0.13
29.9	0.63	36.4	4	0.13
29.3	0.53	36.4	4.2	0.15
30.7	0.75	36.4	4	0.124
33.5	0.89	36	3.3	0.159
36.7	0.63	42.4	4.8	0.11
34.7	0.54	42.4	4.9	0.128
39.3	0.76	42.2	3.1	0.126
44.3	0.52	50.9	6.3	0.14
42.7	0.44	50.9	6.7	0.171
48.3	0.62	50.9	4.9	0.15
26.9	0.86	31.8	4	0.127
25.9	0.73	31.8	3.9	0.167
29.5	1.01	31	2.6	0.168
19.6	1.18	23.1	3.2	0.189
19	1	23.1	3.4	0.183
14.4	1.61	17	2.4	0.211
14	1.35	17	2.6	0.223
55.3	0.42	65.3	7	0.139

Table A.15: Movable Bed Wave Tunnel Data on Energy Dissipation over Equilibrium Ripples with Regular Waves from Lofquist (1986); continued

A_b (cm)	ω (1/s)	λ (cm)	η (cm)	f_e
23.9	1.13	31.8	7.1	0.285
23.9	1.69	31.8	6.8	0.218
23.9	1.38	31.8	7.1	0.248
31.9	1.04	42.4	8.5	0.255
25.5	1.3	31.8	6.7	0.247
22	1.51	31.8	6.1	0.258
20.6	1.6	31.8	5.4	0.211
27.7	1.2	34	6.9	0.264
17.4	1.56	23.1	4.6	0.218
17.4	1.9	23.1	4.5	0.269
17.4	2.33	23.1	4.4	0.283
17.4	2.33	23.1	4.3	0.277
31.9	1.04	42.4	8.8	0.289
31.9	0.849	42.4	8.2	0.315
23.9	1.69	31.8	6.5	0.184
25.9	2.01	31.8	5.2	0.181
28.9	2.21	31.8	4.8	0.163
23.3	1.42	31.8	6.6	0.212
23.3	1.16	31.8	6.7	0.271
23.7	1.7	31.8	6.3	0.183
25.5	2.04	31.8	5.4	0.186

Table A.16: Movable Bed Wave Tunnel Data on Energy Dissipation over Equilibrium Ripples with Regular Waves from Lofquist (1986); continued

A_b (cm)	ω (1/s)	λ (cm)	η (cm)	f_e
28.9	2.21	31.8	5.1	0.142
17.2	1.93	23.1	4.6	0.275
17.2	1.57	23.1	4.8	0.224
17.6	2.31	23.1	4.5	0.257
24.1	1.68	31.8	6.4	0.182
25.5	1.59	31.8	6.4	0.175
22	1.84	31.8	5.7	0.164
20.8	1.95	31.8	5.1	0.184
27.5	1.47	31.8	6.3	0.177
31.9	1.27	43.5	8.2	0.283
31.9	1.63	39.5	7.9	0.24
38.3	0.71	52.2	10.1	0.348
38.3	0.87	58	11.5	0.351
38.3	1.06	58	12	0.314
31.1	1.68	37.3	6.9	0.236
33.9	1.88	37.3	6.2	0.199
28.33	1.43	37.3	7.3	0.22
27.9	1.18	37.3	7.2	0.277
27.5	0.98	37.3	7.1	0.273
33.92	1.54	43.5	8.4	0.215
35.1	1.49	43.5	8.2	0.247

Table A.17: Movable Bed Wave Tunnel Data on Energy Dissipation over Equilibrium Ripples with Regular Waves from Lofquist (1986); continued

A_b (cm)	ω (1/s)	λ (cm)	η (cm)	f_e
38.7	1.65	43.5	7.7	0.184
32.3	1.25	43.5	8.6	0.253
31.9	1.03	43.5	8.6	0.317
31.9	0.85	43.5	7.8	0.345
38.3	0.86	52.2	10.3	0.309
38.3	0.7	52.2	10.2	0.395
38.7	1.05	52.2	10.5	0.281
41.9	1.25	52.2	9.8	0.229
46.3	1.38	52.2	8.9	0.238
47.9	0.69	65.3	12.6	0.33
47.9	0.56	65.3	13.5	0.415
48.3	0.84	65.3	12.9	0.329
51.9	1.01	65.3	12.2	0.248
24.3	1.65	28.1	5.8	0.178
24.3	1.35	28.9	5.9	0.198
24.3	1.11	30.3	5.8	0.236
26.7	1.95	30.2	5.5	0.15
29.5	2.17	31.2	4.7	0.128
24.3	1.63	28.8	5.6	0.191
24.3	1.63	29	5.9	0.209

Table A.18: Movable Bed Wave Flume Data on Ripple Geometry under Regular Waves from Inman and Bowen (1963); $d = 0.2$ mm and $s = 2.65$

A_b **(cm)**	ω **(1/s)**	λ **(cm)**	η **(cm)**
4.9	4.49	6.5	1.1
9.6	3.14	10.8	1.5

Table A.19: Movable Bed Wave Flume Data on Ripple Geometry under Regular Waves from Kennedy and Falcon (1965); $d = 0.095$ mm and $s = 2.65$

A_b **(cm)**	ω **(1/s)**	λ **(cm)**	η **(cm)**
2.08	5.87	3.0	0.51
3.88	3.22	4.9	0.82
5.39	3.22	5.6	1.1
5.78	2.69	5.5	1.0

Table A.20: Movable Bed Wave Flume Data on Ripple Geometry under Regular Waves from Kennedy and Falcon (1965); $d = 0.32$ mm and $s = 2.65$

A_b **(cm)**	ω **(1/s)**	λ **(cm)**	η **(cm)**
4.99	4.52	6.3	1.0
5.33	4.00	7.2	1.2
6.47	4.00	8.6	1.6
4.79	4.52	6.2	1.2
4.26	4.00	5.9	1.3
3.24	4.52	4.6	0.7

Table A.21: Movable Bed Wave Tunnel Data on Ripple Geometry under Regular Waves from Lambie (1984); $d = 0.09$ mm and $s = 2.65$

A_b (cm)	ω (1/s)	λ (cm)	η (cm)
11.0	1.09	11.6	1.45
39.0	1.09	55.0	3.5
14.5	1.05	12.4	1.8
8.0	2.73	7.6	1.4
20.25	1.14	21.2	1.8
21.0	1.14	15.6	2.1
13.0	1.40	14.0	2.0
10.5	2.00	10.5	1.5
8.5	2.17	11.0	2.1
10.5	2.17	10.6	1.3
19.5	2.17	6.5	2.0
7.75	2.73	6.6	1.2
11.25	2.73	8.0	1.2
9.0	2.73	7.5	1.2
17.5	1.40	18.0	2.7
14.5	2.00	8.3	2.3

Table A.22: Movable Bed Wave Tunnel Data on Ripple Geometry under Regular Waves from Lambie (1984); $d = 0.15$ mm and $s = 2.65$

A_b (cm)	ω (1/s)	λ (cm)	η (cm)
19.75	1.34	18.2	2.9
19.75	1.34	23.0	3.3
6.75	2.24	11.5	2.1
10.25	2.24	12.5	2.3
11.75	2.31	13.2	2.2
21.75	1.63	25.3	3.2
19.25	1.64	20.3	4.0
16.75	1.64	18.5	3.3
13.90	1.64	16.3	2.8
10.15	1.63	11.5	1.8
15.5	1.06	17.2	2.8
25.5	1.63	22.2	4.1
24.0	1.62	20.4	4.0
39.4	1.19	33.0	3.9

Table A.23: Movable Bed Wave Tunnel Data on Ripple Geometry under Regular Waves from Lambie (1984); $d = 0.15$ mm and $s = 2.65$; continued

A_b (cm)	ω (1/s)	λ (cm)	η (cm)
36.0	1.19	30.5	4.4
28.0	1.19	27.0	3.8
26.3	1.19	24.0	4.8
17.7	1.19	20.2	3.4
9.75	1.19	18.8	3.1
9.15	1.19	9.4	1.4
12.6	1.19	9.3	1.7
11.5	1.19	13.8	2.6
37.75	0.87	29.7	4.0
21.0	1.37	17.3	2.8
40.5	1.34	33.0	3.7
15.0	2.24	17.0	2.5
18.75	2.24	20.0	1.9

Table A.24: Movable Bed Wave Tunnel Data on Ripple Geometry under Regular Waves from Lofquist (1978); $d = 0.18$ mm and $s = 2.65$

A_b **(cm)**	ω **(1/s)**	λ **(cm)**	η **(cm)**
11.4	2.11	14.0	2.0
11.4	1.92	14.0	1.7
11.4	2.32	13.3	1.8
9.27	2.29	11.4	1.6
18.3	1.14	21.0	2.8
27.5	0.83	26.8	3.3

Table A.25: Movable Bed Wave Tunnel Data on Ripple Geometry under Regular Waves from Lofquist (1978); $d = 0.55$ mm and $s = 2.65$

A_b (cm)	ω (1/s)	λ (cm)	η (cm)
45.8	0.76	72.7	15.5
45.9	0.78	58.4	12.4
49.7	0.56	55.1	10.9
36.7	0.96	55.3	10.1
36.7	1.18	42.8	8.9
36.7	1.48	40.1	7.6
23.0	1.51	27.9	5.4
30.1	1.20	32.7	6.5
36.7	0.78	50.1	10.6
19.3	1.84	24.9	4.3
13.9	2.23	23.9	3.5
15.1	2.05	22.9	3.50
13.8	2.32	20.8	3.2
14.3	2.27	19.0	3.4
24.5	1.41	31.9	6.0
11.9	2.77	10.9	2.8
23.8	1.45	25.4	5.5
18.3	1.83	27.4	4.1
27.6	1.41	33.7	6.8
27.6	2.79	26.2	4.5
13.7	2.32	21.8	3.4
13.8	1.90	16.0	2.2
13.7	1.35	16.0	2.0

Table A.26: Movable Bed Wave Flume Data on Ripple Geometry under Regular Waves from Miller and Komar (1980); $d = 0.178$ mm and $s = 2.65$

A_b (cm)	ω (1/s)	λ (cm)	η (cm)
7.59	2.09	6.0	1.0
8.37	2.09	7.5	1.0
15.40	1.57	13.5	1.0
26.80	1.26	10.6	1.0

Table A.27: Movable Bed Wave Tunnel Data on Ripple Geometry under Regular Waves from Mogridge and Kamphuis (1972); $d = 0.36$ mm and $s = 2.65$

A_b (cm)	ω (1/s)	λ (cm)	η (cm)
77.6	0.78	42.7	7.0
9.4	2.50	12.9	2.1
15.7	1.56	19.7	3.3
15.6	1.56	20.0	3.4
25.8	1.56	28.1	4.8
21.8	1.11	28.4	4.8
29.4	1.11	37.7	5.8
32.0	1.56	33.8	5.1
36.0	0.781	44.3	6.8
42.8	0.781	50.0	8.8
51.9	0.781	54.8	9.5
53.7	0.625	60.1	10.1
60.9	0.521	65.0	10.4
66.8	0.521	73.5	11.5
75.4	0.447	81.2	13.6
93.0	0.447	101.7	18.4
13.5	1.56	17.2	3.0
21.1	1.56	25	3.8
29.7	1.56	33.0	4.6
38.0	1.56	27.8	4.9
43.9	1.56	22.7	3.9

Table A.28: Movable Bed Wave Flume Data on Ripple Geometry under Regular Waves from Mogridge and Kamphuis (1972); $d = 0.36$ mm and $s = 2.65$

A_b (cm)	ω (1/s)	λ (cm)	η (cm)
2.50	5.77	3.3	0.57
2.69	5.81	3.6	0.50
3.00	5.82	3.7	0.53
3.22	5.82	4.0	0.64
3.40	5.81	4.2	0.65
3.66	5.81	4.8	0.66
3.13	5.79	4.4	0.61
2.91	5.82	3.6	0.51
3.27	5.780	4.3	0.61
2.93	5.800	3.8	0.53
2.74	5.820	3.4	0.44
3.30	5.800	4.3	0.62

Table A.29: Movable Bed Wave Flume Data on Ripple Geometry under Regular Waves from Mogridge and Kamphuis (1972); $d = 0.36$ mm and $s = 2.65$

A_b (cm)	ω (1/s)	λ (cm)	η (cm)
3.00	5.810	3.6	0.54
3.98	5.900	4.9	0.69
4.03	5.770	5.36	0.75
4.17	5.780	5.0	0.69
3.51	5.80	4.5	0.61
4.28	5.78	5	0.67
3.90	5.78	5.0	0.65
2.62	6.27	3.2	0.48
2.25	6.28	3	0.44
2.83	6.26	4.0	0.54
3.61	6.28	4.5	0.62
3.14	6.23	4.0	0.56
3.30	6.27	4.1	0.56
2.89	6.24	3.7	0.54

Table A.30: Movable Bed Wave Flume Data on Ripple Geometry under Regular Waves from Mogridge and Kamphuis (1972); $d = 0.36$ mm and $s = 2.65$; continued

A_b (cm)	ω (1/s)	λ (cm)	η (cm)
3.24	6.26	4.2	0.57
3.66	6.28	4.6	0.62
3.07	4.99	4.5	0.67
4.00	5.01	5.2	0.70
3.57	4.99	4.8	0.69
3.81	5.00	5.1	0.80
2.92	4.98	3.5	0.53
3.05	5.00	4.2	0.59
2.97	5.00	4.1	0.59
5.57	2.50	6.6	1.15
8.78	2.50	7.7	1.13
5.88	2.50	7.0	1.31
5.55	2.50	6.6	1.00
5.47	3.10	6.4	0.95
4.91	3.11	6.1	0.85
3.19	5.78	3.8	0.58
2.80	5.77	3.4	0.52
3.76	5.77	4.6	0.70
3.88	5.77	5.0	0.75
3.48	5.79	4.3	0.65
4.04	5.80	4.9	0.72
3.11	5.77	3.7	0.58
2.69	5.77	3.5	0.49
3.89	5.77	4.8	0.67

Table A.31: Movable Bed Wave Flume Data on Ripple Geometry under Regular Waves from Nielsen (1979); $d = 0.082$ mm and $s = 2.65$

A_b (cm)	ω (1/s)	λ (cm)	η (cm)
1.19	6.28	2.9	0.6
1.39	6.28	2.9	0.5
1.45	6.28	2.0	0.5
1.59	6.28	2.9	0.5
1.78	6.28	2.9	0.4
2.09	6.28	3.0	0.5
2.52	6.28	3.0	0.5
2.89	6.28	3.0	0.45
3.17	6.28	3.4	0.6
3.48	6.28	3.6	0.6
2.68	3.70	4.3	0.7
2.98	3.70	4.4	0.80
3.38	3.70	4.7	0.8
3.93	3.70	5.0	0.8
4.60	3.70	5.6	0.8
5.21	3.70	5.9	0.9
5.92	3.70	5.27	0.7
6.60	3.70	6.0	0.75
7.16	3.70	5.6	0.6
8.25	3.70	5.7	0.8
8.82	3.70	5.6	0.6
9.45	3.70	5.3	0.5
10.25	3.70	5.2	0.55
11.03	3.70	4.9	0.55

Table A.32: Movable Bed Wave Flume Data on Ripple Geometry under Regular Waves from Nielsen (1979); $d = 0.17$ mm and $s = 2.65$

A_b (cm)	ω (1/s)	λ (cm)	η (cm)
3.13	3.70	4.5	0.8
4.64	3.70	5.6	0.9
5.97	3.70	6.7	1.15
6.92	3.70	7.5	1.25
7.90	3.70	8.7	1.3
8.66	3.70	8.5	1.2
9.36	3.70	7.4	1.2
10.47	3.70	7.4	1.0
12.75	3.70	8.8	1.2
13.10	3.70	9.4	1.3

Table A.33: Movable Bed Wave Flume Data on Ripple Geometry under Regular Waves from Nielsen (1979); $d = 0.36$ mm and $s = 2.65$

A_b (cm)	ω (1/s)	λ (cm)	η (cm)
4.05	3.70	5.7	0.95
4.47	3.70	6.3	1.0
5.00	3.70	7.1	1.0
6.40	3.70	8.6	1.4
7.52	3.70	9.6	1.55
9.22	3.70	11.9	1.8
10.50	3.70	12.8	1.9
11.29	3.70	13.4	2.2
12.40	3.70	13.8	1.9
14.00	3.70	13.3	1.9

Table A.34: Movable Bed Wave Tunnel Data on Ripple Geometry under Regular Waves from Sato (1988); $d = 0.18$ mm and $s = 2.65$

A_b (cm)	ω (1/s)	λ (cm)	η (cm)
6.37	6.28	6.6	0.7
7.96	6.28	7.3	0.8
19.1	2.09	8.8	1.2
23.9	2.09	12.2	1.34
28.7	2.09	9.8	1.0
31.8	1.26	9.1	1.5
39.8	1.26	12.9	1.9
44.5	0.90	10.6	1.5
55.7	0.90	19.5	3.1
66.8	0.90	12.8	1.4

Table A.35: Movable Bed Wave Tunnel Data on Ripple Geometry under Regular Waves from Sato (1988); $d = 0.56$ mm and $s = 2.65$

A_b (cm)	ω (1/s)	λ (cm)	η (cm)
19.1	4.19	18.5	2.5
38.2	2.09	31.4	5.6
47.8	2.09	35.5	5.7
52.5	2.09	29.3	2.9
63.7	1.26	33.8	4.7
79.6	1.26	26.5	2.2
87.5	1.26	43.6	5.3

Appendix B

Spectral Pure Wave Experiments

Table B.1: Fixed Bed Attenuation Results for Spectral Pure Wave Experiments from Madsen and Mathisen (1996)

A_b **(cm)**	ω **(1/s)**	λ **(cm)**	η **(cm)**	f_e
3.81	2.89	10	1.5	0.42
4.52	2.88	10	1.5	0.287
6.09	2.84	10	1.5	0.215

Table B.2: Movable Bed Wave Tunnel Data on Ripple Geometry under Irregular Waves from Sato (1988); $d = 0.18$ mm and $s = 2.65$

A_b (cm)	ω (1/s)	λ (cm)	η (cm)
13.8	2.094	9.1	1.1
17.5	2.094	10.0	0.7
20.7	2.094	9.8	0.7
24.9	2.094	8.4	0.5
13.1	2.094	9.7	1.2
17.7	2.094	10.9	1.1
19.8	2.094	8.1	0.5
23.2	2.094	8.1	0.4
6.8	2.094	8.8	1.4
8.7	2.094	10.7	1.5
10.0	2.094	9.6	0.7
23.2	1.257	9.9	0.9
28.8	1.257	7.3	0.4
22.6	1.257	8.4	1.0
28.0	1.257	7.8	0.5
10.4	1.257	7.7	0.6
13.2	1.257	7.4	0.4

Table B.3: Movable Bed Wave Tunnel Data on Ripple Geometry under Irregular Waves from Sato (1988); $d = 0.56$ mm and $s = 2.65$

A_b (cm)	ω (1/s)	λ (cm)	η (cm)
14.7	4.189	16.8	1.6
18.4	4.189	16.1	1.1
7.2	4.189	17.5	1.8
9.0	4.189	18.6	2.2
28.2	2.094	27.5	3.3
35.1	2.094	35.0	2.7
14.7	2.094	32.6	4.9
17.6	2.094	31.4	3.1
18.5	2.094	26.4	2.5

Appendix C

Combined Wave-Current Flow Experiments

Table C.1: Fixed Bed Attenuation Results for Combined Wave-Current Flow Experiments from Madsen and Mathisen (1996)

A_b (cm)	ω (1/s)	u_{*w} (cm/s)	u_{*c} (cm/s)	λ (cm)	η (cm)	f_e
6.45	2.80	6.76	3.44	10	1.5	0.25
8.08	2.39	6.36	3.15	10	1.5	0.19
8.8	2.17	6.33	3.5	10	1.5	0.2
6.37	2.80	6.76	2.46	10	1.5	0.25
8	2.39	6.17	2.09	10	1.5	0.18
8.84	2.17	7.09	2.95	10	1.5	0.24
4.31	2.80	5.27	2.46	10	1.5	0.33
5.61	2.39	5.12	2.08	10	1.5	0.26
6.12	2.17	5.46	2.95	10	1.5	0.29
6.61	2.80	5.5	3.2	20	1.5	0.17
8.22	2.39	5.36	2.8	20	1.5	0.14
9.11	2.17	5.58	3.2	20	1.5	0.15
6.55	2.80	5.36	2.6	20	1.5	0.15
8.2	2.39	5.88	2.15	20	1.5	0.15
9.18	2.17	6.44	2.6	20	1.5	0.18

Appendix D

Spectral Wave-Current Flow Experiments

Table D.1: Fixed Bed Attenuation Results for Spectral Wave-Current Flow Experiments from Madsen and Mathisen (1996)

A_b (cm)	ω (1/s)	u_{*w} (cm/s)	u_{*c} (cm/s)	λ (cm)	η (cm)	f_e
3.59	2.92	5.02	2.71	10	1.5	0.37
4.48	2.89	5.74	2.35	10	1.5	0.317

Appendix E

Wave-Current Field Data

Table E.1: Wave-Current Field Data used by Styles and Glenn (2002)

A_b (cm)	ω (1/s)	ϕ_{wc} (deg)	u_{*c} (cm/s)	z_{0a} (cm)	λ (cm)	η (cm)
20.77	0.67	4.78	1.02	5.21	19.84	7.70
22.87	0.65	21.54	0.84	5.55	19.72	7.76
21.67	0.72	74.80	0.67	1.03	26.26	8.18
28.39	0.84	54.64	0.96	3.53	36.61	8.36
27.78	0.86	83.41	0.99	3.08	43.65	8.54
32.09	0.84	45.50	1.34	5.80	42.15	8.66
30.41	0.88	69.18	1.39	3.71	43.99	8.72
31.36	0.82	68.53	1.72	5.47	46.85	8.78
29.30	0.87	62.50	1.66	3.05	47.08	8.84
31.49	0.88	87.07	1.53	2.70	47.62	8.90
31.64	0.80	63.54	1.67	12.75	53.09	9.38
30.95	0.82	71.89	1.44	15.60	53.80	9.43
33.15	0.79	78.00	1.26	11.06	53.53	9.47
32.48	0.59	75.15	1.39	15.43	65.30	9.54
28.13	0.61	65.59	1.20	1.51	64.34	9.53
29.96	0.69	65.62	2.04	2.85	60.30	9.52
29.75	0.77	53.89	2.19	2.40	58.29	9.52
30.12	0.77	38.80	1.79	1.88	57.30	9.52
28.64	0.79	33.39	2.28	1.92	56.54	9.52
29.19	0.74	39.39	2.22	3.19	52.21	9.52
27.97	0.76	40.37	1.86	6.26	46.64	9.52
31.01	0.74	47.74	2.26	3.86	42.93	9.53
28.31	0.75	59.22	1.79	5.14	42.94	9.54

Table E.2: Wave-Current Field Data used by Styles and Glenn (2002); continued

A_b (cm)	ω (1/s)	ϕ_{wc} (deg)	u_{*c} (cm/s)	z_{0a} (cm)	λ (cm)	η (cm)
25.91	0.77	61.38	1.33	4.64	44.26	9.54
21.84	0.74	16.27	1.34	14.06	56.80	9.61
33.26	0.62	73.99	1.48	4.14	55.76	10.31
30.59	0.63	79.26	1.50	5.36	61.45	10.40
34.58	0.59	70.46	1.71	4.14	61.16	10.43
33.01	0.59	68.66	1.76	3.44	61.22	10.45
32.46	0.62	66.65	1.99	3.29	63.19	10.48
30.92	0.61	65.56	1.55	4.24	63.74	10.51
40.68	0.60	72.85	1.51	9.08	63.81	10.53
31.01	0.60	80.89	1.39	12.77	62.86	10.56
37.77	0.63	82.99	0.93	9.76	67.56	10.81
38.02	0.63	89.13	1.08	12.25	67.12	10.81
28.82	0.64	76.93	1.26	11.23	71.87	10.72
32.64	0.64	83.21	1.51	12.85	71.15	10.71
30.81	0.63	78.97	1.93	7.43	71.50	10.70
37.15	0.56	87.55	1.65	21.91	73.35	10.55
35.74	0.57	87.03	1.76	5.93	66.66	10.52
34.88	0.55	88.90	1.97	6.06	65.55	10.52
38.86	0.54	81.92	1.83	3.29	65.58	10.53
34.34	0.56	83.44	1.43	4.14	67.71	10.53
33.60	0.53	77.12	1.32	9.53	67.82	10.54
38.05	0.54	48.51	1.42	13.79	73.85	10.60
45.49	0.53	42.23	1.42	12.62	77.64	12.27
35.05	0.62	20.81	0.82	4.17	96.42	13.77

Table E.3: Field Data on Wave-Formed Ripple Geometry from Dingler (1974)

A_b (cm)	ω (1/s)	λ (cm)	η (cm)	d (cm)
56.5	0.722	8	0.29	0.0172
82.5	0.452	65.0	9.20	0.0555
50.5	0.628	8.8	0.36	0.0177
38.5	0.911	8.4	0.38	0.0158
59.5	0.576	7.9	0.47	0.0176
54.0	0.748	8.0	0.44	0.0151
39.0	0.766	7.7	0.49	0.0132
62.5	0.576	7.9	0.46	0.0128
52.5	0.524	7.2	0.52	0.0131
67.5	0.576	8.2	0.50	0.0131
64.5	0.571	7.9	0.48	0.0170
50.5	0.571	8.0	0.63	0.0170
45.0	0.546	7.5	0.57	0.0170
66.0	0.507	7.5	0.48	0.0155
57.0	0.519	7.4	0.46	0.0155
35.0	0.648	7.6	0.62	0.0176
50.5	0.648	8.5	0.60	0.0206
26.0	0.551	20.6	3.40	0.0179
73.0	0.483	8.1	0.48	0.0159
98.5	0.495	8.3	0.25	0.0159
62.5	0.576	64.0	10.70	0.0582
59.0	0.587	79.0	13.50	0.0616
94.0	0.871	13.7	0.56	0.0412
98.0	0.546	14.0	0.49	0.0409

Table E.4: Field Data on Waved-Formed Ripple Geometry from Inman (1957)

A_b (cm)	ω (1/s)	λ (cm)	η (cm)	d (cm)
55.0	0.628	5.8	0.46	0.0118
29.1	0.898	7.3	1.0	0.0153
20.5	0.785	8.8	1.2	0.0145
43.1	0.849	7.0	0.6	0.0150
22.6	0.628	7.9	1.2	0.0152
39.9	0.542	7.9	0.6	0.0151
59.3	0.628	6.4	0.6	0.0147
61.4	0.571	7.9	0.6	0.0157
44.1	0.628	7.6	0.6	0.0137
33.4	0.683	7.3	0.9	0.0124
20.5	0.785	8.5	1.2	0.0117
20.5	1.047	9.1	1.5	0.0120
11.9	1.013	11.9	1.8	0.0117
44.2	0.731	6.7	0.6	0.0118
23.7	0.648	9.1	0.9	0.0124

Table E.5: Field Data on Waved-Formed Ripple Geometry from Inman (1957); continued

A_b (cm)	ω (1/s)	λ (cm)	η (cm)	d (cm)
21.6	0.628	8.8	1.4	0.0129
31.3	0.622	7.6	0.8	0.0126
26.9	0.661	7.0	0.6	0.0118
55.0	0.571	7.6	0.6	0.0114
63.6	0.483	7.0	0.6	0.0117
10.8	0.785	18.6	2.3	0.0135
6.6	1.257	9.4	1.2	0.0127
10.8	0.785	18.9	2.4	0.0115
7.5	0.966	11.9	1.5	0.0106
4.3	1.047	10.0	1.8	0.0107
35.6	0.604	7.6	0.5	0.0102
25.9	0.739	7.9	0.7	0.0102
41.0	0.483	7.9	0.9	0.0102
14.0	0.661	16.1	1.5	0.0106
4.3	1.257	11.3	1.8	0.0103
10.8	0.483	11.9	1.8	0.0109
32.3	0.483	7.9	1.4	0.0106

Table E.6: Field Data on Waved-Formed Ripple Geometry from Inman (1957); continued

A_b (cm)	ω (1/s)	λ (cm)	η (cm)	d (cm)
24.8	0.628	14.9	1.5	0.0106
16.2	0.524	12.5	1.8	0.0109
22.6	0.524	11.6	1.5	0.0113
5.4	0.698	10.0	1.7	0.0081
44.2	0.698	57.3	9.1	0.0555
26.9	0.698	53.9	9.1	0.0483
97.0	0.419	85.3	15.2	0.0635
44.2	0.648	36.6	4.6	0.0266
25.9	0.610	45.3	6.7	0.0302
30.2	0.628	71.0	11.2	0.0418
31.3	0.483	70.7	10.7	0.0408
37.7	0.524	81.4	12.5	0.0412
32.3	0.571	77.7	13.4	0.0406
32.3	0.571	80.5	12.8	0.0406
28.0	0.524	80.8	13.7	0.0466
33.4	0.571	79.2	12.2	0.0345
31.3	0.648	91.4	14.6	0.0448
23.7	0.610	91.4	14.6	0.0462
24.8	0.571	77.1	11.9	0.0423
34.5	0.524	82.9	13.4	0.0430
23.7	0.628	53.3	7.6	0.0457

Table E.7: Field Data on Waved-Formed Ripple Geometry from Nielsen (1984)

A_b (cm)	ω (1/s)	λ (cm)	η (cm)	d (cm)
50.7	0.748	50.0	5	0.049
47.0	0.885	50.0	15.0	0.050
50.4	0.838	50.0	15.0	0.050
50.3	0.827	50.0	15.0	0.050
39.8	0.885	5.0	0.5	0.011
58.6	0.806	70.0	7.5	0.033
59.9	0.706	70.0	7.5	0.033
47.7	0.766	65.0	7.5	0.030
64.1	0.698	65.0	7.5	0.030
58.6	0.766	80.0	10.0	0.040
70.9	0.748	60.0	8.0	0.040
60.8	0.806	60.0	8.0	0.040
58.1	0.628	55.0	5.7	0.044
137.5	0.524	55.0	5.7	0.062
94.6	0.598	48.0	4.3	0.051

Table E.8: Field Data on Waved-Formed Ripple Geometry from Nielsen (1984); continued

A_b (cm)	ω (1/s)	λ (cm)	η (cm)	d (cm)
63.9	0.668	48.0	4.3	0.045
116.1	0.487	50.0	8.0	0.038
101.4	0.499	50.0	9.0	0.038
88.8	0.561	35.0	7.0	0.045
61.5	1.102	50.0	8.0	0.044
69.2	0.885	60.0	8.0	0.048
70.7	0.816	60.0	8.0	0.049
93.3	0.655	60.0	8.0	0.047
113.6	0.616	60.0	8.0	0.047
70.9	0.683	50.0	7.5	0.047
49.9	0.873	50.0	7.5	0.047
43.6	1.103	55.0	10.0	0.045
45.2	1.030	55.0	10.0	0.045

Bibliography

[1] Abramowitz, M. and Stegun I.A. (1972). *Handbook of Mathematical Functions*, Volume 55 of *National Bureau of Applied Mathematics Series*, Dover Publications Inc., Mineola, NY.

[2] Bagnold, R.A. (1946). Motion of Waves in Shallow Water, Interaction Between Waves and Sand Bottoms, *Proceedings of the Royal Society*, Ser. A, Vol. 187: 1-18.

[3] Barreto-Acobe, C.D. (2001). *Turbulent Wave-Current Boundary Layers Revisited*, S.M. Thesis, Massachusetts Institute of Technology, Cambridge, MA.

[4] Boyd, R., Forbes, D.L., and Heffler, D.E. (1988). Time-sequence Observations of Wave-formed Sand Ripples on an Ocean Shore Face. *Sedimentology*, Vol. 35:449-464.

[5] Carstens, M.R., Neilson, R.M., and Altinbilek, H.D. (1969). Bedforms Generated in the Laboratory under an Oscillatory Flow: Analytical and Experimental Study *Technical Report TM-28*, U.S. Army Corps of Engineers, Coastal Engineering Research Center.

[6] Daily, J.W. and Harleman, D.R.F. (1966). *Fluid Dynamics*, Addison-Wesley Publishing Co., Reading, MA.

[7] Davies, A.G., Soulsby, R.L. and King, H.L. (1988). A numerical model of the combined wave and current bottom boundary layer, *Journal of Geophysical Research*, 93(C1): 491-508.

[8] Dingler, J.R. (1975). *Wave Formed Ripples in Nearshore Sands*, Ph.D. Thesis, University of California, San Diego.

[9] Dingler, J.R. and Inman, D.L. (1976). Wave Formed Ripples in Nearshore Sands, *Proceedings of the 15th International Conference on Coastal Engineering*, ASCE, 2109-2126.

[10] Grant, W.D. (1977). *Bottom Friction Under Waves in the Presence of a Weak Current: Its Relationship to Coastal Sediment Transport*, Sc.D. Thesis, Massachusetts Institute of Technology, Cambridge, MA.

[11] Grant, W.D. and Madsen, O.S. (1979). Combined Wave and Current Interaction with a Rough Bottom, *Journal of Geophysical Research*, 84(C4): 1797-1808.

[12] Grant, W.D. and Madsen, O.S. (1982). Movable Bed Roughness in Oscillatory Flow, *Journal of Geophysical Research*, 87(C1): 469-481.

[13] Grant, W.D. and Madsen, O.S. (1986). The Continental Shelf Bottom Boundary Layer, *Annual Review of Fluid Mechanics*, 18: 265-305.

[14] Hildebrand, F.B. (1976). *Advanced Calculus for Applications*, 2nd Ed., Prentice-Hall, Englewood Cliffs, NJ.

[15] Inman, D.L. (1957). Wave Generated Ripples in Nearshore Sands, *Report TM-100*, U.S. Army Corps of Engineers, Beach Erosion Board.

[16] Inman, D.L. and Bowen, A.J. (1963). Flume Experiments on Sand Transport by Waves and Currents, *Proceedings of the 8th International Conference on Coastal Engineering*, ASCE, 137-150.

[17] Jonsson, I.G. (1966). Wave Boundary Layer and Friction Factors, *Proceedings of the 10th International Conference on Coastal Engineering*, ASCE, Toyko, Japan, 127-148.

[18] Kennedy, J.F. and Falcon, M. (1965). Wave Generated Sediment Ripples, *Technical Report No. 86*, Hydrodynamics Laboratory, Department of Civil Engineering, Massachusetts Institute of Technology.

[19] Lambie, J.M. (1984). *An Experimental Study of the Stability of Oscillatory Flow Bed Configurations*, M.S. Thesis, Massachusetts Institute of Technology, Cambridge, MA.

[20] Lofquist, K.E.B. (1978). Sand Ripple Growth in an Oscillatory Flow Water Tunnel, *Technical Report TP-78-5*, U.S. Army Corp of Engineers, Coastal Engineering Research Center.

[21] Lofquist, K.E.B. (1986). Drag on Naturally Rippled Beds under Oscillatory Flows. *Technical Report MP-86-13*, U.S. Army Corp of Engineers, Coastal Engineering Research Center.

[22] Madsen, O.S. (1994). Spectral Wave-current Bottom Boundary Layer Flows, *Proceedings of the 24th International Conference on Coastal Engineering*, ASCE, Kobe, Japan, 384-398.

[23] Madsen, O.S. and Salles, P. (1998). Eddy Viscosity Models for Wave Boundary Layers, *Proceedings of the 26th International Conference on Coastal Engineering*, ASCE, Copenhagen, Denmark, 2615-2627.

[24] Madsen, O.S. and Wikramanayake, P.N. (1991). Simple Models for Turbulent Wave-current Bottom Boundary Flow, *Contract Report DRP-91-1*, U.S. Army Corps of Engineers, Waterways Experiment Station, Vicksburg, MS.

[25] Mathisen, P.P. (1989). *Experimental Study on the Response of Fine Sediments to Wave Agitation and Associated Wave Attenuation.* S.M. Thesis, Massachusetts Institute of Technology, Cambridge, MA.

[26] Mathisen, P.P. (1993). *Bottom Roughness for Wave and Current Boundary Layer Flows over a Rippled Bed.* Ph.D. Thesis, Massachusetts Institute of Technology, Cambridge, MA.

[27] Mathisen, P.P. and Madsen, O.S. (1996). Waves and Currents over a Fixed Rippled Bed, 1. Bottom Roughness Experienced by Waves in the Presence and Absence of Currents, *Journal of Geophysical Research*, 101(C7): 16,533-16,542.

[28] Mathisen, P.P. and Madsen, O.S. (1996). Waves and Currents over a Fixed Rippled Bed, 2. Bottom and Apparent Roughness Experienced by Currents in the Presence of Waves, *Journal of Geophysical Research*, 101(C7): 16,543-16,550.

[29] Mathisen, P.P. and Madsen, O.S. (1999). Waves and Currents over a Fixed Rippled Bed, 3. Bottom and Apparent Roughness for Spectral Waves and Currents, *Journal of Geophysical Research*, 104(C8): 18,447-18,461.

[30] Miller, M.C. and Komar, P.D. (1980). Oscillation Sand Ripples Generated by Laboratory Apparatus, *Journal of Sedimentary Petrology*, Vol. 50, No. 1:173-182.

[31] Miller, M.C. and Komar, P.D. (1980). A Field Investigation of the Relationship between Oscillation Ripple Spacing and the Near-bottom Water Orbital Motion, *Journal of Sedimentary Petrology*, Vol. 50, No. 1:183-191.

[32] Mogridge, G.R. and Kamphuis, J.W. (1972). Experiments on Bed Form Generation by Wave Action, *Proceedings of the 13th International Conference on Coastal Engineering*, ASCE, 1123-1134.

[33] Nielsen, P. (1979). Some Basic Concepts of Wave Sediment Transport, *Series Paper No. 20*, Institute of Hydrodynamics and Hydraulic Engineering, Technical University of Denmark.

[34] Nielsen, P. (1984). Field Measurements of the Time-Averaged Suspended Sediment Concentration under Waves, *Coastal Engineering*, Vol. 8:51-72.

[35] Rosengaus, M. (1987). *Experimental Study in Wave Generated Bedforms and Resulting Wave Attenuation*, Sc.D. Thesis, Massachusetts Institute of Technology, Cambridge, MA.

[36] Salles, P. (1997). *Eddy Viscosity Models for Pure Waves Over Large Roughness Elements*, M.S. Thesis, Massachusetts Institute of Technology, Cambridge, MA.

[37] Sato, S., Mitani, K., and Watanabe, A. (1987). Geomtry of Sand Ripples and Net Sand Transport Due to Regular and Irregular Oscillatory Flows, *Coastal Engineering in Japan*, Vol. 30, No. 2:89-98.

[38] Sato, S. and Horikawa, K. (1988). Sand Ripple Geometry and Sand Transport Mechanism Due to Irregular Oscillatory Flows, *Proceedings of the 21st International Conference on Coastal Engineering*, ASCE, 1748-1762.

[39] Sleath, J.F.A. (1985). Energy Dissipation in Oscillatory Flow Over Rippled Beds. *Coastal Engineering*, 9:159-170.

[40] Styles, R. and Glenn, S.M. (2000). Modeling Stratified Wave and Current Bottom Boundary Layers on the Continental Shelf, *Journal of Geophysical Research*, 24119-24139.

[41] Styles, R. and Glenn, S.M. (2002). Modeling Bottom Roughness in the Presence of Wave-generated Ripples, *Journal of Geophysical Research*, 107(C8): 24/1-24/15.

[42] Wikramanayake, P.N. and Madsen, O.S. (1990). Calculation of Movable Bed Friction Factors, *Technical Progress Report No. 2*, Prepared for the U.S. Army Corps of Engineers, Waterways Experiment Station, Vicksburg, MS.

[43] Wikramanayake, P.N. and Madsen, O.S. (1991). Calculation of Movable Bed Friction Factors, *Technical Progress Report*, Prepared for the U.S. Army Corps of Engineers, Waterways Experiment Station, Vicksburg, MS.